

IMAGING BEYOND STRUCTURE
- novel noninvasive tools for neuroimaging of
stem cell function and differentiation -

Dissertation

zur Erlangung des akademischen Grades

**doctor rerum naturalium
(Dr. rer. nat.)**

genehmigt durch die Fakultät für Naturwissenschaften
der Otto-von-Guericke-Universität Magdeburg

von
Dipl. Neurowissenschaftler

Markus Aswendt

geb. am 20.05.1984 in Karl-Marx-Stadt

Gutachter:
Prof. Dr. Klaus Reymann
Prof. Dr. Annemie Van der Linden

eingereicht am: 26.11.2012

verteidigt am: 18.03.2013

Für meine Eltern

Table of contents

ABSTRACT	6
1. BACKGROUND	7
1.1 Noninvasive imaging for stem cell therapy	7
1.1.1 <i>Embryonic and neural stem cells</i>	7
1.1.2 <i>Stem cell therapy</i>	8
1.1.3 <i>Stem cell transplantation – a novel therapy in stroke</i>	8
1.1.4 <i>Noninvasive imaging</i>	9
1.1.5 <i>The imaging reporter concept</i>	10
1.2 MRI basics	11
1.2.1 <i>Principles of magnetic resonance</i>	11
1.2.2 <i>Basic MRI sequences</i>	13
1.2.3 <i>Superparamagnetic contrast agents</i>	14
1.2.4 <i>Paramagnetic contrast agents</i>	14
1.2.5 <i>Responsive contrast agents</i>	15
1.2.6 <i>MRI-based cell tracking</i>	15
1.3 Optical imaging basics	16
1.3.1 <i>Fluorescence imaging</i>	17
1.3.2 <i>Bioluminescence imaging</i>	18
1.3.3 <i>Optical imaging-based cell tracking</i>	19
2. MATERIAL & METHODS	20
2.1 Devices	20
2.2 Consumables	21
2.3 Molecular Biology	23
2.3.1 <i>Cloning of imaging reporter plasmids</i>	23
2.3.2 <i>Qualitative identification of gene expression with PCR</i>	25
2.3.3 <i>Quantification of gene expression with qPCR</i>	27
2.3.4 <i>Protein Biochemistry</i>	28
2.4 Cell culture	29
2.4.1 <i>Cell lines</i>	29
2.4.2 <i>Cell culture media, supplements and coatings</i>	31
2.4.3 <i>Cell culture protocols</i>	32
2.4.4 <i>Transfection protocols</i>	33
2.4.5 <i>Transduction protocols</i>	33

2.4.6	<i>Cell labeling with contrast agents</i>	34
2.4.7	<i>Phantom preparation for MRI</i>	35
2.4.8	<i>Characterization of labeled cells and transduced cells</i>	36
2.5	Histology	37
2.6	Animal experimental protocol	38
2.6.1	<i>Animal handling and anesthesia</i>	38
2.6.2	<i>Intracerebral transplantation</i>	39
2.7	Experimental imaging setup	40
2.7.1	<i>Evaluation of MRI sequences for determining T_1 relaxation</i>	40
2.7.3	<i>In vitro and in vivo MRI protocols</i>	42
2.7.4	<i>MRI postprocessing</i>	43
2.7.6	<i>Optical imaging</i>	44
2.7.7	<i>Microscopy</i>	46
2.8	Statistics	46
3.	IMAGING GABAERGIC NEURONS BY MRI	47
3.1	Project aim and experimental setup	47
3.2	Results	48
3.2.1	<i>MRI sequence validation</i>	48
3.2.2	<i>Novel responsive contrast agent for detection of GAD activity</i>	50
3.2.3	<i>Characterization of GAD-dependent contrast agent activation in tissue lysates</i>	50
3.2.4	<i>Differentiation protocol for GABAergic neurons from embryonic stem cells</i>	51
3.2.5	<i>Evaluation of the optimal Gd-chelate labeling procedure</i>	53
3.2.6	<i>GABAergic neuron-specific contrast in vitro</i>	54
3.2.7	<i>In vivo cell imaging at high field strength</i>	54
3.3	Discussion	56
3.3.1	<i>Validation of RAREVTR sequences for stable and reliable T_1 determination</i>	56
3.3.2	<i>Contrast agent mechanism</i>	56
3.3.3	<i>GABAergic differentiation protocol</i>	57
3.3.4	<i>Labeling of stem cells and derivatives with paramagnetic agents</i>	57
3.3.5	<i>T_1 relaxation dependent discrimination of GABAergic neurons</i>	58
3.4	Conclusion and Outlook	58
4.	BOOSTING BIOLUMINESCENCE FOR SENSITIVE NEUROIMAGING	59
4.1	Project aim and experimental setup	59
4.2	Results	60

4.2.1	<i>D3WT_N2Euro – a radial glia-like neural stem cell line</i>	60
4.2.2	<i>In vitro bioluminescence comparison in D3WT_N2Euro and HEK-293</i>	63
4.2.3	<i>Bioluminescence imaging of cells grafted into the mouse brain</i>	64
4.2.4	<i>Spectral luciferase analysis in vivo</i>	65
4.2.5	<i>BLI protocol optimization</i>	65
4.2.6	<i>Generation of advanced Luc2+ NSCs</i>	68
4.2.7	<i>Detection of small number of grafted NSCs with the advanced protocol</i>	71
4.3	Discussion	72
4.3.1	<i>Mouse neural stem cell line derived from embryonic stem cells</i>	72
4.3.2	<i>Imaging reporter expression</i>	73
4.3.3	<i>Quantitative in vitro and in vivo luciferase comparison</i>	74
4.3.4	<i>Revision of the standard protocol for bioluminescence neuroimaging</i>	76
4.4	Conclusion and Outlook	80
5.	NONINVASIVE IMAGING OF NEURAL STEM CELL DIFFERENTIATION	81
5.1	Project aim and experimental setup	81
5.2	Results	82
5.2.1	<i>Validation of the GFAP promoter driven reporter gene expression</i>	82
5.2.2	<i>Dual reporter neural stem cells</i>	83
5.2.3	<i>Dual reporter monitoring of glial differentiation</i>	84
5.4	Discussion	86
5.4.1	<i>Validation of the GFAP promoter driven reporter gene expression</i>	86
5.4.2	<i>Dual reporter neural stem cells provide monitoring of glial differentiation</i>	87
5.5	Conclusion and Outlook	87
6.	SYNOPSIS	89
7.	LIST OF ABBREVIATIONS	90
8.	REFERENCES	93
9.	PUBLICATIONS	104

ABSTRACT

Stroke is one of the leading causes of death and permanent disability worldwide. However, the clinically approved therapies are strictly limited. One promising novel approach is the transplantation of stem cells to enhance recovery. Prior to a successful clinical translation, experimental models are necessary to reveal the underlying biological mechanisms. Noninvasive imaging, particularly magnetic resonance imaging, evolved as a novel tool to study stem cell location and migration in the living animal over time. Contrast agents are used to label cells prior to transplantation and allow the discrimination from the host tissue. One remaining drawback is the limitation on structural information. The question remains, how to elucidate additional cell properties - like viability and fate.

This dissertation includes novel neuroimaging techniques: contrast agents responsive to a specific cellular function and optical reporters of cell viability and cell differentiation. The first project includes the development of a molecular probe, bioengineered to detect selectively the expression of glutamic acid decarboxylase. This enzyme is unambiguously expressed in the brain by GABAergic neurons. The novel contrast agent serves as a substrate for the enzyme and permits the discrimination of GABAergic neurons from immature cells based on the decreased T_1 relaxation rate.

Optical cell tracking with bioluminescence has been investigated in the second project. Luciferases, e.g. isolated from the firefly *Photinus Pyralis*, can be expressed in mammalian cells and permit a cell viability-dependent readout. A transgenic mouse model of luciferase expression restricted to double-cortin-positive neurons served as a reference for optical neuroimaging and allowed bioluminescence protocol optimization under stable conditions. Luciferase substrate concentrations, injection routes and anesthesia effects were investigated. As a major result, an optimized protocol with 2-fold higher sensitivity was established. A mouse neural stem cell line was generated and transduced with 4 different luciferases for a quantitative comparison after transplantation into the mouse brain. Firefly luciferase Luc2 was selected because of its superior bioluminescence in the brain. Cell grafts were imaged with surpassing sensitivity by applying the empirically optimized protocol.

Based on this evaluation, neural stem cells were genetically modified to express a set of distinct optical reporters under control of either a constitutive promoter or cell-specific promoter. Glial differentiation has been monitored by the induced expression of firefly luciferase and the fluorescent protein mCherry controlled by the GFAP promoter.

The results presented in this dissertation show the potential of noninvasive approaches for elucidating key cell features, like viability and differentiation. These methods can be applied for in vivo studies and provide significantly more details of graft behavior. They enable stem cell induced recovery assessment in neurodegenerative disease like stroke without the need of invasive intervention.

1. BACKGROUND

1.1 Noninvasive imaging for stem cell therapy

1.1.1 Embryonic and neural stem cells

Stem cells serve as the fundament of body homeostasis, wound healing and immunity. The embryoblast, composed of the blastocyst's inner cell mass, contains the stem cell origin, which will give rise to fetal, neonatal and adult stem cells during development. These embryonic stem (ES) cells are capable of reconstituting every cell type independent of the germ layer background, which makes them *pluripotent*. The ES cell isolation and adaption on cell culture conditions in the early 1980s by Evans, Kaufman and Martin^{1,2} marks the breakthrough of experimental stem cell research. Maintenance of pluripotency in vitro is mainly achieved by the cell culture supplement LIF (leukemia-inhibitory factor), which triggers activation of the transcription factor STAT3 - one of the essential key factors of self-renewal. In general, stem cell state in vitro is defined by the potential to divide and differentiate into various cell types and the reconstitution of the stem cell pool (self-renewal). In contrast to ES cells, the potential of adult stem cells is limited by self-renewal and differentiation into the cell types of their host tissue (*multipotency*). Adult stem cells exist exclusively in tissue specific niches for example in the bone marrow, skin and fat³⁻⁵. Whereas persistent dividing cells with stem cell characteristics in the mammalian brain have been discussed controversially⁶ until the early 1990s. The experiments of Eriksson and colleagues⁷, finally proved early reports on neural stem cells (NSCs) in a human study using the cell division marker BrdU (5-bromo-2'-deoxyuridine). The in vitro characterization of mammalian NSCs was made possible by the neurosphere assay invented by Reynolds and Weiss⁸. Cells from the adult brain tissue are isolated and cultured in the presence of growth factors to form neurospheres, which consist of cells with NSC properties. The maintenance of multipotency and self-renewal is achieved by the supplementation with the growth factors EGF and b-FGF, which specifically stimulate NSC proliferation and enable the continuous passaging, as it was shown for human NSCs up to 2 years of sustained culture⁹. In addition, stable NSC lines have been generated by immortalization using retroviral oncogene transfer, as described by Ryder *et al.*¹⁰ for mouse NSCs and recently adapted for human NSCs¹¹. The adult mammalian brain constitutes two major neurogenic regions, the subependymal (SE) zone ensheating the lateral ventricles^{12,13} and the subgranular zone (SGZ) of the dentate gyrus of the hippocampus¹⁴. GFAP-positive cells persist in these regions, which retain the potential to proliferate and generate differentiated daughter cells. The cellular composition was described by Doetsch and colleagues and proposed to consist of a GFAP positive astrocyte within the SE and SGZ. These cells divide into putative precursor cells, that in turn give rise to migrating neuroblasts (SE) or new granule neurons (SGZ)¹⁵. However, the in vivo identity of NSCs

remains still controversial¹⁶ because of the lack of definitive markers – e.g. GFAP is insufficient because it is expressed by non-neural cells (astrocytes) and non-stem cells¹⁷.

1.1.2 Stem cell therapy

Regeneration of damaged neural tissue and reconstitution of lost neural circuits is hampered by the irreversibility and progression of these processes in many human neurological diseases (e.g. Huntington, Parkinson and Stroke). Although endogenous repair mechanisms include the generation of novel neurons from endogenous NSCs, they are not effective enough to restore lost brain tissue completely. This is meant to be enhanced and supported by the application of exogenous (neural) stem cells. Cell replacement therapy initially aimed to replace damaged tissue by spontaneous differentiation into the appropriate cell type. However, this attempt is impeded by the differentiation efficiency, low neural circuit integration and the graft survival in vivo. Nevertheless, transplantation of stem cells from various tissue sources was highly investigated during the last decade and could prove enhanced functional recovery and/or tissue reorganization in animal models of neurological disorders^{18,19}. More recently, the observed beneficial effects are explained by a combination of immunosuppressive²⁰, neuroprotective²¹ and neurotrophic effects²². The understanding of mechanisms underlying stem cell induced regeneration is at the beginning and strictly dependent on the development of noninvasive imaging techniques with the aim of elucidating these processes under in vivo conditions.

1.1.3 Stem cell transplantation – a novel therapy in stroke

Stroke is the second leading cause of death²³ and the leading cause of long-term disability²⁴. It is characterized by an embolic/thrombotic vessel blockage or a hemorrhagic bleeding. The clinical therapy is strictly limited to a small subset of patients, administered with recombinant tissue plasminogen activator (rtPA) for recanalization of the vessels within a strict time limit of 4.5 h after stroke onset²⁵.

Human stroke is experimentally mimicked in rats and mice e.g. by blocking the middle cerebral artery (MCAo)²⁶. This results in a substantially reduced blood supply to the cortex and parts of the subcortical regions, leading to a progressive loss of neurons in cortical and subcortical regions. The aim of stem cell therapy in stroke is in the first place to boost the functional recovery (see 1.1.2). Various experimental studies supplied evidence for the successful improvement of behavior and motor functions after stem cell therapy^{27,28}. Furthermore, clinical trials are already in progress (e.g. a phase I study in Guildford, UK, Id-nr. NCT01151124). Beside the route, timing and side of delivery, various types of stem cells are under investigation: ES cells, NSCs and stem cells isolated from bone marrow, umbilical cord blood and adipose tissue. Recently human induced pluripotent stem cells were invented, which serve as an patient-specific source for autologous transplantations²⁹.

The conventional experimental approach includes subgroups of animals to reveal the endogenous recovery mechanisms from the transplant induced and the influence of the surgery itself for each individual time point. The result is a high number of laboratory animals used for one single experiment. Therefore, monitoring of the cell transplant, the stroke tissue evolution and the animal physiology are the main challenges for *noninvasive* approaches and essential for a successful therapy monitoring²⁸.

1.1.4 Noninvasive imaging

Noninvasive imaging offers the exclusive advantage over established invasive methods to observe biological processes in the living organism with only mild effects on the physiological homeostasis (Table 1). Conventional histological or electrophysiological approaches require the sacrificing of the animal at a distinct time point of the experiment. Therefore, to avoid the loss of the animal specific physiological state organotypical slice cultures can be used for a limited time – up to 6 days³⁰. Noninvasive imaging was invented to overcome the limitation of describing only the pathological state by enabling the detection of single molecular events (e.g. gene expression) responsible for a certain disease³¹ under in vivo conditions. Various techniques exist for small animal imaging based on radio-nuclides (e.g. Positron Emission Tomography, PET), based on optical probes (e.g. bioluminescence imaging, BLI), and based on magnetic probes (e.g. magnetic resonance imaging, MRI). These methods differ in spectral and temporal resolution, sensitivity, signal specificity, and tissue penetration (Figure 1). Optical methods are limited by the poor spatial resolution, but offer high sensitivity. Radiotracer methods are also highly sensitive but offer only slightly higher spatial resolution. Finally, MRI is superior for spatial resolution near the range of computer tomography (CT), but is limited in sensitivity.

Table 1: Characteristic properties of invasive and noninvasive methods

	Invasive	Noninvasive
Complexity	- Methods established and cost effective	- Methods still under development, expensive equipment
Methods	- Have to be performed in separate sessions and multimodality strictly limited	- Allow multimodal detection the same day
Resolution	- Subcellular (microscopic)	- Multicellular (macroscopic)
Animals	- High group size, Observations limited to one point of time	- Repetitive measurements on the same animal, each serves as its control

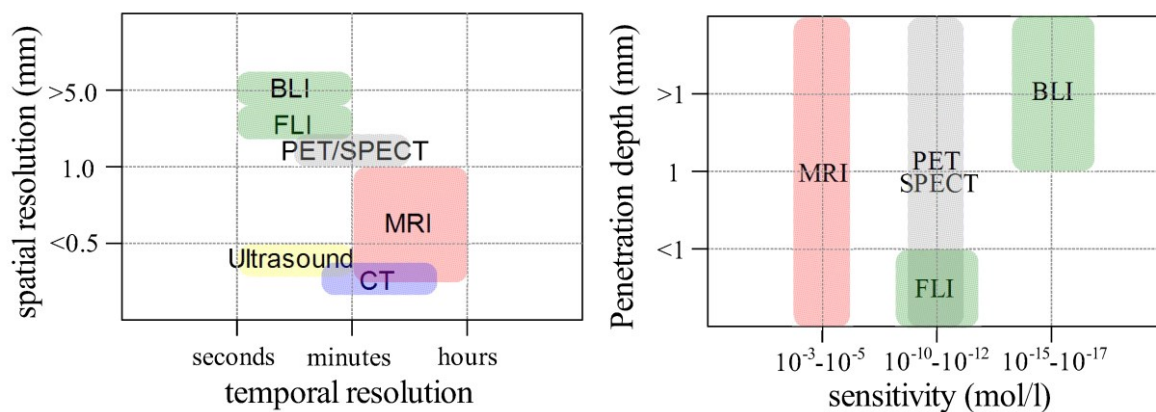


Figure 1: Schematic overview of selected noninvasive imaging modalities illustrating the differences in spatial/temporal resolution, penetration depth and sensitivity³¹.

1.1.5 The imaging reporter concept

The fast development of noninvasive imaging techniques in the last decade was a prerequisite for a novel combination of molecular biology and medical imaging, called *Molecular Imaging*. Molecular Imaging includes the visualization, characterization and quantification of biological processes at the cellular and subcellular level within living subjects³¹. As a basic principle, the gene of interest is monitored by a genetically linked reporter gene or serves itself as an imaging reporter. As a result, proteins/enzymes are expressed and detected with noninvasive imaging techniques. This approach is going to revolutionize the search of disease-related biomarkers because novel therapies can be monitored for specific target genes in the living organism in real time. Several prerequisites for an imaging reporter have to be considered: 1) stable, non-toxic, non-immunogenic, 2) high specificity and 3) biologically relevant half-life. Furthermore, imaging reporter substrates (e.g. for bioluminescence) should have the ability to cross biological barriers and enter the target cells. This dissertation involves examples from MRI and OI-based imaging reporter¹.

¹ For a comprehensive review of other modalities including radionuclide based approaches, see²²².

1.2 MRI basics

1.2.1 Principles of magnetic resonance

Magnetic resonance imaging (MRI) is one of the most powerful methods in clinical diagnosis and has recently emerged as the state-of-the-art method in the field of Molecular Imaging. Compared to other imaging methods, MRI combines high resolution with excellent soft tissue contrast. The underlying physical principle of *nuclear magnetic resonance* (NMR) was discovered by Purcell and Bloch in 1952. 20 years later, Lauterbur and Mansfield invented NMR for imaging^{32,33}. This chapter will describe briefly the physical basics of MRI, including contrast mechanisms and principles for contrast enhancement, and introduce MRI for cell tracking.

The *nuclear magnetic resonance* effect is based on a specific property of certain atomic nuclei, e.g. of the hydrogen nucleus (proton), which have a non-zero nuclear spin. The spin can be imagined as a rotation of the nucleus of non-zero electric charge with a specific frequency, which gives rise to a magnetic moment $\vec{\mu}$, defined as the product of the gyromagnetic ratio γ and the spin \vec{S} . Under normal conditions, the proton spins are oriented randomly (Figure 2 A). After applying an external magnetic field (B_0), the proton spins will preferably align with the external field, which give rise to a macroscopic magnetization (Figure 2 B) and start to precess around the magnetic field axis (M_z) according to the external field with a specific larmor frequency (f), which is proportional to the field strength B_0 : $f = \gamma/2\pi \cdot B_0 \approx 42.57 \text{ MHz/Tesla} \cdot B_0$.

The MRI signal is generated while applying a radiofrequency pulse with larmor frequency, which induces a flip of the M_z magnetization into the plane transverse to B_0 . The transversal magnetization (M_T) is generated, which precess again with larmor frequency (Figure 2C). This rotating magnetization can be recorded by a conductive field coil. Once the radiofrequency pulse is removed, the M_T component will disappear and the nuclei realign until equilibrium M_z state.

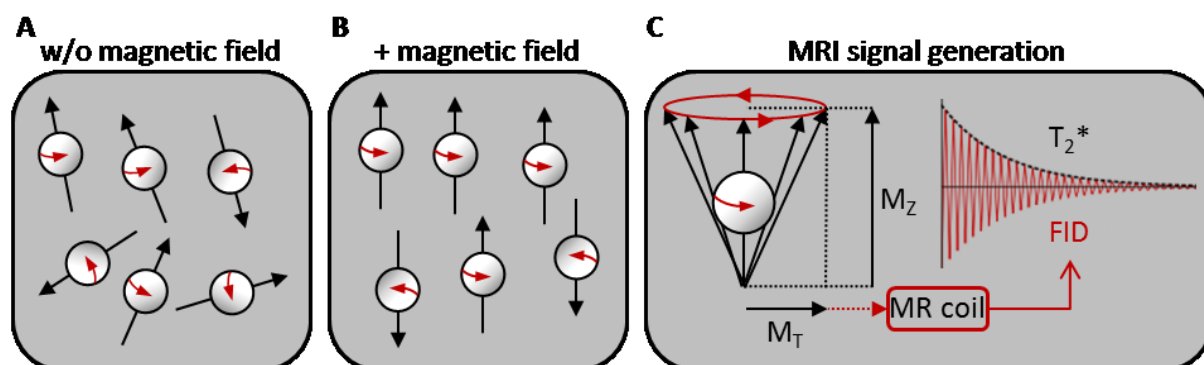


Figure 2: Schematic representation of the spin model for nuclear magnetic resonance. A) Random spin distribution and rotation in magnetic field free environment. B) Spin alignment according to a strong external magnetic field. C) Radiofrequency pulse with the nuclear specific larmor frequency leads to flipping of magnetization into the transverse plane to B_0 . This rotating magnetization M_T can be recorded by a conductive field coil. The decline of M_T with a characteristic decay – the free induction decay (FID) – is illustrated.

The system reaches equilibrium state by two mechanisms: the decline of the transverse component with a characteristic decay – the free induction decay (FID), induced by heterogenous rotation of the transversal spins and the increase of M_z until equilibrium state. The signal decay can be used for contrast generation, because of the relating tissue specific time constants, called relaxation times. The FID decays with the T_2^* relaxation time, which is based on a dephasing of the M_T aligned spins, because of time-constant inhomogeneities of the surrounding B_0 , which results in slightly different Larmor frequencies and diversification of spin direction. Realignment of M_T can be induced by e.g. a refocusing pulse – a process called echo generation. This will exclude the impact of constant inhomogeneities and the signal decays predominantly by energy transfer between the spins and dephasing, resulting in the T_2 relaxation (Figure 3 B).

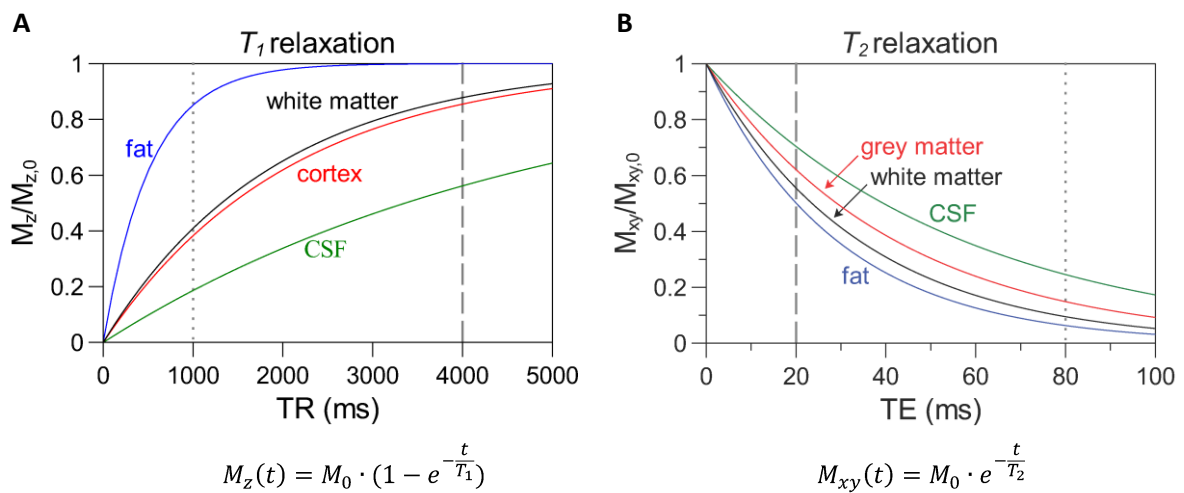


Figure 3: Illustration of T_1 and T_2 relaxation time dependency for fat, cerebrospinal fluid (CSF), cortex and white matter of the rat brain at 11.7 T (values approximated from³⁴). **A** T_1 -weighted images (dotted line indicates strong weighting, dashed line weak weighting) results in hyperintense fat (short T_1) and hypointense CSF (long T_1). **B** T_2 -weighting (strong: dotted line, weak: dashed line) results in hypointense fat (short T_2) and hyperintense CSF (long T_2).

After the radiofrequency pulse, the spins will realign again with B_0 until the M_z equilibrium is reached with the time constant T_1 (Figure 3 A). The T_1 and T_2 relaxation is mathematically described by solutions of the Bloch equations³⁵ (Figure 3), which are used for data fitting. Both relaxation times T_1 and T_2 can be used to maximize soft tissue contrast in MR images based on the parameters for image acquisition, namely repetition time TR and echo time TE. T_1 -weighting is induced with short TR/TE, resulting in hyperintense fat (short T_1) vs hypointense liquids (long T_1). In contrast, long TR and TE values lead to a T_2 -weighted image, in which fat will appear dark (short T_2) and liquids bright (long T_2).

The challenging part of MRI-based cell tracking is to highlight single cells against the host tissue. Nevertheless, cells can be labeled with paramagnetic or superparamagnetic contrast agents to enhance the contrast and enable long-term cell tracking³⁶. The following sections will give a short introduction into MRI sequences and contrast agents used for cell tracking with MRI.

1.2.2 Basic MRI sequences

MRI sequences consist of an ordered combination of radiofrequency pulses (to excite the protons) and gradient pulses to apply local magnetic field changes, which are used for spatial reconstruction.

Gradient Echo Sequence (e.g. FLASH, FISP)

For gradient echo (GE) sequences, a series of radiofrequency pulses is applied separated by the repetition time TR and the data recorded after the echo time TE, phase decoding gradients and during frequency decoding gradients. GE sequences allow rapid imaging with low flip angles (less radiofrequency power), but are sensitive to B0 inhomogeneities and susceptibility artifacts. By adjusting TE and TR, T_2^* , T_1 and proton-density weighted contrast can be achieved. Advanced gradient echo sequences include Fast Low Angle Shot (FLASH), which is optimized for low flip angles at $TR < T_1$ and allows shortening of acquisition time by spoiling of the remaining transverse magnetization. The residual transverse magnetization in gradient echo sequences is used by Fast Imaging with Steady-state Precession (FISP), in which the remaining transversal magnetization is not spoiled but used for gaining high SNR at $TE = TR/2$. Independent of the GE sequence, the choice of a correct flip angle is important for determining T_1 . For each T_1 value an optimal flip angle (“Ernst angle”) exists, which is necessary to achieve highest SNR according to $\alpha_{Ernst} = \cos\alpha - 1 \cdot e^{\left(\frac{-TR}{T_1}\right)}$.

Spin echo sequences (e.g. MSME, RAREVTR)

The spin echo sequences make use of an additional 180° refocusing pulse halfway between the excitation and the echo, which eliminates differences in spin precession, which are introduced by local field inhomogeneities. Therefore, T_2^* -weighting is eliminated and SE sequences allow true T_2 -weighting and high SNR, but require long scan times and use more RF power compared to GEs. For T_1 -weighted images, inversion recovery sequences are often used, which consist of a SE sequence that begins with a 180° pulse for inverting the longitudinal magnetization. After a certain time of inversion (TI), in which the inverted longitudinal magnetization decreases, the 90° excitation pulse is applied. Relaxation during TI is mainly T_1 relaxation time dependent, which enables strong T_1 -weighting with so called inversion recovery sequences. Multi Slice Multi Echo (MSME) sequences consist of an initial 90° pulse and a series of 180° pulses to generate more than one spin echo. For each echo an image can be reconstructed. Using slice selection gradients, excitation and refocusing pulses are applied in an interleaved manner on different slices in order to speed up the acquisition. This can even be accelerated by accumulating over several TE for one image (Rapid Acquisition with Relaxation Enhancement, RARE).

1.2.3 Superparamagnetic contrast agents

Iron oxide contrast agents consist of nanoscale superparamagnetic iron oxide (SPIO) cores encased in a hydrophilic coating composed of poly-saccharides (e.g. Dextran) and synthetic polymers (e.g. silica, or polyvinyl alcohol)³⁷. Such nanoparticles are categorized according to the diameter: <50 nm ultra-small SPIOs (USPIOs) and >50 nm SPIOs³⁸. Due to the magnetic moment of the core in an external magnetic field, they are able to reduce predominantly T_2 and T_2^* relaxation time. When SPIOs are placed in an external magnetic field their moments align in the direction of the magnetic field. This way, substantial disturbances in the local magnetic field are generated, which lead to a rapid dephasing of surrounding protons, thus resulting in a detectable change in MR signal. Iron oxide particles are eliminated by the reticuloendothelial (RES) system), particularly of mononuclear phagocytic cells in the spleen, liver and lymph nodes and subsequently incorporated into the body's iron pool³⁹.

1.2.4 Paramagnetic contrast agents

Most paramagnetic contrast agents contain the lanthanide ion gadolinium Gd(III), which offers seven unpaired electrons resulting in the highest magnetic moment compared to other paramagnetic ions⁴⁰. The Gd(III) is complexed by chemical ligands or chelators to prevent free Gd(III) uptake, which has a toxic effect on biological systems. Paramagnetic relaxation of water protons originates from dipole-dipole interactions between the nuclear spins of the hydrogen nuclei of water molecules and the fluctuating local magnetic field caused by the spins of the unpaired electrons. The resulting effect is seen predominantly as a decrease in T_1 and strongly decreases with distance⁴¹. Detailed theory is provided by the Solomon-Bloembergen equations⁴². The T_1 relaxivity of Gd(III) complexes is primarily determined by three factors: a) the number of water molecules in the inner coordination sphere of Gd(III) q , b) the residence lifetime of these inner-sphere water molecules (how fast they exchange with other water molecules) τ_M , and the rotational correlation time of the agent (how fast the complex tumbles in solution) τ_R (Figure 4).

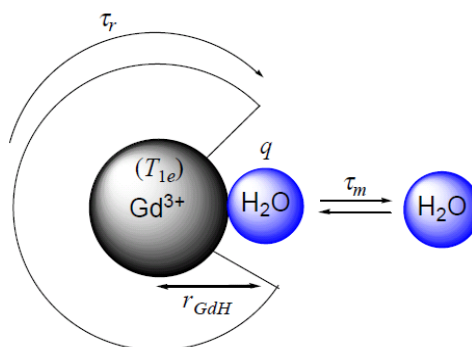


Figure 4: Schematic depiction of the interactions between water molecules and the Gd(III)-based contrast agent. The relaxivity is influenced by the longitudinal electron spin relaxation time T_{1e} , the electron spin-proton distance r_{GdH} , the exchange lifetime τ_M , the number of water molecules q and the and the molecular reorientational time τ_R ⁴¹.

1.2.5 Responsive contrast agents

Responsive contrast agents are the further development of conventional agents. They possess two distinct magnetic states, changed in response to physiological, enzymatic and other metabolic activities. In one concept lanthanide chelates are chemically modified to have one or more potential coordination sites for water blocked in the inactive state and accessible in the active state, as it was invented for the first time by Moats and colleagues⁴³. The relaxivity of this responsive contrast agent is changed by the enzymatic cleavage of a sugar group by the enzyme β -galactosidase, enabling free water access to the paramagnetic ion. Several attempts were made to design contrast agents which are responsive to changes in pH^{44,45}, intracellular calcium concentration⁴⁶, or local oxygen pressure pO_2 ^{47,48} on the in vitro level.

1.2.6 MRI-based cell tracking

Cell tracking using MRI has evolved as an indispensable tool to register the grafted cells in space and time, while exhibiting no or very low adverse effects on the animal physiology⁴⁹. The experimental setup includes 3 major steps: 1) the labeling of (stem) cells with a MRI contrast agent, 2) transplantation of the labeled cells, and 3) the imaging protocol specified for the visualization of the contrast agent labeled cells. The cell labeling procedure must be optimized for every cell type and contrast agent. Potential toxic effects should be monitored.

For histological evaluation, Prussian blue staining of iron oxide-based contrast agents is possible. Additionally, a reliable histological detection is achieved by an internal fluorescent marker (expression of fluorescent reporter or labeled with intracellular dye). For precise monitoring of a biological effect, a sham transplantation is necessary to exclude side effects of the transplantation surgery. Due to the needle penetration of the tissue, inflammation and proliferation of glial cells can be induced.

The highlight of MRI-based cell tracking is the noninvasive monitoring of cell location and migration processes over several months. The resulting images offer information about the anatomical environment and e.g. the structural changes of the stroke lesion, but key cell features, e.g. viability, function and differentiation are neglected. One alternative contrast agent-based method is presented in this dissertation, which enables the discrimination of a specific neuronal population from the background (see 3.).

1.3 Optical imaging basics

Optical imaging comprises a variety of methods to visualize cells and molecular processes by the detection of light emitted by biological light sources with highly sensitive charge-coupled device (CCD) image sensors. Different physical light properties and light interactions with molecules/tissues, e.g. fluorescence, absorption, reflectance or bioluminescence are used for optical imaging. The technical equipment, like sensitive optics, filters and detectors are under permanent development. However, *in vivo* imaging is still limited for cell tracking by the low depth resolution in the mm-range and challenges for signal quantification⁵⁰. Figure 5 summarizes the penetration depth and time-resolution, which differ widely for common optical imaging techniques.

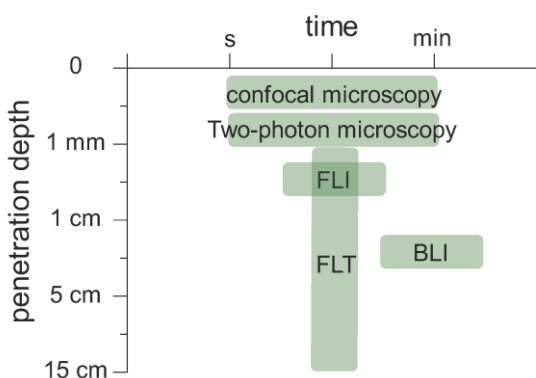


Figure 5: Schematic overview of key-features of selected optical imaging techniques. A) Microscopic techniques are limited by low penetration depth, but can be used to follow fast cellular processes. Fluorescence tomography (FLT), fluorescence imaging (FLI) and bioluminescence imaging (BLI) enable higher tissue penetration, with a time-resolution of seconds to minutes⁵¹.

Three dimensional reconstruction and quantitative determination of the signal source are challenged by the natural barrier for light propagation in a living animal leading producing light absorbance, scattering and autofluorescence. Absorption in the imaging wavelength range (400-1000 nm) is mainly driven by pigments/chromophores (hemoglobin and bilirubin in the blood, myoglobin in the muscles, pheo- and eumelanin in the skin) and also by water and by lipids (Figure 6). A naturally existing window of low absorption appears, which is characterized as the near-infrared (NIR) window (approx. 700-850 nm)⁵². A further impairment is induced by light scattering at inter- and intracellular membrane boundaries due to differences in the refractive index. Light propagation in optically dense media is reduced by the refractive index n (ratio of the speed of light in vacuum and speed of light in the material), ranging from 1.335 (extracellular fluid) to 1.491 (triglycerides)⁵³. These physical effects are of particular importance for optical brain imaging. A multilayer barrier consisting of meninges, bone and skin is covering the brain tissue. Hemoglobin absorption is enhanced because of the high blood to tissue content⁵⁴. The human brain accounts for 2% of the total weight but make use of 20% of total blood flow. Light scattering is induced between grey matter and white matter because of a different refractive index.

In conclusion, the signal intensity in optical imaging is strictly dependent on 1) source depth in the tissue, 2) photons emitted per second, and 3) the wavelength of emitted photons. This results in sensitivity differences for FLI compared to BLI: 10^{15} – 10^{17} mol/L and 10^9 – 10^{12} mol/L respectively⁵⁵.

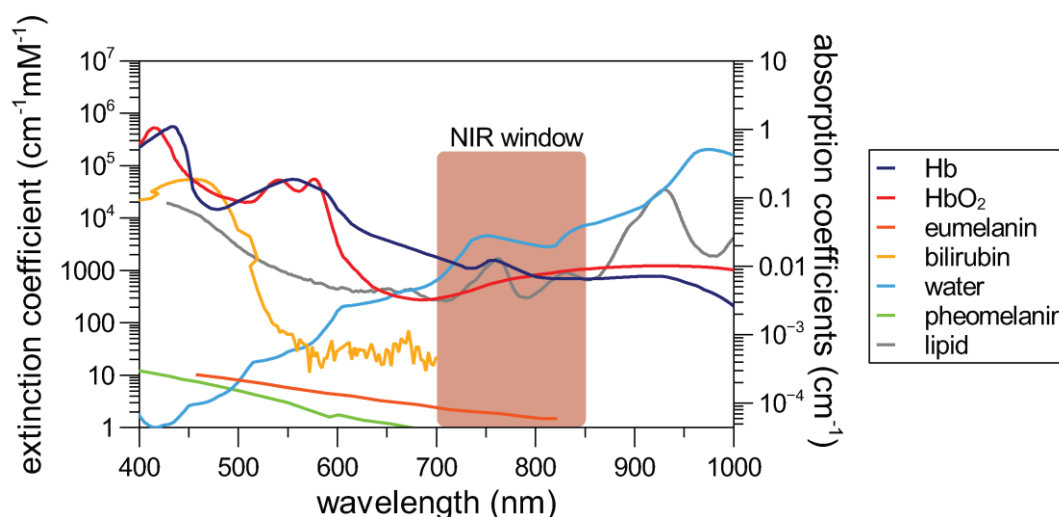


Figure 6: Illustration of the wavelength dependence of the extinction coefficient for hemoglobin and water. Blue to orange light is strongly absorbed by hemoglobin and the infrared range by water leading to a window of low absorption in the near-infrared range optimal for in vivo imaging (original data, see⁵⁶⁻⁶⁰).

1.3.1 Fluorescence imaging

The green fluorescent protein (GFP) was first isolated from *Aequorea Victoria* in 1962⁶¹ and cloned in 1992^{62,63}. The discovery of GFP by Shimomura, Chalfie and Tsien paved the way for the universal use of fluorescence imaging because of the novel unique possibility to visualize structures and processes in living cells and organisms in real-time (Nobel prize in chemistry, 2008). A variety of GFP-like proteins were discovered (Figure 7) from distant species like crustaceans or mutated for different spectral emission⁶⁴. In general, nearly all GFP-like proteins form very stable homotetramers. This naturally occurring oligomerization limits the use as (multicolor) imaging reporter, thus the recently discovered monomeric fluorescent proteins are preferable. The chromophore formation and spectral tuning is strictly dependent on amino acid side chains inside the FP β -barrel, which can be genetically mutated with a single amino acid substitute resulting in a substantial wavelength shift⁶⁵. Nevertheless, the potential for in vivo application is not only dependent on the excitation/emission wavelength, but also on the brightness being determined by quantum yield (QY, the ratio of photons emitted to photons absorbed), the extinction coefficient (EC, determining how strongly light is absorbed), the maturation rate, photostability, pH stability and aggregation potential. EC and QY can be modified by random or site-directed mutagenesis, restricted by the physical barriers of the GFP-like chromophore. The maturation half-time for most fluorescent proteins is between 40 min to 1-2 h, sufficient for the majority of imaging experiments. The photostability defines the time span for imaging and is influenced by the applied imaging method (light intensity, frequency, wavelength). The pH dependence differs for classes from high for yellow, middle for green and low for blue and red emitting proteins.

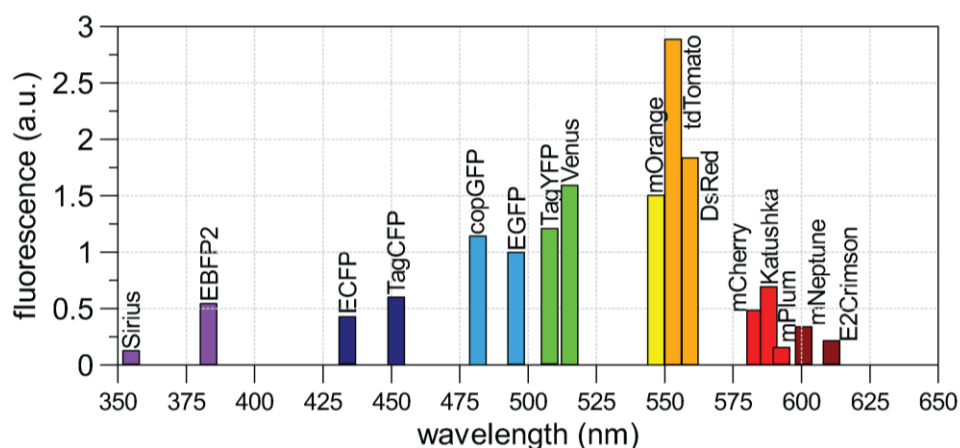


Figure 7: Schematic comparison of selected FPs ranked after the emission maxima in relation to their relative brightness (original values from³¹ and manufacturer's website). To make the fluorescence brightness comparable, quantum yield (QY) and molar extinction coefficient (EC) were multiplied and normalized to EGFP (EC= 55,000 M⁻¹cm⁻¹, QY= 0.6).

1.3.2 Bioluminescence imaging

The bioluminescence effect can be used for imaging thanks to the discovery of the enzyme luciferase from the firefly *Photinus pyralis* in 1978 and successful cloning into mammalian cells. In a naturally occurring form of chemiluminescence, the luciferase (Luc, *Photinus*-luciferin 4-monooxygenase) oxidizes in an ATP-dependent two-step process the substrate D-Luciferin^{II} (Figure 8).

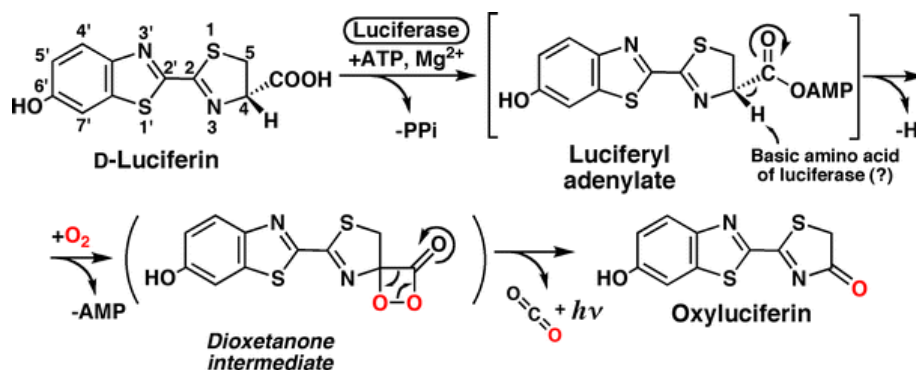


Figure 8: Simplified reaction scheme for the firefly luciferase⁶⁶. In an initial reaction, the enzyme-bound luciferyl adenylate is formed in the presence of Mg²⁺ and ATP. In the second step, an oxygenation of LH₂-AMP leads to the excited state of oxyluciferin, which degrades to the ground state by emission of light in the last reaction step.

Applications for BLI were first developed for in vitro biochemical and molecular assays for fast quantitative measurements of protein interactions and enzyme reactions⁶⁷. Since the first in vivo application for visualizing luciferase gene expression in vivo⁶⁸, the method was continuously developed⁶⁹. A potpourri of different luciferases has emerged from various species and exhibiting different properties (required substrate, wavelength, need or lack of ATP-dependence) (Table 2). Technical and computational advancements enable spectral unmixing of luciferases emitting at different wavelengths, a method which is also applicable in vivo⁷⁰.

^{II} D-Luciferin: (S)-2-(6'-hydroxy-2'-benzothiazolyl)-2-thiazoline-4-carboxylic acid

BLI is beneficial for cell tracking approaches (compared to FLI) because the localization is achieved by the unambiguous light emission from genetically modified cells, and the ATP-dependent enzyme reaction serves as an indicator for cell viability. In addition, quantification is possible based on the relationship between enzyme-substrate complex and photon emission. BLI has been proven in various studies as a valuable imaging reporter for noninvasive monitoring of tumor cells and stem cells in various disease models⁷¹⁻⁷⁴. In vivo BLI approaches are strictly determined by biological factors (e.g. substrate availability) and physical factors (e.g. wavelength), which will be discussed in chapter 4.

Table 2: Properties of luciferases from different species

Luciferase	Species	Emission <i>in vitro</i>	Emission <i>in vivo</i>	Quantum Yield	Substrate	Protein Size	Energy Source	Cofac- tor	Refer- ence
Luc2	<i>Photinus pyralis</i>	562 nm	616 nm	0.44	D-Luciferin	61 kDa	ATP	Mg ²⁺	76
PpYRE9	<i>Photinus pyralis</i>	617 nm	617 nm	N.A.	D-Luciferin	61 kDa	ATP	Mg ²⁺	77
CBG99	<i>Pyrophorus plagi- ophthalmus</i>	546 nm	546 nm	0.62	D-Luciferin	61 kDa	ATP	O ₂	78
GLuc	<i>Gaussia princeps</i>	485 nm	485 nm	N.A.	CTZ-h	20 kDa	substrate	-	79
hRLuc	<i>Renilla reniformis</i>	480 nm	480 nm	0.06	CTZ-h	34 kDa	substrate	-	80
Vluc	<i>Vargula hilgen- dorffii</i>	462 nm	462 nm	0.28	Vargulin	68 kDa	substrate	O ₂	81,82
Cluc	<i>Cypridina noctilu- ca</i>	465 nm	465 nm	N.A.	Vargulin	68 kDa	substrate	O ₂	83

1.3.3 Optical imaging-based cell tracking

An optical imaging-based cell tracking approach can be subdivided into 3 experimental steps: 1) generation of transgenic cells expressing a luciferase and/or fluorescent protein, 2) in vitro cell characterization of the optical properties and the impact of the transgene, and 3) the in vivo application, e.g. transplantation of the cells and subsequent optical tracking in the mouse brain. Following this approach, numerous applications have been reported for bioluminescence-based cell tracking to glioblastomas⁸⁴, ischemic lesions⁸⁵ and multiple sclerosis inflammatory regions⁸⁶. For fluorescent-based brain applications the recent discovery of near-infrared proteins enabled first applications^{87,88}. The GFP fluorescent protein is not suitable for in vivo imaging in the brain and detection ex vivo is limited due to high green tissue autofluorescence and low GFP stability/persistence against histological treatment. The fluorescence proteins used for experiments described in this work belong to a new generation of enhanced green or red fluorescence proteins, exhibiting strong signal also for ex vivo detection. As was pointed out before (1.3), optical imaging in the brain is challenged by the special anatomical compartment and therefore dependent on an optical reporter with highest sensitivity. A complete investigation of optical reporters suitable to meet brain imaging has not been done. The following experimental section will highlight which luciferase works best for optical cell tracking and how fluorescent proteins can be coupled efficiently to serve as histological landmarks.

2. MATERIAL & METHODS

2.1 Devices

Table 3 summarizes the devices for each experimental category (cell culture, molecular biology, protein biochemistry, histology and animal experiments).

Table 3: List of devices sorted according to experimental categories.

Device	Name	Supplier
Cell culture		
Liquid nitrogen tank	Arpege 170	VWR
Electroporator	GenePulser Xcell	Biorad
Incubator	HERA cell 150	ThermoScientific
Centrifuge	Himac CT6E	VWR
Confocal microscope	TCS SP2	Leica
Fluorescence microscope	BZ-9000	Keyence
Laminar cabine	Kojair Biowizard and MSC-Advantage	ThermoScientific
Hotplate stirrer	L-81	Hartenstein
Microplate Reader	Sunrise/ Mithras LB 940	Tecan/Berthold
Light Microscope	Axiovert 4CFL and Axiovert 135	Zeiss
Molecular biology		
Centrifuge	2415/Multifuge 1 S-R	Sigma-Aldrich/Heraeus
Electrophoresis	EasyPhor Midi	Biozym
Gel documentation	Gel Doc XR	Bio-Rad
PCR	GeneAmp PCR System 2400	Perkin-Elmer
qPCR	TProfessional Thermocycler	Biometra
Spectrometer	BioSpectrometer basic	Eppendorf
Thermomixer	Thermomixer comfort	Eppendorf
Protein biochemistry		
SDS electrophoresis	X-Cell Surelock Mini-Cell	Invitrogen
Western blot	X-Cell II blot module	Invitrogen
Histology		
Cryostat	CM3050	Leica
Microscope/ Confocal Microscope	BZ-9000/ TCS SP2	Keyence/ Leica
Animal experiments		
4.7, 7.0 and 11.7 T animal MRI scanner	Biospec47/30, 70/30, 117/16	Bruker BioSpin
BLI camera system	Photon Imager/IVIS spectrum	Biospace/PerkinElmer
Stereotactical instrument	Cat. No. 51600	Stoelting
Mouse Adapter	Cat. No. 51625	Stoelting
Temperature controller	-	medres
Electric Driller	Technobox 810	Bien-Air
Digital navigation system	Cat. No. 51904	Stoelting
Digital injection controller	Micro 4	World Precision Instruments
Hamilton syringe 5µl with 26 G needle	Cat. No. 7634-01, 7732-06	Hamilton
Surgical instruments (scissors, forceps)	Various	FST

2.2 Consumables

The following table summarizes consumables used for the highlighted experiments. Chemicals, which are not listed were purchased exclusively from Sigma-Aldrich and Merck. Standard buffer (PBS, TBS, Tris-HCL) were prepared in aqua bidest according to established recipes⁸⁹. Dilutions of stock solutions for animal experiments were prepared in physiological saline to facilitate physiological distribution. All solutions for cell culture and animal experiments were sterile filtered (0.2 µm filter, VWR). Consumables were stored according to manufacturer recommendations.

Table 4: List of consumables for cell culture, molecular biology, protein biochemistry and animal experiments

Name	Product nr.	Supplier
Cell culture		
Agarose Typ VII-A low-gelling	A0701	Sigma-Aldrich-Aldrich
Agarose	A9539	Sigma-Aldrich-Aldrich
Accutase	L11-007	PAA
B27 Supplement (50x)	17504	Gibco
beta-mercaptoethanol (50mM)	31350, 50 mM	Gibco
BSA	K31-011	PAA
Cell culture plates, flasks, (Pasteur)	various	Brand, Greiner, Nunc, Sarstedt and
D-Luciferin sodium salt, 99%	bc218	Synchem
DMEM high Glucose (4,5g/l)	E15-883	PAA
DMEM/F12 (1:1)	31330-038	Gibco
Dotarem®	-	Guerbet
EZ-PCR Mycoplasma kit	20-700-10	WKS Diagnostik
EGF-human	AF-100-15	PreproTech
Euromed	ECL-ECM0883L	Biozol
FBS/FBS ES-cell tested	A15-101/ Lot 751710	PAA/Gibco
FGF-human	AF-100-18B	PreproTech
G418 (Neomycin)	P25-011	PAA
Gelatine 2%	G1393	Sigma-Aldrich
Glutamin	M11-004, 200 mM	PAA
GMEM 1x	21710025	Gibco
HBSS 1x	14170	Gibco
Insulin human, rekombinant (10mg/ml)	I9278	Sigma-Aldrich
ITS (100x)	I3146-5ml	Sigma-Aldrich
Laminin (1mg/2ml)	11 243 217 001	Roche
LIF (10 ⁶ Units)	ESG1106, 106units/ml	Millipore
Lipofectamin LTX + Plus Reagent Kit	15338-100	Invitrogen
N2-Supplement (100x)	17502-048	Gibco
Mycoplasma Test Kit	20-700-20	Biological Industries
NEAA (100x)	M11-003	PAA
Neurobasal	21103	Gibco
Nickel	72247	Sigma-Aldrich
Optimem	11058-021	Gibco
Penicillin/Streptomycin	P11-010	PAA

Name	Product nr.	Supplier
Cell culture		
PBS with Mg ²⁺ /Ca ²⁺	H15-001	PAA
PBS w/o Mg ²⁺ /Ca ²⁺	H15-002	PAA
Poly-L-Ornithin	P4957	Sigma-Aldrich
PrestoBlue	A-13261	Invitrogen
Sodium pyruvate	P3662	Sigma-Aldrich
Trypan blue	93595	Sigma-Aldrich
Trypsin/EDTA	11-004	PAA
Zeocin	R250-01	Invitrogen
Molecular biology		
DEPC	K028.2	Roth
DNA Polymerization Mix 10 (dNTPs)	GC-013-004	GeneCraft
dTT	R0861	Fermentas
FastDigest restriction enzymes	various	Fermentas
Gel Extraction Kit	287704	Qiagen
LE Agarose	840004	Biozym
LB Medium	A6666	AppliChem
Mass Ruler 6x loading dye	RO621	Fermentas
Mass Ruler DNA ladder	SMO403	Fermentas
Midori Green	617002	Biozym
Nucleo Spin Gelextractin Kit	74060950	Machery-Nagel
Nucleo Spin RNA II	74095550	Machery-Nagel
Oligo dT	79237	Qiagen
Omniscript RT Kit	205111	Qiagen
Phusion Hot Start Polymerase	F540s	Finnzymes
Plasmid Midi Kit	12243	Qiagen
Plasmid Mini Kit	27106	Qiagen
Rapid Dephos + Ligation Kit	4898117001	Roche
SensiMix No-Rox	OT650-05	Bioline
T4- DNA-Ligase	10716359001	Roche
Protein biochemistry		
AOAA	C13408	Sigma-Aldrich
Amersham Hyperfilm ECL	28906839	GE Healthcare
BCA protein assay	23221	Thermo-Scientific
Cell Lysis Buffer	9803	Cell Signaling
Complete protease inhibitor cocktail	04 693 159 001	Roche
ECL solution	RPN2209	GE Healthcare
M-PER lysis buffer	78503	Thermo-Scientific
Novex 8-16% Tris-Glycine Mini Gels	EC6045BOX	Invitrogen
PageRuler Plus	SM1811	Fermentas
Protran Nitrocellulose Membrane	10402506	Whatman
PLP	P9255	Sigma-Aldrich
Restore Plus Stripping buffer	10016433	Thermo-Scientific
TBS-Tween tablets	524753-1EA	Merck Chemicals

Name	Product nr.	Supplier
Histology		
Alkaline Phosphatase Detection Kit	SCR004	Millipore
Glass ware	various	VWR
Mounting Medium	Aqua-mount	Thermo-Scientific
Microscope Slides	4951PLUS	Thermo-Scientific
Animal experiments		
Carprofen	Rimadyl®	Pfizer
Coelenterazine-h, Rediject	760506	PerkinElmer
D-Luciferin, sodium salt	bc218	Synchem
Isoflurane	Isoflurane	Abbott
Hamilton syringe 5µl with 23 G needle	7634-01, 7732-06	Hamilton
Ketamine	Ketavet	Pfizer
Physiological saline	NaCl 0.9%	Braun
Pentobarbital	PTB-537-NA	Lipomed
Surgical instruments (scissors, forceps)	Various	FST
Suture (non-colored)	PGA Resoquick 5/0 USP	Resorba
Syringes and needles	various	Braun
Xylazine	Rompun®	Bayer

2.3 Molecular Biology

2.3.1 Cloning of imaging reporter plasmids

Lenti- and retroviral plasmids (Table 5) were cloned by amplification of the gene of interest with specific primer (Table 5) with Phusion DNA Polymerase designed to fit the FastDigest restriction enzymes necessary for ligation with the plasmid backbone (protocols used according to manufacturer's specifications). The following plasmids were donated or purchased: pBabe-neo-GIT (generous gift of A. Jacobs, European Institute for Molecular Imaging, Münster, Germany), pcDH and pPACKH1 (Biotac, Heidelberg, Germany), pGL (Promega, Madison, USA) pGex and phu (generous gift of L. Mezzanotte and E. Kaijzel, Leiden University Medical Center, Leiden, Netherlands), pDRIVE (Invivogen, San Diego, USA) and pCH (generous gift of Rob Hoeben, Leiden University Medical Center, Leiden, Netherlands).

The HIV-1 derived lentiviral vector included the following parts:

- **Multiple Cloning Site (MCS)**
- **EF1alpha promoter** - constitutive promoter for highly efficient expression⁹⁰
- **T2A** - self-cleaving 2A-like peptide sequence for efficient multicistronic reporter expression
- **WPRE element** - enhances stability and translation
- **SV40 polyadenylation signal** - enables efficient termination of transcription
- **Hybrid RSV/5LTR promoter** - provides high level of expression of full-length viral transcript
- **Genetic elements (cPPT, gag, env, LTRs)** - necessary for packaging, transducing, and integrating of the viral expression construct into genomic DNA

- **SV40 origin** - for stable propagation of the pCDH plasmid in mammalian cells
- **pUC origin** - for high copy replication and maintenance of the plasmid in *E.coli* cells
- **Ampicillin resistance gene** - for selection in *E.coli* cells.

The lentiviral expression vectors are combined with the pPACKH1 plasmid mix containing 3 plasmids for the structural (gag), replication (pol), regulatory protein (rev) and the envelope glycoprotein of vesicular stomatitis virus (VSV-G)⁹¹. By combination of the expression vector and the pPACKH1 mix during the transduction process, pseudoviral particles are produced, which can infect mammalian and non-mammalian target cells (amphotropic virus) but cannot replicate (biosafety level 2).

The retroviral expression vector pBabe is derived from Moloney murine leukemia virus (MMLV) and produces only in combination with the packaging cell line Plat-E⁹² (bearing the viral structural genes) pseudoviral particles. Based on the MMLV envelope protein, these particles have a limited host range (mouse) and refer to an ecotropic virus (biosafety level 1).

The following cDNAs were used to modify the backbone plasmids: the human GFAP promoter, the luciferases (Luc2, PpyRe9, CBG99 and hRluc) and the fluorescent proteins mCherry from *Discosoma sp.* and copGFP from *Pontenilla plumata*. Modified plasmids were verified by sequencing (GATC Biotech, Konstanz, Germany) with primer pairs flanking the gene of insert. All generated imaging reporter plasmids are listed in Table 5 with the associated PCR primer pairs used for cloning in Table 6.

Table 5: Overview of cloning strategy for imaging reporter plasmids

Plasmid	Insert	Backbone origin	Insert origin	Restriction
pcDH-pBabe-Luc2-T2A-copGFP-Neo	Luc2	pBabe-Neo-GIT	pcDH-EF1-Luc2-T2A-copGFP	EcoRI/Sall
pcDH-EF1-Luc2-T2A-copGFP	Luc2	EF1-MCS-T2A-copGFP	pGL4.14	BamHI/NotI
pcDH-EF1-PpyRe9-T2A-copGFP	PpyRe9	EF1-MCS-T2A-copGFP	pGex-Pret9	BamHI/NotI
pcDH-EF1-CBG99-T2A-copGFP	CBG99	EF1-MCS-T2A-copGFP	pGL3 CBG99	NotI/BamHI
pcDH-EF1-hRluc-T2A-copGFP	hRluc	EF1-MCS-T2A-copGFP	hRluc PCR (from pGL4 hRluc)	XbaI/BamHI
pcDH-EF1-Luc2-T2A-mCherry	mCherry	EF1-Luc2-T2A-cop GFP	mCherry PCR (from phu-DCX 3509-	BspEI / Sall
pCDH-GFAP-T2A-Puro	GFAP promoter	EF1-MCS-T2A-Puro	GFAP PCR (from pDRIVE-hGFAP)	Clal/XbaI
pcDH-GFAP-P2A-T2A-Puro	P2A	GFAP-T2A-Puro	pCH-CMV-eGFP-P2A-fluc	EcoRI/BamH1
pcDH-GFAP-Luc2-P2A-mCherry-T2A-Puro	Luc2	GFAP-P2A-T2A-mCherry-Puro	Luc2 PCR (from pGL4.14)	EcoRI/XbaI
pcDH-GFAP-Luc2-T2A-mCherry	GFAP promoter	EF1-Luc2-T2A-mCherry	pcDH-GFAP-MCS-T2A-cop GFP	Clal/XbaI
pcDH-GFAP-Luc2-T2A-mCherry-SV40-Zeo	SV40-Zeo	GFAP-Luc2-T2A-mCherry	pBabe-SV40-Zeo	KpnI

Table 6: PCR primer pairs for cloning

Name	Sequence 5'-3'	Length (bp)	CG-content (%)	Tm (°C)
Luc2_BamHI_for	AAGGGAAAGGATCCGCCACCatggaagatgcaaaaacattaag	44	46	73
Luc2_NotI_rev	AAATTTGCGGCCGCcacggcgtcttgc	28	61	71
PpyRe9_BamHI_for	AAGGAAAAAGGATCCGCCACCatggaggacgccaag	36	56	74
PpyRe9_NotI_rev	AAATTTGCGGCCGCgctcttgcgccc	27	63	71
CBG99_BamHI_for	AAG GGA AAA GGA TCC GCC ACC atg gtg aag cgt gag	36	56	74
CBG99_NotI_rev	TAAAA GCGGCCGC acc gcc ggc	22	73	70
hRluc_XbaI_for	AAG GGA AAA TCTAGA GCC ACC atg gct tcc aag	33	49	64
hRluc_BamHI_rev	TAAAAGCC GGATCC ctg ctc gtt ctt cag	29	52	68
mCherry_BamHI_for	AAGGGAAAAAGGATCCAATGgtgagcaagg	30	47	63
mCherry_BamHI_rev	AAATTCTCGGATCCCTTGACAGCTCGTCC	30	50	64
mCherry_BspEI_for	AAGGGAAAAATCCGGAAtg gtg agc aag	28	46	61
mCherry_Sall_rev	TAAAAGCCGTCGACTtactgtacagctcg	30	47	61
P2A_EcoRI_for	AAGGGAAAAAGAATTCGGTGGTGGCTCGG	29	52	64
P2A_BamHI_rev	TAATTGCGGGATCCTGGTCCGGGATTCTC	29	55	64
GFAP_ClaI_for	AAGGGAAAAATCGATgtctgcaagcagacctgg	34	47	70
GFAP_XbaI_rev	TAAAAGCCTCTAGAtgtctgtgctctgctcg	32	50	70
SV40-Zeo_KpnI_for	ATGGGATATATGGTACCctgtggaatgtg	30	46	62
SV40-Zeo_KpnI_rev	TAATTGCCGGTACCctgcatcggtcag	26	53	63

2.3.2 Qualitative identification of gene expression with PCR

The primer pairs for PCR were designed using the Primer-Blast tool from the National Center for Biotechnology Information (NCBI, Bethesda, USA) – whenever possible selected primer pairs span exon-exon junctions in the reference sequence (Table 7). Actin was used as reference. Lineage marker were selected according to manufacturer's recommendation and literature data⁹³.

Table 7: Properties of PCR primer pairs for identification of gene expression in mouse cells.

Name	Sequence 5'-3'	Length (bp)	GC-content (%)	Tm (°C)	Product (bp)	Accession Nr.
5T4 for	AACTGCCGAGTCTCAGATACC	21	52	53	506	NM_011627.4
5T4 rev	ATGATACCCTTCATGTGATCC	22	46	51		
Actin for	CAGGTCATCACTATTGGCAA	20	45	49	574	NM_007393.3
Actin rev	ATCGTACTCCTGCTTGCTGA	20	50	50		
Brachyury for	TGCTTTCCCAGACCCAGTT	20	55	61	303	NM_009309.2
Brachyury rev	CCGGTGGTTCCTTAGAGCTG	20	60	60		
BLBP for	ATGAAAGCTCTGGGCGTGGGC	21	62	60	322	NM_021272.3
BLBP rev	AGCGAACAGCAACGATATCCCCA	23	52	59		
DCX for	TTTCTACCGCAATGGGGACC	20	55	60	897	AF045547.1
DCX rev	AATGACAGCGGCAGGTACAG	20	55	60		
Galc for	CGTGAGCACCGCTTACGCT	20	65	60	130	NM_008079.3
Galc rev	ATGTTGGTCCAGTGGTGATCGCC	23	56	59		
GATA6 for	AAACTGAGCCCCTTCGCGGC	20	65	60	765	NM_010258
GATA6 rev	GGAGCCGCAGTTCACGCACT	20	65	60		

Name	Sequence 5'-3'	Length (bp)	GC-content (%)	Tm (°C)	Product (bp)	Accession Nr.
GFAP for	AAGAGACAGAGGAGTGGTAT	20	45	49	518	NM_010277.3
GFAP rev	GTCCTTAATGACCTCACCAT	20	45	49		
Musashi1 for	ATGCCTTCATGCTGGGTATT	20	45	57	118	NM_008629.1
Musashi1 rev	CGGAATTCGGGGAAGTGGTA	20	55	60		
Nanog for	TGCTCTTTCTGTGGGAAGGCTGC	23	56	60	899	NM_028016.2
Nanog rev	AGCATTCCAAGGCTGGCCGTT	21	57	60		
Nestin for	TGTCAAGGTCCAGGATGTCA	20	50	58	335	NM_016701.3
Nestin rev	GCTCTAGTCCATTCTCCATC	20	50	55		
NeuroD1 for	TTCGCCACGCAGAAGGCAA	20	60	60	653	NM_010894.2
NeuroD1 rev	CAGGCAGCCGGCGACCAAT	20	65	60		
NF-h for	TCTGAACGACCGCTTCGCGG	20	65	60	587	NM_010904.3
NF-h rev	GGTCCAACCTCACTCGGAACCAC	23	60	60		
Oct4 for	GCCCTGCAGAAGGAGCTAGAAC	22	59	63	459	NM_013633.1
Oct4 rev	GGAATACTCAATACTTGATCT	21	33	50		
Olig2 for	ACAGACCGAGCCAACACCAGCGC	23	65	63	546	NM_016967.2
Olig2 rev	CCCGTGCAGCTAAGGCATGAC	21	66	61		
Pax6 for	GGCAACCCACGCAAGATGGC	20	65	60	454	NM_013627.4
Pax6 rev	GCGGTGTCTGTTCCGGCCAA	20	65	60		
Prominin 1 for	TCCTGTGCAGCAATCACTGA	20	54	60	445	NM_008935.2
Prominin 1 rev	CACAGTCTCAACATCGTCGT	20	52	60		
Rex-1 for	TGACCCTAAAGCAAGACG	18	50	54	414	NM_009556.3
Rex-1 rev	ATAAGACACCACAGTACACACC	22	45.5	57		
S100beta for	AGCAGCAAAGGTGACCAG-	25	60	62	555	NM_009115.3
S100beta rev	GGGACCAGTCAGCTCACGGGA	21	67	60		
Sox1 for	TTACTTCCCAGCTCTTC	20	55	54	555	NM_009233.3
Sox1 rev	TGATGCATTTTGGGGTATCTCTC	24	46	55		
Sox2 for	TGCTGCCTCTTAAGACTAGGGCT	24	50	57	506	NM_011443.3
Sox2 rev	CTGCCCCGGGACCATACCA	20	70	60		
Synaptophysin for	GCCTGTCTCCTTGAACACGAAC	22	55	65	287	NM_009305.2
Synaptophysin rev	TACCGAGAGAACAACAAGGGC	22	50	64		

The protocol for conventional detection of gene expression by RT-PCR included 1) the total RNA extraction, 2) single strand cDNA synthesis with 5 µg of purified total RNA, 3) the PCR reaction mix (Table 8), 4) the PCR run (initial denaturation 98°C 30 s, 35 cycles of Denaturation 98°C 5 s – Annealing TM=55-60°C 30 s – extension 72°C 30 s and the final extension 72°C 10 min) and 5) the evaluation after electrophoresis (1% agarose gel, TrisHCL, 100 V, 45 min).

Table 8: PCR mix

Component	Final concentration	Volume (µl)
H ₂ O, PCR grade	-	10.8
MgCl ₂ (stock 25 mM)	3 mM	0
PCR primer forward (stock 10 µM)	500 nM	1
PCR primer reverse (stock 10 µM)	500 nM	1
5x Phusion HF buffer	1x	4
dNTPs (stock 10 mM)	200 µM	0.4
DMSO		0.6
Phusion		0.2
total volume		18
mix 2 µl DNA (100 ng) with 18 µl the reaction mix		

2.3.3 Quantification of gene expression with qPCR

The qPCR primer pairs were selected with the QuantPrime⁹⁴ software and selected for high specificity based on NCBI mouse reference sequences. GAPDH was chosen as housekeeping gene, because of the reported stable expression in mouse embryonic stem cells and neural differentiation protocols⁹⁵.

Table 9: Properties of qPCR primer pairs for quantification of gene expression in mouse cells.

Name	Sequence 5'-3'	Length	CG-content	Tm (°C)	Accession Nr.
qDCX for	TGGAAACAGCCCACCTTTCTG	22	55	56.7	NM_001110222
qDCX rev	ACCATGCATTTACTCTCCAAAGGC	24	46	55.7	
qGAD1 for	CAGCCAGACAAGCAGTATGACG	22	55	57	NM_008077.4
qGAD1 rev	TTGCTTTCCACATCAGCCAGAAC	23	48	57	
qGAD2 for	ACCACAATGGTCAGCTACCAACC	23	52	57	NM_008078.2
qGAD2 rev	TTTGAGATGACCATGCGGAAGAAG	24	46	56	
qGAPDH for	CATGGCCTTCCGTGTTCTTA	20	55	54	NM_008084.2
qGAPDH rev	GCGGCACGTCAGATCCA	17	65	52	
qGFAP for	TCAATGCTGGCTTCAAGGAGAC	22	50	54.8	NM_010277.3
qGFAP rev	CATTGAGCTCCATCATCTCTGCAC	24	50	57.4	
qGlast for	TTGGCATTGGCAGAGGACCAAC	22	54.5	62.9	NM_148938.3
qGlast rev	AGTAGAGGAGATCAGCCTCCTGTC	24	54.2	60.4	
qMAP2 for	AGCAGGATGACGGGTGAAATC	22	54.4	63.3	NM_001039934.1
qMAP2 rev	AGCTACCTCAGCCAAACTGAGC	23	52.2	63.4	
qNestin for	AGTGCTACATACAGGACTCTGC	23	52	57.1	NM_016701.3
qNestin rev	TTCTCCAGGTGTCTGCAAGCG	22	55	56.7	
qOct4 for	TGTTTCTGAAGTGCCGAAGCC	22	55	56.7	NM_013633.3
qOct4 rev	CCAAGCTGATTGGCGATGTGAG	22	55	56.7	
qS100beta for	TGGCTGCGGAAGTTGAGATTAC	23	52.2	62.4	NM_009115.3
qS100beta rev	TCCCAGCAGCTAAAGGACACAC	22	54.5	62.1	
qSynaptophysin for	CCAGAACGGACATAACCTGGGAAG	24	54.2	63.3	NM_009305.2
qSynaptophysin rev	ACATTTGCTCACCTCCAAACC	23	52.2	63.9	
qTubb3 for	ATGAGGCCTCTCTACAAGTATG	24	50	57.4	NM_023279.2
qTubb3 rev	TTCCAGGTTCCAAGTCCACCAG	22	55	56.7	

The protocol for quantification of gene expression consisted of the 1) cDNA preparation (see 1.3.2), 2) the reaction mix (Table 10) with the SensiMix SYBR No-ROX kit including a dilution series of cDNA-mix from all samples for determining primer-specific PCR efficiency (2.5-100 ng) and the single cDNAs (100 ng per reaction) in triplicate and 3) the PCR run (initial denaturation 95°C 10 min, 40 cycles of denaturation 95°C 15 s – Annealing TM=58-62°C optimized for each primer pair for 15 s – extension 72°C, melting curve at the end of the amplification from 65 to 99°C with $\Delta T=1^\circ\text{C}$, heating rate= 1°C/s). Data was evaluated using the software PCRsoft V1.1 and the Relative Expression Software Tool V2.0.13⁹⁶. Relative quantification based on the $\Delta\Delta\text{CT}$ method was achieved by determining the PCR efficiencies for each primer pair with the cycle threshold (CT) values from the cDNA-mix and CT values for each specific gene. Results were calculated in relation to the housekeeping gene GAPDH.

Table 10: qPCR reaction mix

Component	Final concentration	Volume (μ l)
H ₂ O, PCR grade	-	7
MgCl ₂ , stock solution, 25	3 mM	0
PCR primer forward, 10 μ M	500 nM	1
PCR primer reverse, 10 μ M	500 nM	1
DNA master mix 2x	1x	9
total volume		18
mix 2 μ l cDNA (100 ng) with the reaction mix		

2.3.4 Protein Biochemistry

Western blot

Western blot analysis was performed using as standardized setup with commercially available consumables (see Table 4)¹¹¹. For cell lysates, 2-3x10⁶ cells were washed with ice-cold PBS and scraped from the plate with 4 ml/cm² with complete lysis buffer (10 ml stock: 9 ml 1x Cell Lysis Buffer + 5 μ l PMSF + Protease inhibitor cocktail tablet). The mixture was kept on ice for 30 min and vortexed occasionally, followed by 20 min centrifugation (20,000 xg, 4°C). The resultant supernatant contained the proteins, which were measured with the BCA protein assay at 570 nm in 96-well plates. For each protein analysis, 30 μ g of total lysate protein were subjected to SDS-polyacrylamide gel electrophoresis and transferred to nitrocellulose membranes⁹⁷. Membranes were blocked with 5% non-fat dry milk in TBST for 1 h. Immunolabeling of the blots occurred overnight at 4°C with the primary antibody, followed by the HRP-coupled secondary antibody for 1 h at RT (Table 11). Immunolabeling was detected on an X-ray film using the ECL developer solution. For evaluation of the X-ray films, ImageJ was used (Version 1.42q; National Institutes of Health) to determine the integrated density of the protein-of-interest bands in relation to the actin or alpha-tubulin bands as loading control.

Table 11: List of antibodies used for western blot analysis

Antigen	Host	Dilution	Product-nr.	Supplier
alpha-Tubulin	Mouse	1:5000	CP06	Calbiochem
beta-Actin	Rabbit	1:5000	PM053	MBL
copGFP	Rabbit	1:10000	AB501-EV	Biocat
Goat anti mouse HRP	Goat	1:5000	12-349	Millipore
Goat anti rabbit HRP	Goat	1:5000	7074	Cell Signaling
Goat anti rat HRP	goat	1:5000	AP136P	Millipore
Rluc	Mouse		MAB4410	Millipore
GAD65/67	Rabbit	1:750	ab1511	PAA

¹¹¹ Western blot of tissue lysates were obtained according to a modified-protocol including a different lysis buffer, for details see¹¹⁴.

Tissue lysates for contrast agent assessment

For contrast agent activation tests with lysates, rat tissues (liver, cortex and cerebellum) were mechanically homogenized, and lysed with M-PER lysis reagent according to the manufacturer's protocol. M-PER is a non-denaturing agent, preserving protein structure, which makes it compatible with enzyme assays. The protein content was determined and lysates subsequently frozen at -80°C to avoid protein degradation. Equal amounts of total protein (3-3.5 mg) were incubated with the contrast agent and 0.05 mM of the cofactor pyridoxal-5'-phosphate (PLP) in PBS buffered solution. For selective inhibition of the GAD enzyme, the carbonyl-trapping agent aminoxyacetic acid was used at 250 μM concentration.

2.4 Cell culture

2.4.1 Cell lines

All cell lines were stored in liquid nitrogen tanks and tested regularly for the contamination with mycoplasma using the mycoplasma test kit according to manufacturer's protocol. Table 12 gives a short overview of cell lines used for the experiments including the references of the first description in the literature. A morphological comparison of the major cell lines is visualized in Figure 9 and Figure 10. The CGR8 cells were a generous gift from A. Sachinidis (University Cologne, Germany), the D3WT from T. Saric (University Cologne, Germany) and the GL261 from A. Jacobs (EIMI, University Münster, Germany).

Table 12: List of experimentally used cell lines

Name	Species	Description	Reference
HEK-293(T)	Human	Embryonic kidney cells, immortalized with sheared adenovirus	98
C17.2	Mouse	Neural stem cell line, immortalized by retrovirus-mediated v-myc transfer	99
CGR8	Mouse	Embryonic stem cells (129/Ola derived)	100
D3WT	Mouse	Embryonic stem cells (129S2/SvPas derived)	101
D3WT_N2Euro#4	Mouse	Neural stem cells, derived from D3WT	-
GL261	Mouse	Glioblastoma cell line (C57BL/6 derived)	102
Plat-E	Human	Packaging cell line optimized for high efficient packaging of retroviruses	92
U373	Human	Glioblastoma-astrocytoma - grade III- cell line derived from human (Caucasian, male, 61 years old)	103

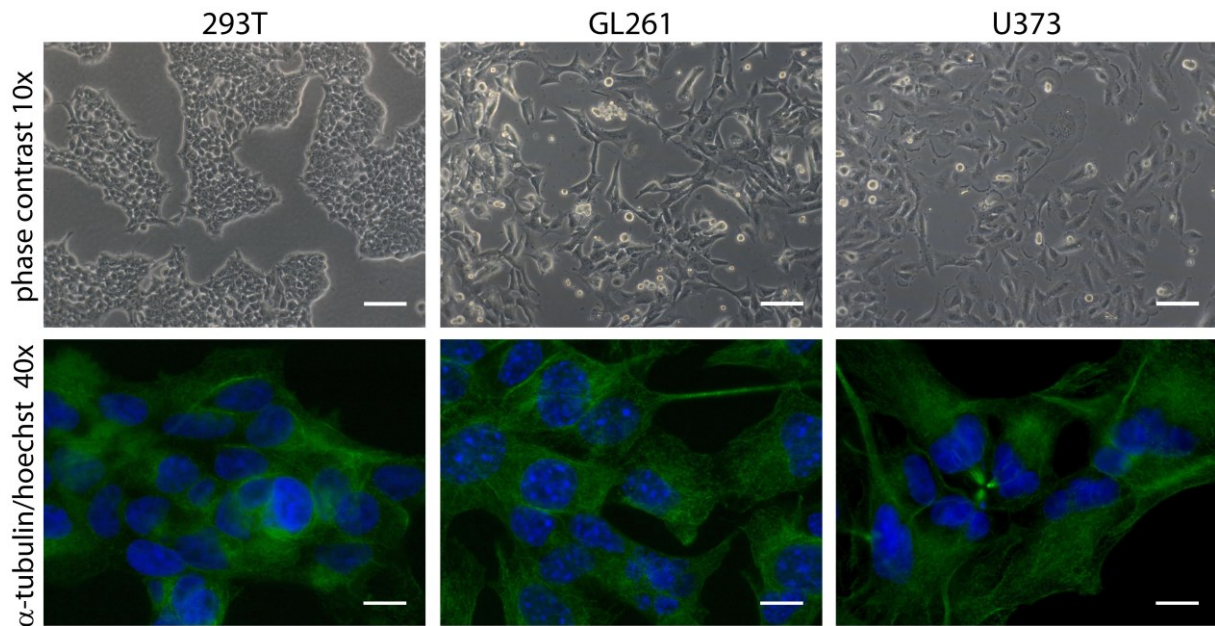


Figure 9: Morphological characterization of tumor cell lines. 293T, GL261 and U373 show unique morphology under phase contrast microscopy (scale bar 100 μm). B) ICC for α -tubulin (green) counterstained with Hoechst reveal cytoarchitectural differences (scale bar 20 μm).

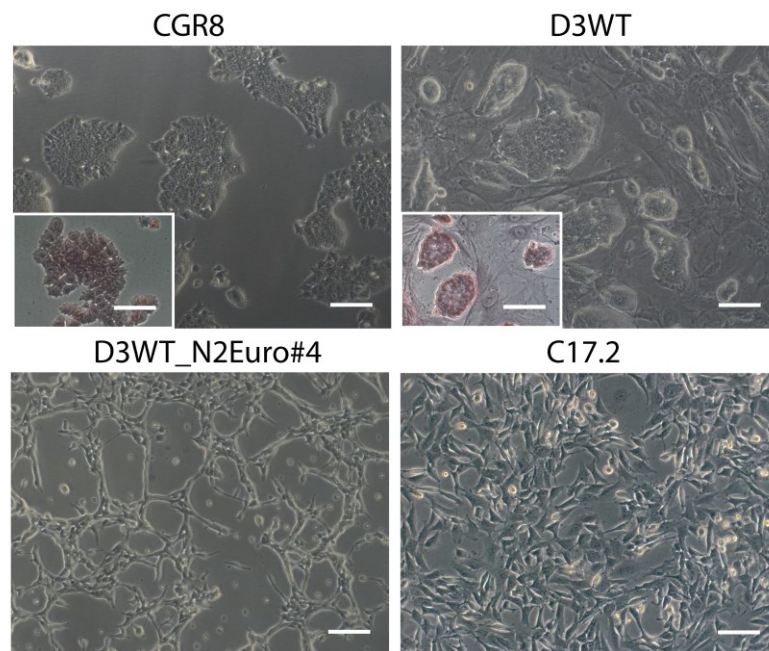


Figure 10: Morphological characterization of embryonic and neural stem cell lines. A) CGR8 cells and D3WT exhibit the unique embryonic stem cell colony formation – a dense package of homogeneous round cells growing on gelatin coating and feeder layer, respectively. Small framed pictures show the alkaline phosphatase staining, which specifically highlights embryonic stem cells as red/purple cells. B) The neural stem cell lines D3WT_N2Euro#4 and C17.2 are characterized by a bipolar and epithelial morphology, respectively (scale bar 100 μm).

2.4.2 Cell culture media, supplements and coatings

The following tables summarize the composition for each cell culture media (Table 13, calculations for a total volume of 50 ml) and cell culture plate coatings (Table 14), indicated by a characteristic short name, which is used throughout the text. The media containing growth factors or instable supplements (e.g. N2) were freshly prepared before use and stored not longer than 1 week at 4°C. Supplementation with antibiotics Penicillin/Streptomycin (P/S) was not used for stem cell culture media except selection of transduced cells with zeocin (250 µg/ml), or G418 (200 µg/ml).

Table 13: Cell culture media composition

Component	Final concentration	Volume	Component	Final concentration	Volume
<u>GMEM FCS*</u>			<u>DMEM FCS</u>		
GMEM		44.0 ml	DMEM		44.5 ml
FCS* (ES-cell tested)	10% (v/v)	5.0 ml	FCS	10% (v/v)	5.0 ml
L-Glutamine	2 mM	0.5 ml	L-Glutamine	2 mM	0.5 ml
LIF	100 units/ml	5.0 µl	P/S	1x	0.5 ml
beta-mercaptoethanol	50 µM	50.0 µl			
<u>DMEM FCS*</u>			<u>N2/B27</u>		
DMEM		41.4 ml	Neurobasal		24.2 ml
NEAA	1x	0.5 ml	DMEM/F12		24.45 ml
L-Glutamine	2 mM	0.5 ml	B27	1x	0.5 ml
FCS* (ES-cell tested)	15% (v/v)	7.5 ml	N2	1x	0.25 ml
LIF	1000 units/ml	50.0 µl	L-Glutamine	2 mM	0.5 ml
beta-mercaptoethanol	50 µM	50.0 µl	beta-	100 µM	100.0 µl
<u>ITSFN</u>			<u>DMEM FCS/HS</u>		
DMEM/F12		49 ml	FCS	10% (v/v)	5.0 ml
L-Glutamine	2 mM	0.5 ml	HS	5% (v/v)	2.5 ml
ITS	1x	0.5 ml	L-Glutamine	2 mM	0.5 ml
			Sodium pyruvate	1x	0.5 ml
<u>D3N2Euro</u>			<u>D3N2Euro FCS</u>		
Euromed		48.275 ml	Euromed		47.875 ml
L-Glutamine	2 mM	0.5 ml	L-Glutamine	2 mM	0.5 ml
N2	1x	0.5 ml	N2	1x	0.5 ml
BSA	50 µg/ml	0.5 ml	BSA	0.5 µg/ml	0.5 ml
Insulin	25 µg/ml	125.0 µl	Insulin	25 µg/ml	125.0 µl
b-FGF	10 ng/ml	5.0 µl	FCS	1% (v/v)	0.5 ml
EGF	10 ng/ml	5.0 µl			

Table 14: Coating procedure for cell culture plates

Coating	Material	Procedure
Gelatine	0.2% in PBS (with Ca ²⁺ /Mg ²⁺)	Incubate plate with 100 µl/cm ² at 37°C min. 30 min, wash 1x with PBS
Poly-L-Ornithin/Laminin (POLA)	178.6 µl/ml PO, LA 1:100 in PBS (with Ca ²⁺ /Mg ²⁺)	Incubate plate with 100 µl/cm ² at 37°C min. 4 h, wash 1x with PBS

2.4.3 Cell culture protocols

Cells were incubated under humidified atmosphere with 5% CO₂ with exception of those experiments under hypoxia (2% O₂). Cell counting was done using a Neubauer chamber and the Trypan blue dye with respect to the formula: cells/ml=10,000*mean number of cells per large square*trypan blue dilution factor*medium dilution factor.

293T, Plat-E, U373 and C17.2 cells

Cells were splitted at 80% confluence by washing 1x with PBS (w/o Ca²⁺, Mg²⁺) and detachment with 50 µl/cm² Trypsin for approx. 2 min at 37°C. Trypsin reaction was stopped with 1-3 ml medium, cells collected and centrifuged for 3 min at 1,000 rpm. The pellet was resuspended in 1-3 ml medium and the cells counted and subsequently plated (approx. 30,000 cells/cm²). The following complete media were used: 293T, Plat-E, U373 (DMEM FCS), C17.2 (DMEM FCS/HS)

CGR8 and D3WT cells

The ES cell lines CGR8 and D3WT cells depend on gelatine coating and feeder layers (γ-irradiated mouse fibroblast culture, obtained from Dr. Saric Dept. Neurophysiology, University of Cologne), respectively. The cells were splitted before reaching 80% confluence (approx. every 2nd day) by washing 1x with PBS (w/o Ca²⁺, Mg²⁺) and detached with 50 µl/cm² Trypsin for approx. 2 min at 37°C. Trypsin reaction was stopped with 1-3 ml medium, cells collected and centrifuged for 3 min at 1000 rpm (except for the EBs, which were centrifuged for 3 min at 500 rpm). The pellet was resuspended in 1-3 ml medium, the cells counted and subsequently plated (approx. 18,000 cells/cm²). The maintenance of pluripotent state needs to be checked regularly for these cells, e.g. by morphological analysis and staining for alkaline phosphatase – an enzyme elevated in stem cells (Figure 10).

Derivation and culture of D3WT_N2Euro#4

The radial glia-like NSCs were derived after a modified protocol from Conti *et al.*⁹³: the D3WT cells (see above) were seeded on bacteriological grade plates (approx. 2,000/cm²) in DMEM FCS* (w/o LIF) for 4 d and subsequently passaged in N2/B27 medium for additional 10-14 d. The developing neurosphere-like EBs were plated on gelatine coated plates and attached on the surface for 1 d. Afterwards, the medium was changed to D3N2Euro, which induced proliferation of FGF- and EGF-responding cells. The proliferating, adherent cell subgroup was further passaged using Accutase instead of Trypsin for detachment and cultured additional 10 d until the stable cell line develops. For further passaging D3N2Euro medium, Accutase and gelatine coated plates were essential to maintain NSC state. The neuronal differentiation was induced by plating 50,000 cells/cm² on POLA coating in the D3N2Euro media without EGF for 3 d. The cells were further cultured for 7 d in N2/B27 media. The glial differentiation was induced by plating 50,000 cells/cm² on POLA coating and culture in D3N2Euro FCS media for 7 d.

2.4.4 Transfection protocols

Cell transfection was used for short-term gene expression analysis and functionality tests of the cloned plasmids in 24-well plates (with glass slides and 0.2% gelatine coating for IHC) or black 96-well plates for BLI. The day before transfection, cells were seeded at 25,000/cm² (NSCs) and 17,500/cm² (tumor cells) in the complete media. 24 h later, 0.25 µg/cm² plasmid DNA was diluted in 50 µl/cm² OptiMem and mixed with 0.5 µl/cm² Plus Reagent. After initial incubation at RT for 5 min, 1 µl/cm² Lipofectamine LTX was added, mixed and incubated for 30 min to allow lipo-DNA complex formation. Afterwards, cell media was exchanged by 50 µl/cm² lipo complex and incubated for 4 h at 37°C. After lipofection, media was refreshed with complete growth media and the cells were further cultured for up to 48 h prior testing of transgene expression. In case of experiments with U373 cells, 24 h after transfection, cells were additionally stimulated by adding 1.5-5.0 mM valproic acid or 10-50 mM ethanol to the media to enhance GFAP expression^{104,105}.

2.4.5 Transduction protocols

Ecotrop transduction

For retroviral packaging, Plat-E cells were plated 24 h prior to transfection at 1x10⁵/cm² in 0.25 ml/cm² DMEM FCS (w/o antibiotics). The transfection was achieved by mixing 0.2 µg/cm² plasmid DNA diluted in 20 µl/cm² OptiMem plus 0.2 µl/cm² Lipofectamine Plus Reagent and incubating for 5 min at RT. Afterwards, 0.25 µl/cm² Lipofectamine were added and incubated for 30 min to allow DNA-lipo complex formation. Before adding the transfection mix, cells were washed 3x with OptiMem and supplement with 0.1 ml/cm² OptiMem containing Chloroquine (final conc.: 25 µM). Finally, the DNA mixture was added dropwise to the cells, mixed gently by shaking the plate and incubated at 37°C overnight. 24 h post transfection, the medium was exchanged. The virus collection started 48 hours post transfection, by centrifugation of the supernatant at 1,500 rpm/4°C for 5 min to pellet cell debris. The virus was stored long-term at -80°C. For retroviral infection of proliferating target cells (not confluent culture in 24-well plate), medium was exchanged by 200 µl OptiMem containing 7.5 ng/ml Polybrene and 200 µl virus-supernatant. After 24 h of incubation at 37°C, media was exchanged. At 48 hours post infection selection with antibiotics or cell sorting via FACS started.

Amphitrop transduction

The amphitrop transduction is based on 3 steps: 1) production of pseudoviral particles in a packaging cell line (e.g. 293T) by co-transfection of the expression plasmid and packaging vectors, 2) Collection of pseudoviral particles from producer cells, and 3) transduction of the target cells with pseudoviral particles, which will drive transgene integration into the host genome by reverse transcription. The 3rd generation lentivector expression system is based on the expression vector, which contains the

genetic elements required for packaging, transduction, stable integration of the viral expression construct into genomic DNA, and expression of the reporter, but is lacking genes coding for viral replication. The structural replication and integration proteins are provided by the packaging plasmids pPACKH1-GAG, pPACKH1-REV and pVSV-G. The resulting pseudoviral particles are limited by infection and stable transgene transfer into the target cells – the production of new infectious virus particles is blocked. For lentiviral packaging und Biosafety Level 2 criteria, 293T cells were plated 24 h prior to transfection at 8.8×10^5 cells/cm² in 0.2 ml/cm² DMEM FCS (w/o antibiotics). The transfection mix consisted of 1) 2.25 µg pPACKH1 packaging plasmid mix and 1 µg target vector in 100 µl Optimem, 2) mixed with 4 µl Lipofectamine Plus Reagent and incubated for 5 min at RT, and 3) the addition of 8 µl Lipofectamine LTX, mix and incubation for 30 min at RT to allow DNA-lipo complex formation. Before adding the transfection mix, cells were washed 3x with Optimem. Transfection mix plus 4.0 ml Optimem was added and incubated 37°C for 12-15 h. The day after medium was changed and cells further incubated at 32°C and 5% CO₂ to facilitate transfection process. 48 h post transfection, the first virus supernatant was collected and stored overnight at 4°C. This procedure was repeated 24 h later and both virus samples were centrifuged at 1,250 rpm for 10 min and aliquoted for long-term storage at -80°C. For lentiviral infection, target cells were prepared the day before by plating on 24-well plates at 4,000 cells/cm² and incubation overnight. The virus mix contained 8 µg/ml polybrene in 200 µl medium and 200 µl virus stock for each well^{IV}. The expression of reporter genes was monitored in the target cells the next 2-3 days and medium changed or cells passaged if necessary. If the cells exhibited transgene expression during at least 3 passages, cell culture was transferred to Biosafety Level 1 area and selection process (via antibiotics or FACS) started.

2.4.6 Cell labeling with contrast agents

The cell labeling procedures were adapted based on previously described protocols. In general, transfection methods are commonly to introduce foreign DNA (see 2.4.4). Moreover, most of the techniques are also able to facilitate uptake of MRI contrast agents dependent on the particle size and polarity. Several methods were compared with regard to uptake and influence on cell viability/survival using the commercially available paramagnetic contrast agent Dotarem®, which shares the chemical structure of the Gd(III) chelate with Gd-DO3A-GAD. The tested methods are 1) Pinocytosis (Pino): a process of spontaneous uptake of contrast agent supplemented to the cell culture media by the unspecific and random pinocytosis/endocytosis, 2) calcium phosphate precipitation (CaP): contrast agent binds to calcium phosphate which crystallizes in a mixture of calcium chloride and sodium phosphate and is taken up by endocytosis⁹⁸, 3) lipofection (Lipo): the contrast agent is coated

^{IV} For transduction of (neural) stem cells supplementation with growth factors is recommend.

by a positively charged phospholipid bilayer which induces fusion with the cell membrane¹⁰⁶, and 4) electroporation (EP), which induces the reversible formation of small pores in the cell membrane upon an electrical discharge¹⁰⁷. Cells were prepared as follows: undifferentiated CGR8 cells were detached with 0.05% trypsin/0.02% EDTA (PAA), centrifuged at 250 \times g for 3 min and counted. Differentiated CGR8 cells were detached and dissociated with accutase (PAA) by careful titration, centrifuged at 250 \times g for 3 min and counted. Pinocytosis was achieved by incubating the cells for 2 h in the presence of 50 mM Dotarem[®]. For lipofection a custom-made transfection agent similar to lipofectamine¹⁰⁸ was used in a lipo:contrast agent ratio of 1:2, preincubated for 30 min, followed by 2 h incubation with the cells in complete medium. The CaP transfection mixture was prepared as described by¹⁰⁹. Briefly, 2 \times BES-buffered saline (BBS), 0.25 M CaCl₂ and 50 mM Gd-DOTA were mixed in a ratio of 2:1 and treated like the lipofection samples. For electroporation 50 mM Gd-DOTA were mixed with ice-cold Hanks Balanced Salt Solution (HBSS) and directly electroporated using the GenePulser with a 100 V square pulse for 20 s. After EP, cells were placed on ice for 5 min. Independent of the labeling method, cells were finally washed twice with PBS to remove excessive contrast agent and counted by the trypan blue exclusion assay to determine viability and survival rate (see 2.4.8). The electroporation protocol was applied to undifferentiated and differentiated cells with 10 mM Gd-DO3A-GAD. The cells were subsequently plated for 6 h and collected by centrifugation at 250 \times g for 3 min. Labeled cells were washed and counted as described above. Cell pellets were directly used for cell implantations by adjusting the cell number to 1.875 \times 10⁵ cells/ μ l in HBSS or either fixed with PFA for 15 min at RT for MRI phantoms.

2.4.7 Phantom preparation for MRI

For MRI on cells and lysates a MRI compatible setup was used, which allowed positioning of the probes on the MRI animal holder without introducing additional susceptibility artefacts and permitted the long-term storage of the imaging probes. Phantoms for MRI experiments at 4.7 T consisted of plastic PCR tubes containing a mixture of cells/tissue lysates and 0.5% low melting agarose covered and embedded in 1% agarose (Figure 11A, B).

The measurements at 1.0 and 7.0 T (at University of Torino) were conducted on cell pellets in glass capillaries embedded in a 10 mm glass tube filled with 1% agarose. The agarose phantoms were cooled down to room temperature for MRI experiments or cooled down to 4°C for long-term storage. For the quantitative comparison of T_1 scans (see section 3.2), two specific phantoms were used: a T_1 reference phantom (Figure 11) and a PCR tube phantom with distinct concentrations of Gd-DTPA (Magnevist[®], Bayer) ranging from 0.5-25 mM.

The reference phantom was prepared according to previous reports^{110,111}: it consists of 9 different nickel chloride (NiCl₂) concentrations ranging from 0.2 to 1.9 mM in aqua dest, mixed with deuterium

oxide (D₂O) and agarose in 15 ml falcon tubes (Table 15, Figure 11C). Compared to Gd(III), Ni(II) doped agarose is much less temperature and magnetic field strength dependent and exhibits stable T_1 relaxation times under various experimental conditions.

Table 15: Composition of the reference phantom tubes.

Sample	NiCl ₂ (mM)	NiCl ₂ (ml)	H ₂ O (ml)	D ₂ O (ml)	Agarose (g)
1	1.88	8.30	1.70	0.00	0.06
2	0.12	0.55	9.45	0.00	0.02
3	0.24	1.05	8.45	0.50	0.08
4	0.50	2.20	6.30	1.50	0.13
5	0.27	1.20	7.30	1.50	0.11
6	0.91	4.00	5.00	1.00	0.22
7	0.50	2.20	5.80	2.00	0.25
8	1.61	7.10	0.40	2.50	0.20
9	0.58	2.55	5.00	2.50	0.15

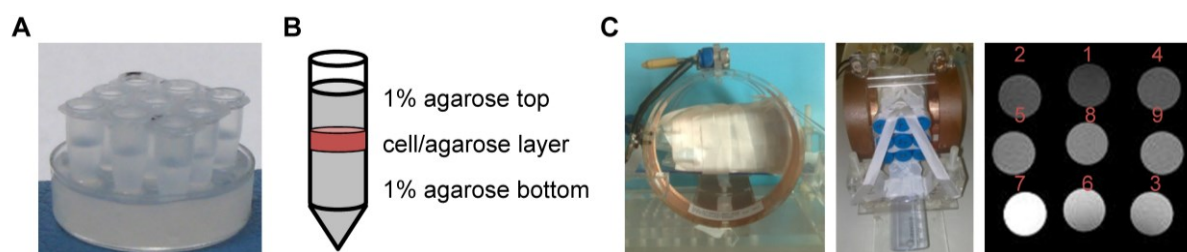


Figure 11: MRI phantom composition: A) PCR tube phantom for lysate and cell analysis. B) Composition of the PCR tube phantom containing three layers of agarose. C) Reference phantom placed in helmholtz coil setup for receive/transmit. Pictures illustrate views from the left, top, and a representative RAREVTR scan image with the sample assembly.

2.4.8 Characterization of labeled cells and transduced cells

Cell viability and survival rate measured with the trypan blue exclusion assay

Based on the standard method for cell counting with the trypan blue exclusion assay for cell passaging (see 0), this test was adapted to count the number of viable (transparent) and dead (blue) cells per treatment. The resulting number of viable cells in percent gives a “snapshot” information on the treatment impact ($viability = viable\ cells / total\ cell\ number \times 100\%$). In addition for cell labeling experiments, the number of viable cells was compared to an untreated control group (n=3). This measure is capable of reflecting the number of cells, which died because of the labeling – a very important measure reflecting the contrast agent toxicity: $survival\ rate = viable\ cells_{treated} / viable\ cells_{untreated} \times 100\%$).

PrestoBlue live-cell viability assay

The PrestoBlue assay solves the challenge to determine cell viability quantitatively in short time without cell impairment. This assay was used to identify changes in cell viability between transduced and wildtype cells. The PrestoBlue reagent is a resazurin-based solution, which is blue and nonfluo-

rescent, but subsequently turns red and fluorescent (emission max. 586 nm) after cell-endogenous reduction processes take place. The fluorescent measurement is quantitative due to the proportional relation between conversion and number of metabolically active cells. 24 h before PrestoBlue test, 5,000 cells/well were plated in 100 μ l (96 well). The next day, medium was removed, centrifuged at 1,000 rpm for 3 min and later used for background correction. Finally, 10 μ l and 90 μ l complete media was added to each well and incubated for 2 h at 37°C. The fluorescence was measured using the plate reader (adjustments: duration: 0.5 s, lamp Energy: 14,000, excitation: 530 nm; emission: 600 nm). If luciferase expressing cells were used, bioluminescence could be measured in the same well after washing 2x with PBS, adding new media and 1 mM 2 μ g/ μ l D-Luciferin (adjustments: shake for 10 s, acquisition for 2 s).

Cell proliferation

The determination of cell proliferation was achieved by at least 5 subsequent measurements. On the first day, 5x 60 mm dishes of each cell line/treatment were prepared in duplicate (approx. 1×10^5 cells) and counted for the following 5 days. The cell density at day 0 and on the following days was used to determine the doubling time – h/generation: $\text{doubling time} = (\log(\text{cell number day } x) - \log(\text{cell number day } 0)) / \log 2) / \text{hours}_{\text{day } 0 \text{ to } x}$.

2.5 Histology

For histological analysis, mice were perfused with 0.1 M PBS and 4% PFA, the brains were removed and subsequently frozen in -40°C cold methanol. Longterm stored brains (-80°C) were sliced 10-20 μ m thin using a cryostat and directly used for histology. Conventional histological stainings (e.g. Nissl, Hoechst, etc.) and the alkaline phosphatase detection assay for ESCs were performed according to established protocols⁸⁹ and manufacturer's protocols. Prior to histology, cells were fixed with 4% PFA for 15 min at RT and washed 2x with 0.1 M PBS. For immunohistochemistry (IHC) and immunocytochemistry (ICC) analysis, a standard protocol consisting of 1) permeabilization with 0.025% (ICC) or 0.25 % (IHC) Triton-X-100 in TBS for 10 min, 2) unspecific antigen blocking by 5% BSA in TBS for 60 min, 3) primary antibody binding in 0.8% BSA for 2 h, 4) coupling of the primary specific secondary antibody (Dylight 488 or 549, made in goat, dilution 1:1000, Pierce) in 0.8% for 60 min and counterstaining of the cell nuclei with Hoechst dye 33342 for 10 min. In between the protocol steps and after the last step, cells were carefully washed at least 2x with TBS. The glass slides or object slides were mounted with Aquamount and long-term stored at 4°C in the dark.

Table 16: List of antibodies used for IHC and ICC

Antigen	Host	Dilution	Product-nr.	Supplier
Alpha tubulin	Mouse	1:500	CP06	Calbiochem
betalll tubulin	Mouse	1:300	T8660	Sigma-Aldrich
betalll tubulin	Rabbit	1:200	PRB-435P	Covance

DCX	Rabbit	1:500	4604	CellSignaling
DyLight488 anti-mouse	Goat	1:1000	35502	Pierce
DyLight488 anti-rabbit	Goat	1:1000	35552	Pierce
DyLight549 anti-mouse	Goat	1:1000	35507	Pierce
DyLight549 anti-rabbit	Goat	1:1000	35557	Pierce
GABA	Rabbit	1:1000	A2052	Sigma-Aldrich
GAD65/67	Rabbit	1:200	AB1511	Abcam
GFAP	Mouse	1:750	G3893	Sigma-Aldrich
GFAP	Rabbit	1:200	Z0334	Dako
Living Colors DsRed	Rabbit	1:500	632496	Clontech
Nestin	Rabbit	1:500	Ab5968	Abcam
Nestin	Mouse	1:500	MAB353	Millipore
Oct4	Rabbit	1:200	SC8066	SantaCruz

2.6 Animal experimental protocol

2.6.1 Animal handling and anesthesia

All animal experiments were conducted according to the guidelines laid out in the German Animal Welfare Act, in accordance with the European Communities Council Directive 86/609/EEC, and were approved by the local authorities (Landesamt für Natur, Umwelt und Verbraucherschutz North Rhine-Westphalia, reference number 8.87-51.04.20.09.362 and A123). Mice and rats were purchased from Janvier (Saint Berthevin Cedex, France). Animals were housed in individually ventilated cages at 25°C with regulated day-night cycle and handled in relation to the guidelines of the German council for laboratory animal use (GF-SOLAS, <http://www.gv-solas.de/index.html>). The anesthesia protocols were adapted from previously described versions^{37,112}.

For MR measurements, mice were fixed with a tooth bar and ear bars in a custom-made animal holder (medres, Cologne, Germany) for stable animal fixation. The holder was coupled to a warming pad system for heating. The respiration rate was monitored with a pressure sensitive pad under the thorax using DASylab (Measurement Computing, Norton, USA) software. This setup allowed imaging under physiological conditions for several hours. For BLI measurements animals were not fixed (because of the lower image resolution not necessary), but also warmed to 37°C. In both setups, inhalation anesthesia was conducted by nose caps with constant 2% Isoflurane supply at approx. 1 bar in O₂:N₂O (30:70%). Nitrous oxide is used in this carrier gas-mixture, because of its anesthetic and analgetic effect. Isoflurane is one of the most common inhalation anesthetics, exhibiting an analgetic effect, reducing muscle tonus and inducing vasodilation. For injection anesthesia, Ketamine/Xylazine anesthesia was induced by intraperitoneal (ip) injection of 100 mg/kg ketamine and 10 mg/kg Xylazine, resulting in a sleeping time of approx. 45 min. Ketamine is a NMDA-receptor antagonist and induces analgesia, anesthesia, hallucinations, elevated blood pressure and bronchodilation. It is

combined with the $\alpha 2$ agonist Xylazine for muscle relaxation. Furthermore, Pentobarbital anesthesia was applied by injecting 45 mg/kg ip, which resulted in a sleeping time of approx. 45 min. As a barbiturate, Pentobarbital induces sedation and anesthesia.

2.6.2 Intracerebral transplantation

Cell preparation

For intracerebral transplantations, cells are cultured for at least 2 passages in advance to allow balanced gene expression and high cell viability. On the day of surgery, cells are detached and counted (see cell specific protocols, 0). The cell amount is adjusted carefully to result in a total injection volume of 2 μ l (e.g. 150,000 cells/ μ l for the injection of 300,000 cells) in HBSS buffer. Cells have to be kept on ice until transplantation to ensure high viability.

Surgery

Mice were anaesthetized with Isoflurane in O₂:N₂O (30:70%) and fixed in the stereotactic frame, equipped with a warming pad and temperature feedback control for efficient control of the physiological state. For analgesia, Carprofen was injected subcutaneously (sc) using a 2 ml syringe with a 30g needle (4 mg/kg sc). The skull was exposed by a small incision and hole(s) were drilled at the following coordinates relative to bregma: AP+0.5; L \pm 2.0; DV-2.5 using a stereotactical instrument. The homogeneous cell suspension was injected into the brain through a Hamilton syringe using a micropump system with flow rates of 1,500 nl/min (withdraw) and 500 nl/min (injection). Before removing the syringe, it was left in place for 5 min to allow the cells to diffuse locally. The wound was sutured and the animal woke up under controlled conditions in an incubation chamber at 30°C.

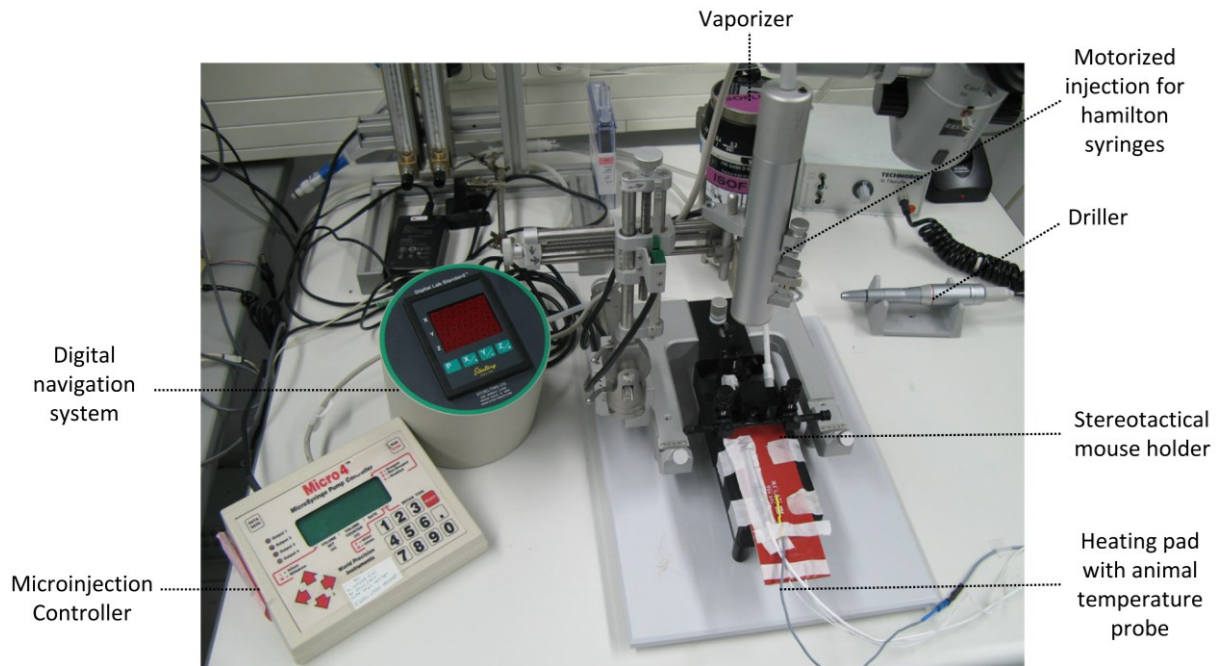


Figure 12: The technical setup for stereotactical injections included a driller, the stereotactical mouse holder equipped with a motorized injection for Hamilton syringes, a microinjection controller and digital navigation system. Animals were kept under Isoflurane anesthesia by using a vaporizer and O_2/N_2O 30:70% at physiological conditions by heating with warming pad controlled by a temperature probe.

2.7 Experimental imaging setup

2.7.1 Evaluation of MRI sequences for determining T_1 relaxation

A precise determination of T_1 relaxation is a prerequisite for experiments with a paramagnetic contrast agent, which is designed for T_1 contrast weighted MRI. Spin echo with inversion recovery (MSME_IR) serves as the NMR reference, hampered for in vivo imaging by the long acquisition time. Therefore, a variety of different MRI sequences comprising different physical principles for determining T_1 were tested in order to select a short and stable method, which fits to in vitro and in vivo conditions: 1) variation of the repetition time with fixed echo time (TE) and flip angle (FA), 2) variation of inversion time (TI) with fixed TE, TR and FA. The sequences were either gradient echo (FLASH) or spin echo based (MSME, RAREVTR). The signal intensity per voxel was plotted against the variable time constant or flip angle and fitted with the Bloch equations (see 1.2) per voxel using an in-house software (see 2.7.4).

These measurements were conducted with the Nickel standard phantom (Table 17), the Gd-DTPA phantom (Table 18) and applied for in vivo tests on mice and rats (Table 19).

Table 17: MRI parameter for optimizing T_1 relaxometry in vitro with the Nickel standard phantom

Nickel standard phantom					
	FLASH_TR	FLASH_IR	MSME_TR	MSME_IR	RAREVTR
TR/TI (ms)	14x (50 – 10000)	15x (20 – 5000)	16x (65 – 10000)	13x (75 – 5000)	12x (100 – 5000)
TE (ms)	4	4	13.5	13.5	12
FA	30°	90°	90°	90°	90°
FOV (mm)	70x70	70x70	70x70	70x70	70x70
Matrix	128x128	128x128	128x128	128x128	128x128
Resolution (mm)	0.547x0.547	0.547x0.547	0.547x0.547	0.547x0.547	0.547x0.547
Slice (mm)	2	2	2	2	2
Averages	4	4	4	4	4
Acquisition time (h)	9	13	9	11	1

Table 18: MRI parameter for optimizing T_1 relaxometry in vitro with the Gd-DTPA phantom

Gd-DTPA phantom					
	FLASH TR	FLASH IR	MSME TR	MSME IR	RAREVTR
TR/TI (ms)	14x 12.5 - 5000	19x (25 – 5000)	12x (20-10000)	19x (30-5000)	12x (30-10000)
TE (ms)	4	4	13.5	13.5	12
FA	30	90	90	90	90
FOV (mm)	30x30	30x30	30x30	30x30	30x30
Matrix	128x128	128x128	128x128	128x128	128x128
Resolution (mm)	0.234x0.234	0.234x0.234	0.234x0.234	0.234x0.234	0.234x0.234
Slice (mm)	2	2	2	2	2
Averages	1	1	1	1	1
Acquisition (total)	0.5	5	3	4.5	0.75

Table 19: RAREVTR parameter for in vivo validation

In vivo tests			
	RAREVTR (rat)	RAREVTR (mouse)	RAREVTR (mouse) 11.7 T
TR/TI (ms)	12x (250-5000)	12x (30-5000)	12x (200-9000)
TE (ms)	12	12	12
FA	90	90	90
FOV (mm)	30x30	30x30	30x30
Matrix	128x128	128x128	128x128
Resolution (mm)	0.234x0.234	0.234x0.234	0.234x0.234
Slice (mm)	2	2	2
Averages	2	2	1
Acquisition (total)	0.5	0.75	0.5

2.7.3 In vitro and in vivo MRI protocols

MRI phantom PCR tubes measured at 4.7 T

MRI experiments with tissue lysates and for the optimization of cell labeling were conducted on a Biospec 4.7 T (Bruker BioSpin, Ettlingen, Germany) with a transmit Helmholtz coil (120 mm diameter) and a receive surface coil (28 mm diameter) for receive. T_1 maps were acquired with a RAREVTR sequence using the following parameters: 12 variable TR=116.640, 258.513, 415.220, 590.230, 788.388, 1,016.768, 1,286.274, 1,615.045, 2,036.712, 2,625.391, 3,608.035, 7,500.000 ms, effective TE=12.0 ms, Rare factor 2, field of view (FOV)=30.0×30.0 mm, slice thickness 2.0 mm, matrix=128×128, resolution=0.234×0.234 mm, number of averages=2, with a total acquisition time (TA) of 46 min.

MRI phantom measured at 1.0 and 7.1 T

MRI experiments on cell pellets were acquired on an Avance300 spectrometer (Bruker) operating at 7.1 T equipped with a microimaging probe using a standard T_1 -weighted MSME sequence (TR=250 ms, TE=3.3 ms, NEX=6, FOV=0.115×0.115 cm², 1 slice, slice thickness=1 mm) and on an Aspect M2 system (Aspect Imaging, Shoam, Israel) operating at 1.0 T equipped with a horizontal bore MRI magnet using a standard T_1 -weighted multi-slice spin-echo sequence (TR=250 ms, TE=7.0 ms, NEX=30, FOV=0.17×0.17 cm², 1 slice, slice thickness=1.5 mm). T_1 values were measured using a saturation recovery spin-echo sequence (at 7 T: TE=2.6 ms, 16 variable TR ranging from 40 to 6,000 ms, NEX=1, FOV=0.115×0.115 cm², 1 slice, slice thickness=1mm; at 1 T: TE=7.0 ms, 12 variable TR ranging from 50 to 4,000 ms, NEX=1, FOV=0.17×0.17 cm², 1 slice, slice thickness=2 mm). For relaxometric determination of intracellular Gd(III)-content, cell pellets were treated as described elsewhere¹¹³.

Determination of R_1 field dependence

The proton R_1 NMRD profiles of tissue lysates were measured at 25°C on a fast field-cycling Stelar relaxometer (Stelar, Mede Pavia, Italy) over a continuum of magnetic field strengths from 0.00024 to 0.47 T (corresponding to 0.01–20 MHz proton Larmor frequencies). The relaxometer operates under computer control with an absolute uncertainty in R_1 of ±1%. Additional data points in the range of 20–70 MHz were obtained on a Stelar Spinmaster relaxometer tunable to the different frequencies. The temperature was controlled with a Stelar VTC-91 air-flow heater equipped with a copper constantan thermocouple to 25°C±0.1.

In vivo MRI at 7.0 T

The in vivo MRI data was acquired on a Biospec 7.0 T (Bruker) using a 8 cm diameter transmit Helmholtz coil and a 16 mm diameter receive surface coil for detection under Isoflurane (2%) anesthesia (O₂:N₂O, 30:70 %) and lasted approximately 35 min. For a general overview and the coregistration, a T_2 -weighted RARE sequence was used (TR=6,500 ms, TE=13.0 ms, FOV=14.0×14.0 mm², 30 slices,

slice thickness=0.5 mm, 128×128 matrix, i.e. a resolution of 109×109×500 μm^3). The T_1 maps were acquired with a RAREVTR sequence (12 variable TR 189.708, 331.527, 488.167, 663.094, 861.146, 1,089.384, 1,358.693, 1,687.171, 2,108.355, 2,696.085, 3,676.028, 7,500.000 ms, effective TE=12.0 ms, Rare factor=2, FOV=20.0×20.0 mm^2 , 6 slices, slice thickness=1.0 mm, 128×128 matrix, i.e. a resolution of 156×156×1000 μm^3)¹¹⁴.

2.7.4 MRI postprocessing

T_1 maps were calculated on a voxel basis with monoexponential fits using a custom-made program developed in IDL, which includes an initial signal-to-noise (SNR) cut-off for each voxel at SNR < 5¹¹⁵.

For RAREVTR measurements, the MRI signal $S(\text{TR})$ was fitted with the following function:

$S(\text{TR}) = S_0 \cdot (1 - e^{-\frac{\text{TR}}{T_1}})$ or $S(\text{TI}) = S_0 \cdot (1 - 2 \cdot e^{-\frac{\text{TI}}{T_1}})$ with equilibrium signal S_0 , relaxation time T_1 , repetition time TR and inversion time TI.

MR images were visualized and processed with ImageJ (Version 1.42q; National Institutes of Health). Region of interest (ROI) analysis based on the quantitative maps was used to determine T_1 values for phantom tubes or cell graft. In case of MRI phantoms, circular ROIs with identical diameter were drawn manually. For the in vivo measurements, two ROIs were drawn manually along the grafting canal in one animal and applied to all scans, yielding T_1 values for the phantom samples and the cell grafts, respectively.

Changes in relaxation rate ΔR_1 induced by the contrast agent were calculated by:

$$\Delta R_1 = (1/T_{1(\text{treated sample})}) - (1/T_{1(\text{untreated sample})})$$

This calculation minimizes the impact of fluctuating background T_1 values for each sample and allows comparison of T_1 maps from different scans. The relaxivity r_1 was determined from T_1 maps of dilution series of NiCl_2 and Gd-DTPA in different concentrations (c) as the slope of the linear fits according to: $R_1 = R_0 + r_1 \cdot c$. Further processing of the in vivo MRI data was done by converting the raw data into 32-bit NIFTI format (Neuroimaging Informatics Technology Initiative; <http://nifti.nimh.nih.gov>) and scaling up the voxel size by a factor of 10. For brain extraction and affine coregistration with 12 degrees of freedom, FSL tools were used (FMRIB Software Library; <http://www.fmrib.ox.ac.uk/fsl>). The data was processed according to a 4-step protocol: 1) RARE scans of all animals were registered and averaged to yield a brain template, 2) the RAREVTR scans of every time point were coregistered to the template brain, 3) the resulting transformation was applied to the T_1 maps accordingly and 4) for visualization, brain maps were masked manually to exclude non-brain tissue¹¹⁴.

2.7.6 Optical imaging

Technical setup

BLI was conducted using the Photon IMAGER™ – a BLI camera equipped with an f/1.4 numerical aperture lens for light collection and a 3rd generation (Gallium Arsenide PhotoCathode) dual multichannel plate intensifier tube coupled through an optical fiber to a charge coupled-device (CCD) chip for light detection. The object is placed on a stage, which is heated up to 37°C and can be adjusted in height revealing a FOV ranging from 18x24 cm to 6x8 cm. The camera equipment is caged in a light proof hood (low level of 30 photons/s background radiation). The detection of photons is achieved by several steps, involving the collection of photons by the lens, the amplification by the dual channel plate intensifier by a factor of 10⁵ and detection by the CCD chip. Optical resolution is limited by the separation of 2 spots in 100 µm distance (stage top position) and 300 µm (stage base position). Calculation of the photon flux (ph/s/cm²/sr) is achieved by the software-automated calculations, which include the conversion of photodetector counts to photons per s and cm², the correction for light source placement and the noise introduced by cosmic radiation. For selection of emission/excitation wavelengths, a set of six long-pass filters (515-800 nm) and continuous wavelength excitation filter (5 nm accuracy, 400-740 nm range). The Photon IMAGER™ is equipped with gas and vaporizer for inhalation anesthesia and a PC for image acquisition (Photon Imager software Version 2.7.5.1) and evaluation (M3 Vision software Version 1.5 rev.1076). In addition to the Biospace system, an IVIS Spectrum imager was used in the collaboration with Prof. Löwik (LUMC Leiden, The Netherlands). The IVIS camera contains the same major components, but offers additional filters for excitation (18 filter 30 nm bandwidth) and emission filter (20 filter 20 nm bandwidth), which allow acquisition and separation of light spectra and finally spectral unmixing e.g. of luciferases emitting light at different wavelengths and the reduction of autofluorescence.

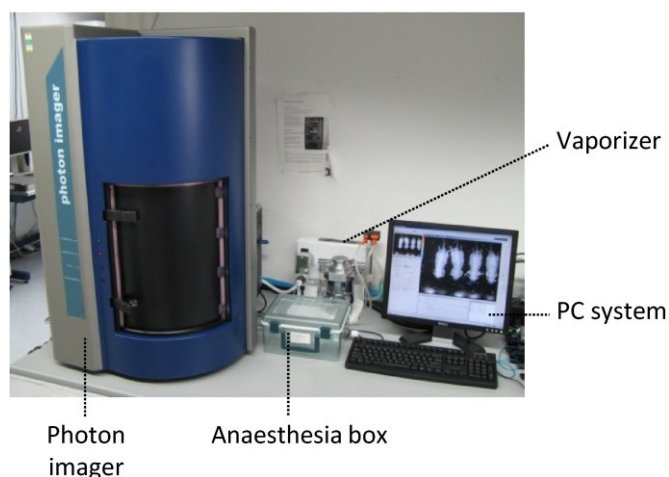


Figure 13: The experimental setup for bioluminescence imaging includes the Photon Imager with a PC for acquisition and analysis and equipment for inhalation anesthesia (anesthesia box and vaporizer).

Acquisition parameter

The video/photo was acquired by adjusting the illumination to 10-20% and setting the aperture to 22.6. In the BL mode, aperture was adjusted to 1.4, which results in an open diaphragm and allows more photons to hit the photomultiplier plate.

In vitro BLI was conducted on cells seeded in 96 black well plates (to reduce light scattering and reflection) by adding the appropriate substrate directly prior to measurement. The plate was carefully moved to disperse substrate equally and placed centrally on the stage in top position. The stage was heated to 37°C to allow comparison to in vivo conditions. BLI signals were recorded for 1 min.

For in vivo BLI, stage height was adjusted to fit the FOV covering all animals (1-4) and fixed between same experiments. The standard imaging protocol included i.p. injection of 150 mg/kg D-Luciferin in the pre-anaesthetized animal and subsequent measurement for 15-60 min.

Optical imaging postprocessing

BLI raw data was analyzed using the M3Vision software. Time profiles were extracted with 5 s and 60 s time frame for each ROI (with constant size between different measurements) with the fixed unit $\text{ph/s/cm}^2/\text{sr}$. Background ROIs were only necessary for the transgenic DCX-Luc mice (on the shaved back, ROI size equal to brain ROI) to subtract unspecific signal correlating with substrate injection dose and for hRluc transgenic cells vs. control cells to normalize for the coelenterazine auto-oxidation and the resulting unspecific photon emission. For in vitro data, no time profiles were acquired, but the ROI means for 1 min acquisition were used to calculate mean and standard deviation for e.g. a particular cell line (at least in triplicate). From cell dilution series (in triplicate) the photon flux per (photons/cell) were calculated by dividing the ROI $\text{ph/s/cm}^2/\text{sr}$ by the cell number plated in each well. The in vivo time profiles were exported to Excel (Version 2010, Microsoft Corporation, Redmond, USA) and evaluated with user-written macros according to Keyaerts *et al.*³⁷: the 95th percentile (5s time frame) referring to maximum photon emission (“PE_{max}”) and the “time-to-peak” (60 s time frame) referring to the time needed after substrate injection to reach maximum photon emission. Time curves were preprocessed by correction for the actual acquisition start by addition of the time between substrate injection and acquisition start, to correct for interindividual differences. The 95th percentile of N ordered values (e.g. 360 time frames for 30 min acquisition) is obtained by calculating the rank n : $n = 95/100 \cdot N + 0.5$. The result is rounded to the nearest integer and the photon emission corresponding to n represents the PE_{max}. For calculation of time-to-peak the maximum photon emission in the 60 s time frame curves was determined. The signal-to-noise ratio (SNR) on optical data was calculated by dividing mean photon flux ($\text{ph/s/cm}^2/\text{sr}$) by the standard deviation of the noise. For accurate calculation of the noise, the mean of 3 randomly chosen ROIs outside the mouse was calculated.

2.7.7 Microscopy

Bright field images were acquired using the Zeiss Axiovert, confocal fluorescence images with the Leica TCS SP2 microscope equipped with a supplementary CCD camera and the Keyence BZ-9000 microscope. Microscopic images were acquired by keeping brightness/contrast and illumination constant for each project to allow a qualitative comparison. Phase contrast images were acquired at 10 and 20x magnification; fluorescence images at 20, 40 and 63x magnification (ocular 10x magnification). IHC and IHH images were preprocessed using the manufacturer microscopic software and finally modified with the ImageJ software by adjusting brightness/contrast accordingly for each experimental setup. Quantification of cell differentiation was achieved by counting GABA, GAD, beta III-tubulin, DCX or GFAP-positive cells based on the specific immunostaining. This cell number was divided by the total cell number represented by the counting the Hoechst-stained cell nuclei. This counting procedure was done for 5 randomly chosen fields of view at 40x magnification.

The relative ICC signal intensity was calculated by measuring the image intensity with ImageJ and dividing this mean value by the number of cells on the image. At least 3 separate images were analyzed for each condition. The brightness was adjusted on the microscope software for every acquisition equally. Acquisitions with the Leica TCS SP2 were adjusted to GFAP 0-45,000 a.u.; copGFP 0-25,000 a.u. and Hoechst 0-25,000 a.u.; for the Keyence BZ-9000, excitation for copGFP and Hoechst were set to 1 s and 1/150 s, respectively.

2.8 Statistics

All data are represented as mean \pm SD. Unpaired t test was used to compare means of 2 groups for in vitro experiments (GraphPad QuickCalcs, GraphPad Software, La Jolla, USA).

In vivo BLI data was analyzed using a repeated measures ANOVA for each individual test regime (concentration, injection route, anesthesia, time of injection). Post hoc comparisons were corrected for multiple comparisons using Sidak correction (SPSS version 20, IBM SPSS statistics, Ehningen, Germany). If not specified, a p-value \leq 0.05 was considered to be significant and highlighted by *, in addition a p \leq 0.005 was marked by **.

3. IMAGING GABAERGIC NEURONS BY MRI

3.1 Project aim and experimental setup

MRI-based tracking of contrast agent labeled stem cells grafted in the rodent brain has become the noninvasive imaging method of choice because of the high spatial resolution and the possibility for repeated, noninvasive measurements. Nevertheless, this method is lacking information about stem cell fate and viability. Furthermore, the unambiguous detection of neuronal subtypes - which potentially develop out of a stem cell graft, cannot be imaged selectively with MRI.

The aim of this project was to design and evaluate a novel molecular probe (in cooperation with the group of Prof. Silvio Aime, University of Torino, Italy), which allows the detection of neurons with MRI. As a potential target, we selected the glutamic acid decarboxylase (GAD) enzyme, which exists in two isoforms encoded by two separate genes: GAD65 and GAD67 with different intracellular distribution and activity. We focused on GAD because of 1) the unambiguous expression in GABAergic neurons (and beta-cells of the pancreas), 2) the importance of this enzyme in synthesis of the major inhibitory neuronal transmitter, which comprises approx. 30-40% of all neurons in the brain, and finally, 3) because of the pivotal role of GABAergic neurons in neuronal network homeostasis and neurological disorders such as stroke and Huntington's disease¹¹⁶⁻¹¹⁸. The GAD-specific decarboxylation of glutamate was used as a motive, which is mimicked by the responsive contrast agent to facilitate a highly specific change in relaxivity.

The experimental schedule included the following subprojects:

- 1) *Comparison of MRI sequences for stable and reliable determination of T_1 relaxation rates.*
- 2) *Evaluation of Gd-DO3A-GAD relaxivity in tissue lysates.*
- 3) *Setting up a GABAergic cell system based on the differentiation of embryonic stem cells, which allows relaxometry on cell pellets.*
- 4) *Optimization of the cell labeling procedure, based on a comparison of different methods (pinocytosis, lipofection, Calciumphosphate precipitation and electroporation).*
- 5) *Characterisation of relaxivity changes induced by the GAD enzyme in the cellular compartment by applying the optimized labeling protocol.*
- 6) *Proof-of-concept study of imaging GABAergic neurons with MRI.*

The results of this section are available in the following publications:

Aswendt M, Gianolio E, Pariani G, Napolitano R, Fedeli F, Himmelreich U, Aime S, Hoehn M (2012) In vivo imaging of inhibitory, GABAergic neurons by MRI. *NeuroImage* 62(3):1685-93.

Napolitano R, Pariani G, Fedeli F, Aswendt M, Aime S, Gianolio E (2013) Synthesis and Relaxometric Characterization of a MRI Gd-based probe responsive to GAD enzymatic activity. *Journal of Medicinal Chemistry* (Epub ahead of print).

3.2 Results

3.2.1 MRI sequence validation

For a quantitative comparison of T_1 relaxation rates, the nickel standard phantom was measured with 3 different MRI sequences, comprising the variation of TR (RAREVTR, MSME_TR and FLASH_TR) and TI (MSME_TI, FLASH_TI). The data fitting was optimized for each sequence to yield reliable r_1 (Figure 14), which were compared to the expected values at 4.7 T (Figure 15A). These measurements revealed stable relaxivities for all sequences, except for FLASH with variable TR, with best fitting to the expected r_1 for the MSME_TR and RAREVTR sequence. The MRI sequences were adapted to the Gd-DTPA phantom and r_1 was again determined (Figure 15B) revealing comparable values for all sequences. The RAREVTR sequence was chosen for further tests because of its superior time-efficiency, and reproducibility between both separate MRI sessions and Gd-DTPA phantoms (Figure 15C and D).

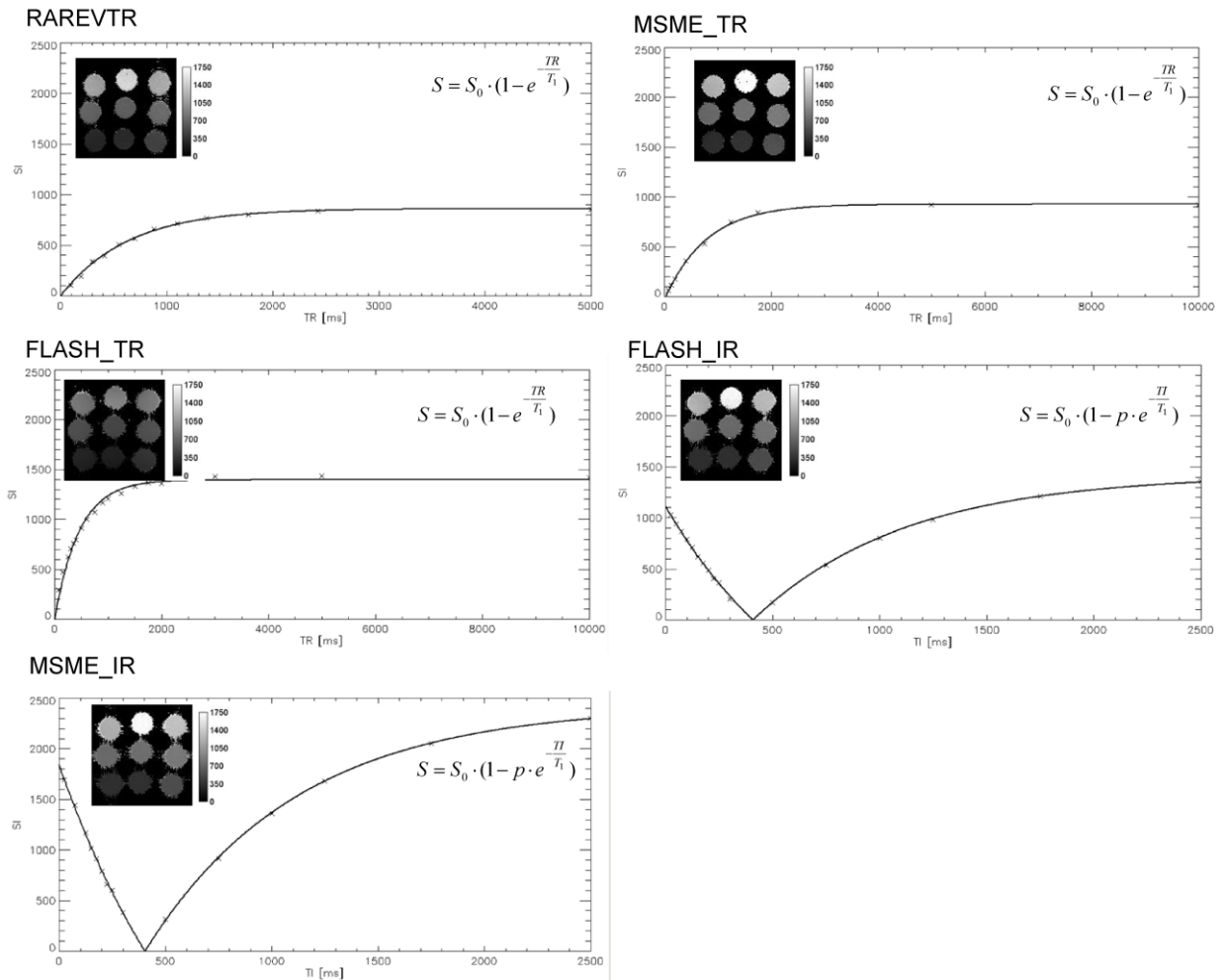


Figure 14: Schematic overview of the monoexponential fit for determining T_1 relaxation. Representative fits are displayed for the central image pixel. The resulting T_1 maps are depicted on the upper left of each graph with equal scaling for 0-1750 ms T_1 , illustrating the apparent differences in the resulting T_1 map.

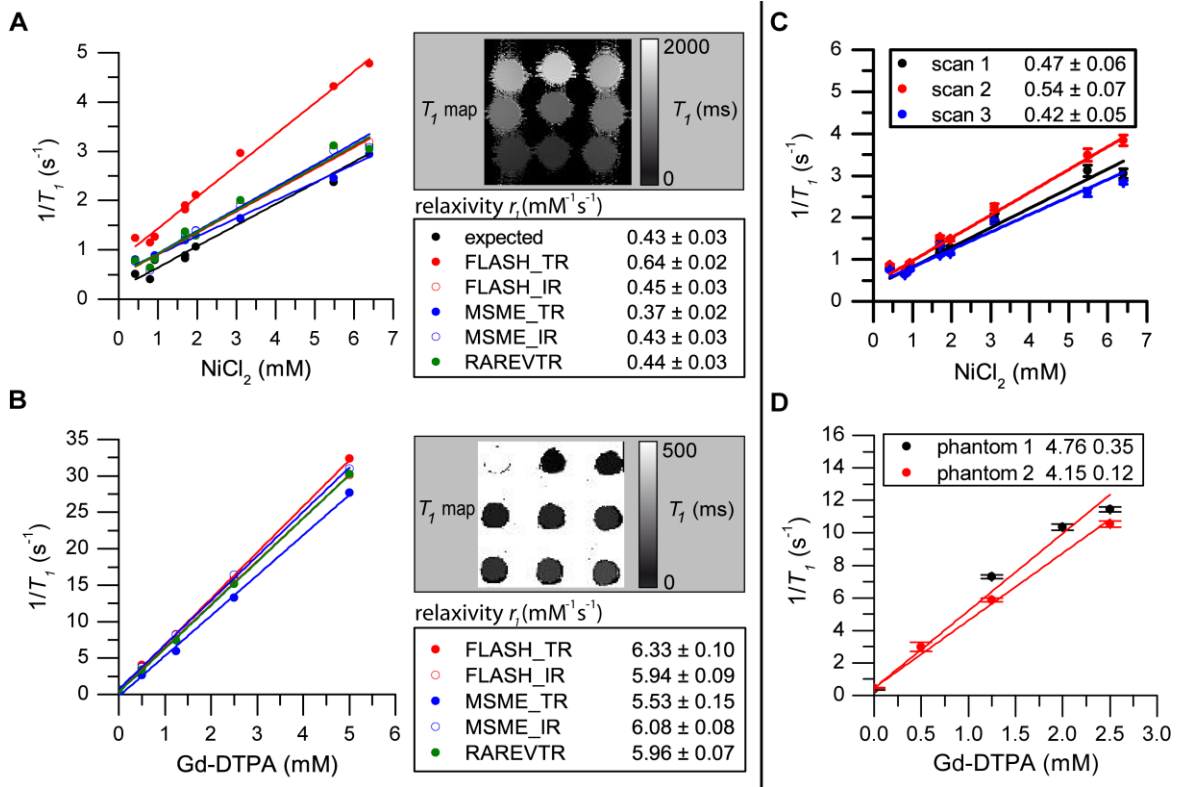


Figure 15: Evaluation of MRI sequences for T_1 relaxivity. A) Comparison of different sequences on the Nickel standard phantom at 4.7 T (representative T_1 map, upper right) revealing relaxivity values for MSME_IR and RAREVTR close to the expected values¹¹⁹ (expressed as relaxivity \pm standard deviation). B) Same sequences were used to determine Gd-DTPA relaxivity at 4.7 T with a phantom consisting of a Gd-DTPA dilution series (representative T_1 map, upper right). C) Stability of RAREVTR scans on the same Nickel standard phantom – separate scan on separate days revealed robust determination of T_1 . D) Stability of RAREVTR scans for determining T_1 on different phantoms.

Finally, the RAREVTR sequence was validated for robust in vivo measurements by comparing rat and mouse values at low field strength (4.7 T) and high field strength (11.7 T). According to the field strength-dependent relaxivity of paramagnetic contrast agents, the T_1 values for the rat brain increased with magnetic field strength (e.g. rat cortex approx. 200 ms difference). The measured T_1 values at 11.7 T were in good agreement with data reported by de Graaf *et al.*³⁴ (Figure 16).

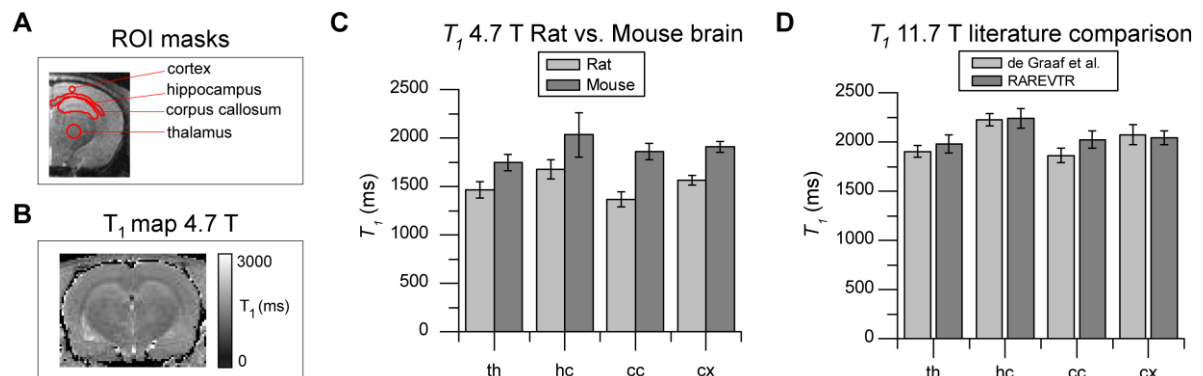


Figure 16: In vivo verification of the RAREVTR sequence. A) ROI analysis on coronal brain images was used to extract T_1 values from B) T_1 maps in anatomical brain regions. C) RAREVTR was suitable to determine T_1 on mouse and rat brains. D) Previously published T_1 values of the rat brain³⁴ correlated highly with the experimentally acquired using the RAREVTR sequence at 11.7 T.

3.2.2 Novel responsive contrast agent for detection of GAD activity

The chemical basis of the novel responsive contrast agent Gd-DO3A-GAD^V is a Gd-DO3A moiety bearing a long, highly flexible substituent that ends up with two glutamate residues on which the GAD enzyme is intended to decarboxylate. The two glutamate moieties are expected to compete with water for the two axial Gd(III) coordination sites, and thus their presence results in a low relaxivity system. The removal of the carboxylates by GAD yields an increase in the observed relaxivity. To avoid the cleavage of the peptidic bonds by endo-peptidases, the amidic nitrogens formed upon conjugation of the glutamate residues have been selectively methylated. In order to avoid steric constrain in the access to GAD active site, the glutamate moieties have been separated from the Gd-chelate by a long and flexible linker (Figure 17).

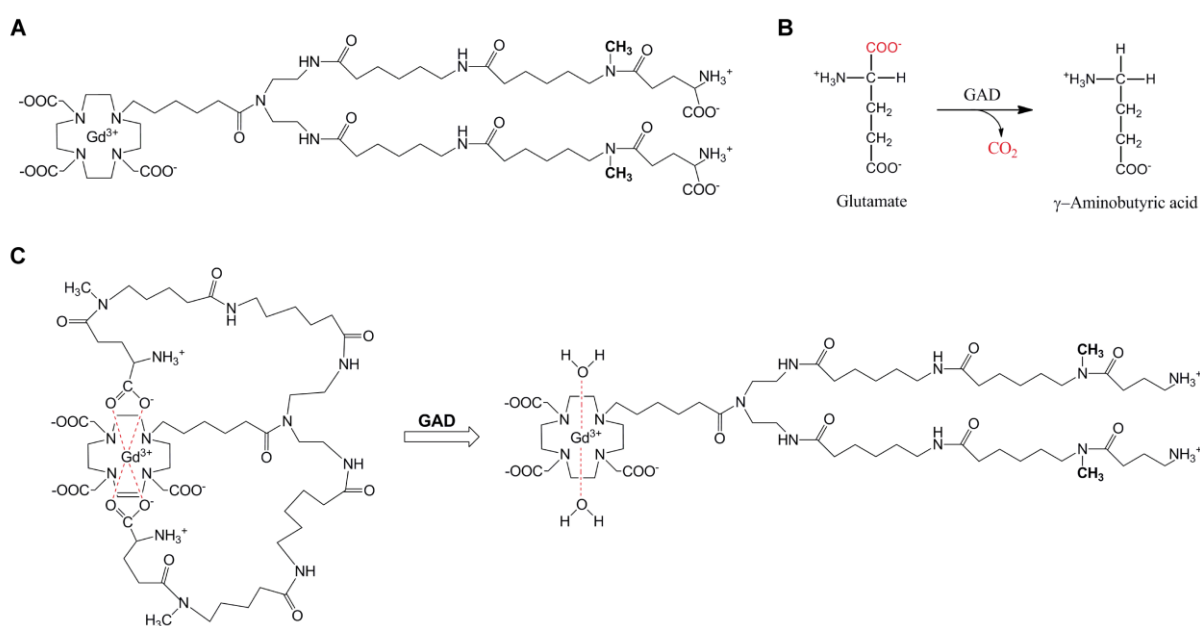


Figure 17: Schematic representation of Gd-DO3A-GAD structure and processing by the GAD enzyme. **A)** The chemical structure of Gd-DO3A-GAD reveals the core chelate DO3A structure and the long linker arms bearing the 2 glutamate moieties. **B)** Enzymatic reaction converting glutamate into GABA driven by GAD. **C)** Schematic representation of Gd-DO3A-GAD structure and processing by the GAD enzyme, which releases Gd coordination by the glutamate residues and enables free water access, resulting in an increased relaxivity¹¹⁴.

3.2.3 Characterization of GAD-dependent contrast agent activation in tissue lysates

For the initial test of GAD-dependent relaxivity changes upon contrast agent activation, crude tissue lysates with a specific buffer to preserve enzyme activity were incubated for 24 h at 37°C in the presence of Gd-DO3A-GAD, and subsequently T_1 relaxation times were acquired. Western Blot analysis was used to identify GAD65/67 in tissue lysates (Figure 18 A). Rat brain lysates from the cortex and cerebellum exhibit strong GAD65/67 protein expression, in contrast, the in the liver the enzyme is absent. This is reflected in the T_1 maps: a decrease in T_1 relaxation time was only detectable in the

^V Gd-DO3A-GAD: 1-[5-[[N,N'-bis-[3,10,17-triaza-4,11,18-trioxo-21-carboxyl-21-amino]eicosane]]-N-methylaminocarbonyl]pentyl]-1,4,7,10-tetraazacyclododecane-4,7,10-triacetate (3-) gadolinate

presence of GAD65/67 in cortex and cerebellum (Figure 18 B). Based on the T_1 maps, a quantitative comparison was made to extract changes in relaxation rates before and after addition of Gd-DO3A-GAD, which revealed a 2-fold higher ΔR_1 in the brain samples compared to the liver sample (Figure 18 C). The relaxivity behaviour was further studied at different magnetic field strengths by acquiring NMRD profiles, which exhibited the highest relaxivity shift useful for MRI at 1 T (or 40 MHz). The NMRD profiles were also obtained for identifying the specificity of GAD mediated contrast agent activation by addition of the GAD specific inhibitor AOAA to the brain lysates (Figure 18D).

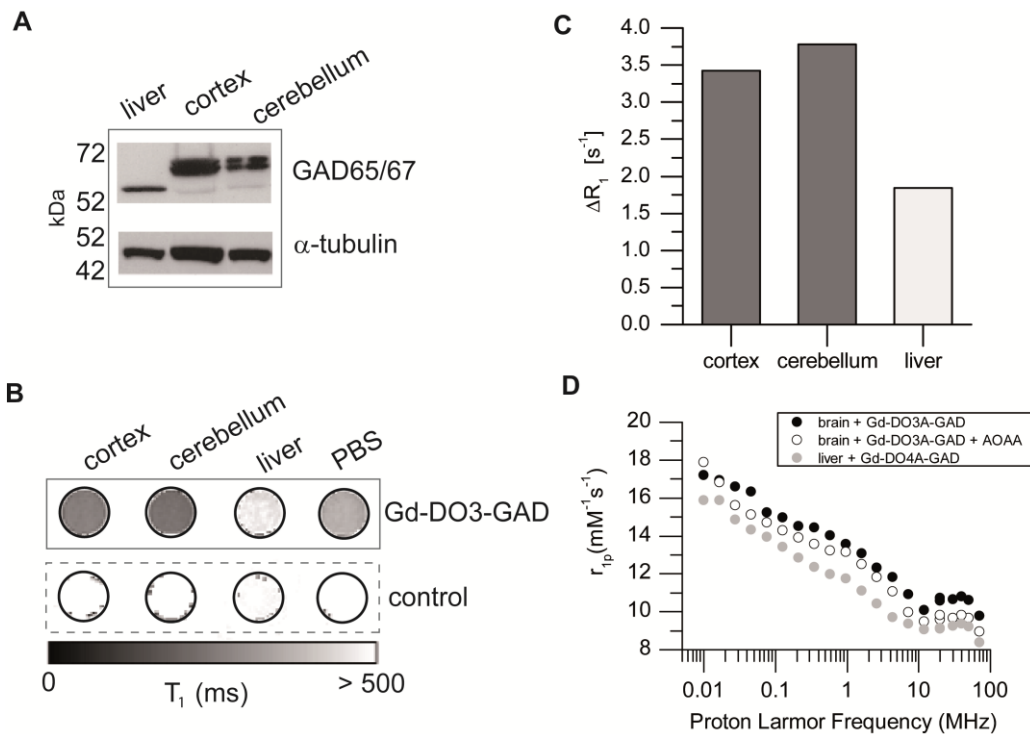


Figure 18: GAD-dependent relaxivity increase in tissue lysates. A) Confirmation of GAD65/67 in brain lysates expression by western blotting, alpha-tubulin as loading control. B) T_1 map acquired for MRI phantom of tissue lysates revealed a decrease in T_1 relaxation time after incubation with Gd-DO3A-GAD compared to the control situation. B) This MRI phantom was used for quantitative analysis. ΔR_1 was increased for brain lysate compared to liver lysate. D) NMRD profile revealing the paramagnetic characteristic relaxivity field dependence and the specificity of Gd-DO3A-GAD activation. Upon addition of the GAD-specific inhibitor AOAA, relaxivity decreased substantially.

3.2.4 Differentiation protocol for GABAergic neurons from embryonic stem cells

Relaxometry studies on a cellular level require a substantial amount of cells for labeling and subsequent MRI measurements. In case of GABAergic neurons, this is hampered by the absence of stable and commercially available cell lines. Therefore, a protocol was set up, which allows the robust generation of several million of GABAergic neurons in approx. 10 days by differentiation of the embryonic stem cell line CGR8. The novel three-step protocol consists of 1) formation of embryoid bodies (EBs), 2) selection of neural precursor cells (NPCs) in chemically defined medium, and 3) differentiation of NPCs into inhibitory neurons (Figure 19 A). The presence of the GAD65/67 proteins, was confirmed by western blot and by ICC (Figure 19 B, D). The final proportion of betaIII tubulin and

GAD65/67 positive neurons was 31% and 27%, respectively. Neuronal differentiation was not impaired in the presence of Gd-DO3A-GAD, as labeled stem cells exhibited only slightly reduced proportion of GABAergic neurons (Figure 19 C). Marker up- and downregulation reflecting the transition from pluripotency to mature neurons was studied with qPCR for every protocol step. Relative gene expression in relation to expression of the housekeeping gene GAPDH in CGR8 cells revealed 1) the downregulation of the pluripotency marker Oct4, 2) the maximum Nestin expression under NPC selection conditions, and 3) the selective upregulation of the mature neuronal marker betaIII tubulin in conjunction with GABAergic specific GAD1 and GAD2 in the final step (Figure 19 E).

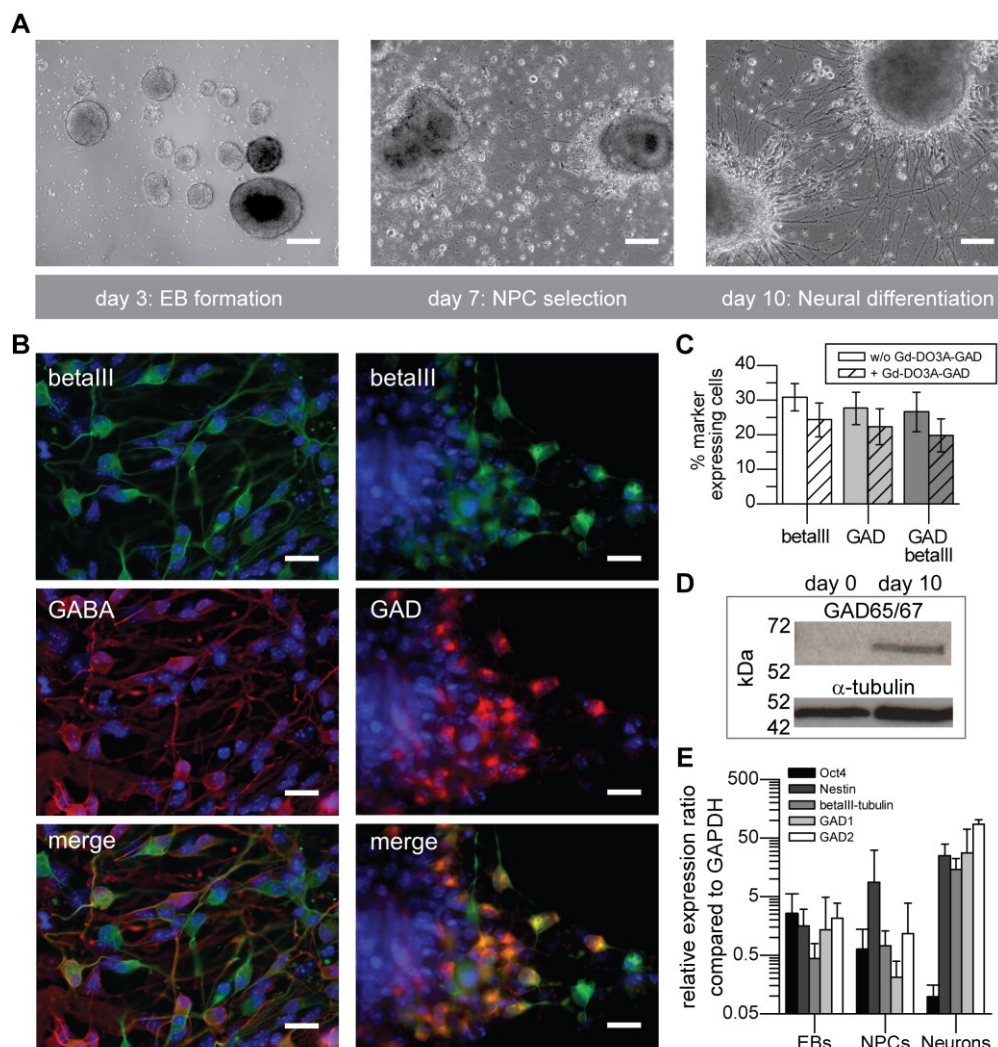


Figure 19: Evaluation of the GABAergic differentiation protocol: A) Principle of the 3-step protocol lasting for 10 days illustrated by bright-field microscopy of the EB formation, selection of NPCs and the differentiation of NPCs. (scale bar 100 µm). **B)** Existence of GABA and GAD65/67 coexpressed by majority of cells after differentiation protocol proven by IHC (scale bar 20 µm). **C)** Detailed quantitative analysis of marker expression in differentiated cultures revealed high proportion of GAD65/67 expressing neurons. Labeling of cells prior to differentiation resulted in only slightly (not significant) decreased GABAergic differentiation. **D)** Western blotting revealed GAD65/67 only present in differentiated cultures. **E)** qPCR analysis reflects protocol step dependent upregulation of neuronal marker (betaIII, GAD) and downregulation of pluripotency marker (Oct4).

3.2.5 Evaluation of the optimal Gd-chelate labeling procedure

Stem cell labeling with MRI contrast agents depends on specific protocol optimization for minimizing toxicity effecting pluripotency and differentiation potential. In order to determine the best method, 4 different approaches were compared using the clinically used contrast agent Dotarem®, which shares the Gd(III) chelate chemical structure with Gd-DO3A-Gad: 1) unspecific endocytosis/pinocytosis (pino), 2) calcium phosphate precipitation (CaP), 3) lipofection (Lipo), and 4) electroporation (EP). Viability and survival rate were assessed for each method, revealing no effect for endocytosis. In contrast, calcium phosphate, lipofection and electroporation lead to a decreased survival rate without affecting viability of the cells, indicating a detrimental effect of the incorporated contrast agent (Figure 20 A). The efficiency of contrast agent uptake was determined by ROI analysis on T_1 maps of MRI phantoms containing labeled cells at 4.7 T. The ΔR_1 values indicate a minimal unspecific uptake of contrast agent by endocytosis and calcium phosphate precipitation. Higher contrast agent uptake, as indicated by stronger changes in ΔR_1 (factor 2.4) was observed for lipofection and electroporation treatment (Figure 20 B). Although electroporation served as the most convenient method for stable and high contrast agent uptake, the influence on viability/survival needed to be minimized by a specific protocol, which includes HBSS buffer and a single square wave at 100 V with a pulse length of 20 ms. This final protocol was applied to the undifferentiated and differentiated CGR8 cells in the presence of Gd-DO3A-GAD without impact on viability and low impact on cell survival (decreased to 53–72%) (Figure 20 C). IHC analysis showed no difference in potential of these labeled cells to constitute a GABAergic culture (see Figure 19 C).

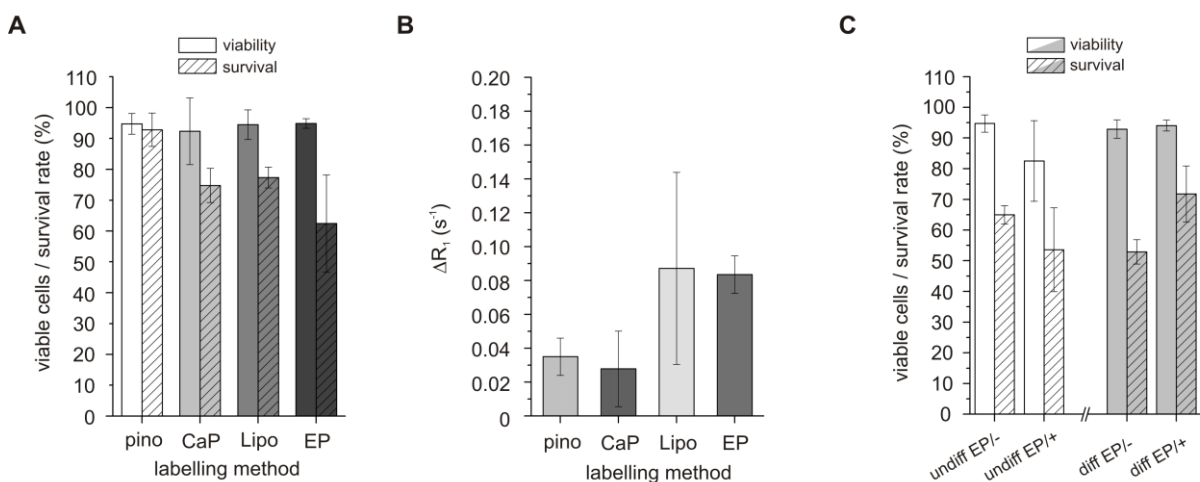


Figure 20: Optimization of cell labeling approaches with paramagnetic contrast agents. A) Cell viability was not impaired by the labeling procedure. The survival rate for Calciumphosphate precipitation (CaP), lipofectio (Lipo) and electroporation (EP) decreased due to impact of the labeling procedure, but not due to the Gd-DTPA. B) High contrast agent uptake was only possible with Lipo and EP, as confirmed by the changes in relaxation rate of labeled cell vs. unlabeled cell pellets. C) An optimized EP protocol was applied to the undifferentiated and differentiated ES labeling with Gd-DO3A-GAD. Independent on the cell status, viability was not impaired, but the survival rate decreased slightly compared to Gd-DTPA¹¹⁴.

3.2.6 GABAergic neuron-specific contrast in vitro

Applying the optimized labeling protocol permitted the discrimination of native and differentiated ES cells based on the T_1 relaxation rates. Labeled cells were incubated for 6 h to allow complete activation of Gd-DO3A-GAD and subsequently measured in MRI phantoms at 1 and 7 T (Figure 21). At both field strengths, independent experiments proved the substantial difference between ES cells and GABAergic neurons based on the measured T_1 values. Notably, such experiments showed high fluctuations and averaging depends on prior normalization, either by considering the actual number of vital cells or the Gd(III) content. The correction of the actual contrast agent uptake turned out to fit better the expected high difference between low- and high field (see NMRD profile, predicting relaxivity behavior for low and high field, Figure 18). Nevertheless, all in vitro experiments predicted a T_1 difference at 7 T still ≥ 100 ms, which promised an in vivo application at high field strength.

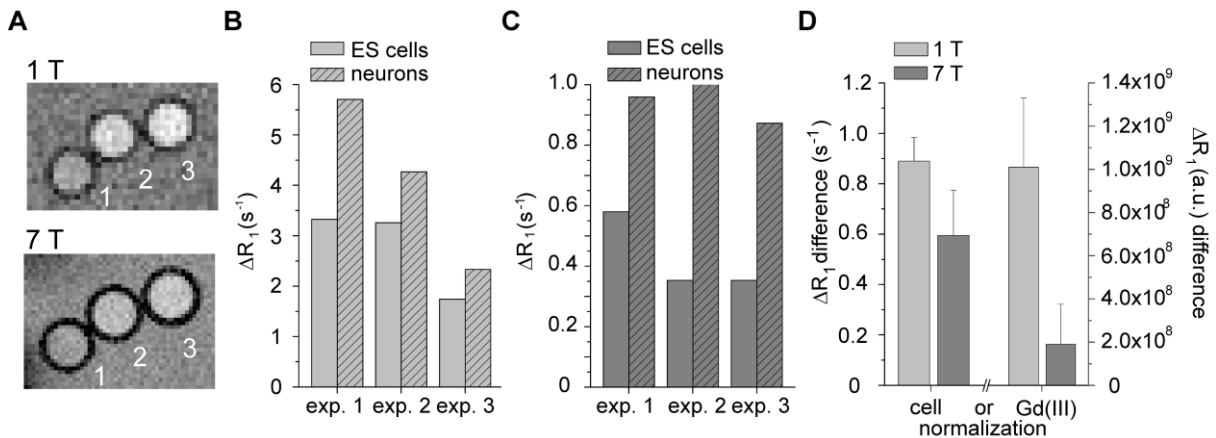


Figure 21: Relaxometric discrimination of native ES cells and GABAergic neurons based on the relaxivity change of Gd-DO3A-GAD in the presence of GAD. A) T_1 maps of a MRI phantom containing PBS (1), ES cells (2) and neurons (3) acquired at 1 and 7 T. **B and C)** Changes in relaxation rate calculated for 3 independent labeling experiments at 1 T and 7 T. At both field strengths, the T_1 difference was sufficient to discriminate between undifferentiated and differentiated cells. **D)** The normalization of these relaxation rate changes based on the actual cell number for each experiment or the Gd(III) content per mg protein, revealed a stronger effect for the second method¹¹⁴.

3.2.7 In vivo cell imaging at high field strength

The in vitro experiment was transferred to in vivo conditions, by grafting 750,000 pre-labeled undifferentiated and differentiated cells into the left and right striatum of nude mice, respectively (n=2). MRI was performed at 7 T directly after transplantation and followed for up to 1 week. T_1 maps were evaluated to calculate the change in relaxation rate between the ES cell graft and the differentiated graft (Figure 22). The T_1 -weighted image and the T_1 map at 0.5 h after transplantation clearly depict the substantial image contrast difference between the two cell grafts. Further analysis at each time point revealed a strong T_1 difference > 100 ms, as predicted from the in vitro experiments. This contrast was lost by day 7. The final histological evaluation of graft location revealed a symmetric distribution corresponding to the MR images (Figure 22 D).

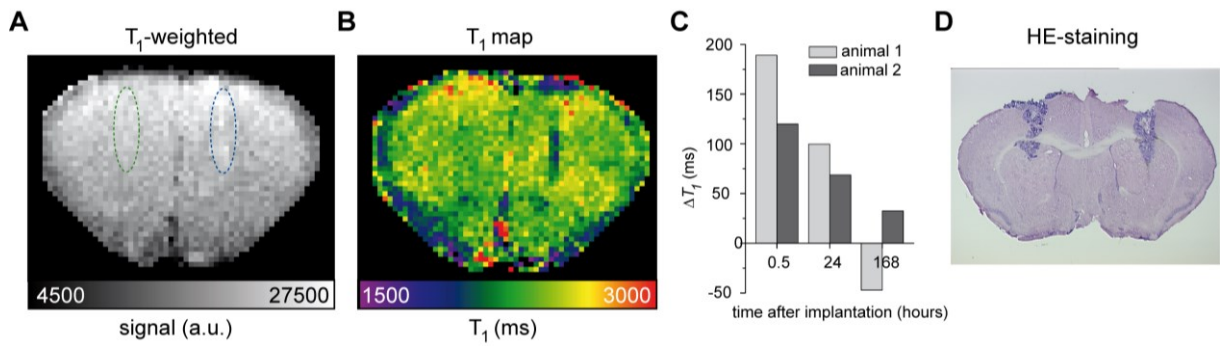


Figure 22: In vivo application of Gd-DO3A-GAD to discriminate grafted GABAergic neurons from ES cells. **A)** Representative T_1 -weighted image at 0.5 h after implantation of pre-labeled GABAergic neurons (right striatum) and ES cells (left striatum). **B)** Corresponding T_1 map revealing substantially lower T_1 values for the neuronal implant. **C)** Quantitative evaluation of the ΔT_1 between both cell grafts from 2 animals monitored for up to 7 days reflects a decrease of contrast over time. **D)** HE-staining for histological localization of the cell grafts 7 days after transplantation¹¹⁴.

3.3 Discussion

Molecular probes bioengineered to respond to processes, which are directly coupled to neuronal cell function are under strong investigation and intended to bridge noninvasive observation of molecular events with pathophysiological processes during disease state¹²⁰. The GAD-responsive probe, presented here, marks the first development of a MRI contrast agent, which is selectively activated by a neuron-specific enzyme, and is proven to discriminate GABAergic neurons based on T_1 relaxation changes.

3.3.1 Validation of RAREVTR sequences for stable and reliable T_1 determination

The best MR sequence for measuring T_1 relaxation for both in vitro MR phantoms and in vivo conditions was empirically determined by comparing gradient echo (FLASH) and spin echo (MSME, RAREVTR) sequences, with variable TR or TI. In a first step, the sequences were applied to the nickel standard phantom, which contains defined concentration of NiCl_2 , H_2O , D_2O and agarose with known T_1 relaxation rates. In these experiments, the r_1 determined by the inversion recovery sequence MSME_IR correlated best with expected values. The RAREVTR sequence gave similar results within 1/10 the acquisition time. Based on these results, sequences were optimized in terms of resolution (234 μm in plane) and imaging time (fastest method: FLASH_TR 30 min). Again the RAREVTR sequence was best in terms of acquisition time and precise r_1 . Further tests on the RAREVTR stability for separate scan sessions and on different Gd-DTPA phantoms revealed strongly coherent data limited only by the general MR imaging noise and the phantom preparation. Finally, the RAREVTR sequence was also tested under in vivo conditions. The sequence was used to obtain T_1 relaxation times of rat and mouse brain at low magnetic field 4.7 T. However, also at high magnetic field (11.7 T), the acquired values for the rat brain are in accordance with literature values³⁴. In conclusion, the RAREVTR sequence enabled stable determination of T_1 for in vitro and various in vivo applications.

3.3.2 Contrast agent mechanism

The design of Gd-DO3A-GAD is a further development of established responsive probes, namely the first reported enzyme-activated gadolinium chelate by Moats, Fraser and Meade⁴³. According to the concept described there, Gd-DO3A-GAD has been made responsive to the GAD-decarboxylation by two glutamate groups, which block free water access to Gd(III) and suppress the relaxivity. These masking groups are cleaved specifically by the enzyme GAD leading to an increased relaxivity based on the elevated access of water molecules to the paramagnetic core. This contrast agent processing, accompanied with a relaxivity shift, was proven in GAD-containing tissue lysates and could be diminished by addition of a GAD-specific inhibitor. The enzyme co-factor PLP plays a crucial role in efficient

contrast agent processing, because the GAD inhibitor AOAA, selectively traps PLP. Therefore, lysates were supplemented with additional PLP to facilitate the reaction. Based on the acquired NMRD profiles the representative field dependence relationship for r_1 relaxivity was observed, where deviations are most likely due to the crude lysate mixture, substantially different to ideal water solutions. Further chemical analysis of the contrast agent processing and potential unspecific complexing of the agent to macromolecules, especially in lysates, is reported elsewhere (Napolitano *et al.*, in revision).

3.3.3 GABAergic differentiation protocol

To establish a cell model for relaxometric tests of Gd-DO3A-GAD, a differentiation protocol was most suitable to generate several millions of cells, required for one MRI phantom experiment. Based on previous reports, the ES cell line CGR8 was chosen, which grows feeder-layer independent and is able to generate GABAergic neurons *in vitro*¹²¹. The novel differentiation protocol described here, is based on the five-stage method introduced by Okabe¹²², but generates comparable number of GABAergic neurons (approx. 30% neurons of which 89% were GABAergic) in 10 days instead of 2-3 weeks. The simplified 3-step protocol was proven by western blot and qPCR to produce neurons with the GAD65/67 enzyme. Furthermore, the qPCR profile reflects each protocol step, namely the increased Nestin expression during NPC selective conditions, the decrease of the pluripotency marker Oct4 over time, and finally, the onset of GAD1 and GAD2 expression in the last step.

3.3.4 Labeling of stem cells and derivatives with paramagnetic agents

Appropriate to the differentiation procedure, the labeling protocol had to be developed for the ES cells and the differentiated neurons. Four different methods were chosen based on previous reports proving the usefulness when using superparamagnetic contrast agents, and compared relating to cell viability and labeling efficiency: pinocytosis, lipofection, calcium phosphate precipitation and electroporation. Pinocytosis describes the unspecific uptake of contrast agent and turned out to be not effective at all for labeling. Lipofection and CaP were already used for labeling of ES cells and NPCs with ironoxide-based contrast agents¹²³ and Gd(III) chelates¹²⁴. In the experiments reported here, lipofection facilitated contrast agent uptake better than CaP, without effecting viability. The uptake variability is probably due to the random process of contrast agent complexing with the liposome. The contrast agent is finally stored in intracellular vesicles, which can change relaxivity¹²⁵. Electroporation induces direct intracellular contrast agent uptake by the formation of small pores in the membrane and was selected for the labelin with Gd-DO3AGAD. The method was already applied for incorporation of iron oxide particles, as well as Gd(III) chelates^{125,126}. For the experiments reported here, the protocol was optimized to yield $\geq 92\%$ viability and $\geq 62\%$ survival rate in the presence of 50 mM Gd-DOTA, which was only slightly decreased by Gd-DO3A-GAD.

3.3.5 T_1 relaxation dependent discrimination of GABAergic neurons

In a first application step, undifferentiated and differentiated cells were labeled with Gd-DO3A-GAD and imaged for T_1 -dependent contrast differences at 1 and 7 T. Quantitative T_1 maps confirmed higher relaxation rates at low field compared to high field strength, in agreement with the theory. Furthermore, the GAD-specific activation of Gd-DO3A-GAD could be proven in three independent experiments by the strong increase in $\Delta R1$. Because of the multi-step process, these values tend to vary and should be normalized to the cell number, or even better, to be more precise, normalized to the Gd(III)/protein content. The comparison of both correction methods revealed a stronger field-dependence for the Gd(III) content calculation, which is most likely due to variable amount of contrast agent taken up by individual cells. However, these results promised the usefulness of Gd-DO3A-GAD for cell tracking at high magnetic fields, which was investigated in the final in vivo experiment. Until now, only a minority of novel responsive contrast agents have been used for in vivo imaging^{127,128}, although various biological processes were already targeted in vitro¹²⁹. However, in the present study the first proof-of-principle discrimination between grafted stem cells and differentiated cells was achieved using in vivo MRI. In line with the in vitro experiments, predicting a change in T_1 relaxation rate ≥ 200 ms, the in vivo analysis revealed ≥ 100 ms, still enough for robust discrimination of labeled ES cells and GABAergic neurons. Although, normalization seems to be important for quantitative analysis, until now a similar procedure cannot be applied in vivo¹³⁰. Nevertheless, such a method would be important in order to determine quantitatively the proportion of pre-labeled stem cells differentiating into GABAergic neurons and simultaneously changing relaxivity of Gd-DO3A-GAD.

3.4 Conclusion and Outlook

In this study, cell specific MR imaging was shown based on a novel contrast agent responsive to the GAD enzyme in GABAergic neurons. This contrast agent based method is in line with the first reports on imaging neurotransmitter¹³¹ and brain-specific receptor¹³², which will definitely expand the potential of MRI for a functional readout on the cellular level. The responsive probe presented here, proved for the first time a neuronal enzyme-specific MRI signal. The contrast agent chemistry is still developing rapidly, e.g. generating cell-penetrating probes with increased intracellular retention. Such improvements could facilitate molecular probes, as Gd-DO3AGAD, for the longitudinal monitoring of GABAergic differentiation in “real time”. The validation of a responsive probe for ES cells and neurons, set the basis for future transplantation studies and will enable the functional readout required to monitor the success in stem cell therapy of neurodegenerative disease, like Huntington’s disease or stroke.

4. BOOSTING BIOLUMINESCENCE FOR SENSITIVE NEUROIMAGING

4.1 Project aim and experimental setup

Optical monitoring of stem cell based therapies is strictly limited by imaging sensitivity. Being superior to fluorescence imaging, *in vivo* bioluminescence imaging (BLI) has become the optical method of choice for *quantitative* tracking of (stem) cells in *real-time* with *high signal-to-noise*. Nevertheless, BLI of grafted NSCs needs adaption to the complex brain application - like the selective substrate uptake through the blood-brain-barrier, light scattering and attenuation by the multilayer tissue barrier. The numerous reports on BLI in the mouse brain used nearly exclusively tumor cells^{73,133,134}, immortalized neural stem cells¹³⁵, mesenchymal stem cells¹³⁶ or lentiviral *in vivo* gene transfer¹³⁷ for a qualitative measurement of reporter gene expression.

The project reported here was initiated in cooperation with *Laura Mezzanotte and Clemens Löwik* (Department of Radiology, Leiden University Medical Center, Leiden, The Netherlands), *Rob Hoeben* (Department of Molecular Cell Biology, Leiden University Medical Center, Leiden, The Netherlands) and *Sébastien Couillard-Després* (Institute of Molecular Regenerative Medicine, Paracelsus Medical Private University, Salzburg, Austria). The *in vivo* performance of 4 luciferases was tested by overexpression in HEK-293 and NSCs after transplantation into the mouse brain. The standard BLI protocol was revised by analyzing the effect of anesthesia, substrate concentration and injection route using the DCX-Luc transgenic mouse model for brain specific BLI. Results were finally translated to intracerebrally transplanted Luc2+ NSCs, which could be detected with surpassing sensitivity.

The experimental schedule included the following subprojects:

- 1) *Establishing a mouse NSC line*
- 2) *Cloning of bimodal imaging reporter for lentiviral vector-mediated expression of Luc2, PpyRE9, CBG99 or hRluc coupled to copGFP in HEK-293 and NSCs*
- 3) *In vitro and in vivo characterization of BLI sensitivity of transgenic HEK-293 and NSCs*
- 4) *In vivo BLI protocol optimization (substrate concentration, injection route and anesthesia)*
- 5) *Determination of the sensitivity limit for transplanted Luc2+ NSCs in the mouse brain using the optimized protocol.*

The results of this thesis section are part of the following publications:

Aswendt M*, Adamczak J*, Couillard-Després S, Hoehn M (2013) Boosting Bioluminescence Neuroimaging: An Optimized Protocol for Brain Studies. PLoS ONE 8(2):e55662.

Mezzanotte L*, Aswendt M*, Tennstaedt A, Hoeben R, Hoehn M, Löwik C (2013) Quantitative evaluation of luciferases for *in vivo* bioluminescence imaging of neural stem cells. CMMI (in revision).

4.2 Results

4.2.1 D3WT_N2Euro – a radial glia-like neural stem cell line

Based on previous reports about the generation of NSCs from ES cells⁹³, a novel protocol was established. The murine ES cells D3WT were treated according to a 3-step protocol: 1) formation of neurosphere-like EBs under non-adherent conditions, 2) selection of adherent cells from the neurospheres on gelatin-coating, and 3) expansion of the EGF and b-FGF responsive cell population (Figure 23). The complete protocol lasts for approx. 25 days (days in vitro, DIV), followed by an additional passaging of the cells, during which 3 out of 20 colonies were selected for further characterization.

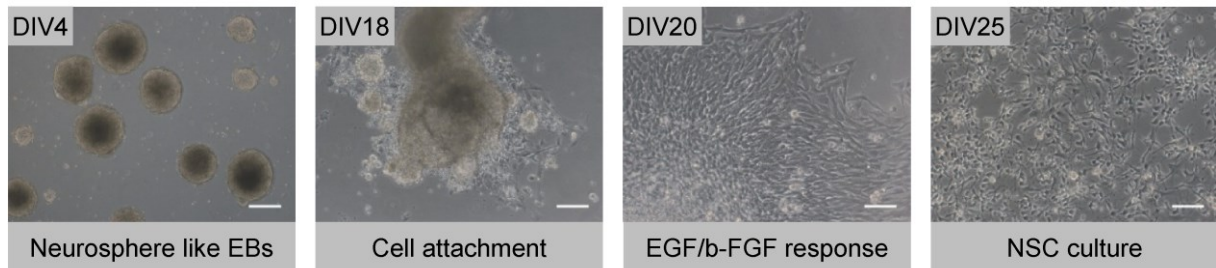


Figure 23: Protocol steps for generation of NSCs from the ES cells D3WT by chemically defined media composition and surface coatings in approx. 25 days in vitro (DIV). Phase contrast microscopy illustrates the 3-step process and the final cell morphology at DIV25 (10x magnification, scale bar 50 μ m).

Cell clone #1, 2 and 4 shared the homogenous bipolar morphology and stable propagation until DIV37 (Figure 24 A). All clones expressed homogeneously Nestin in the absence of GFAP with exception of clone #1, which contained single GFAP positive cells (indicated by arrow on Figure 24 B). Furthermore, clone #1 contained DCX positive neurons and clone #2 and #4 showed weak unspecific immunoreactivity for DCX (Figure 24 C). During the further cell passaging, only clone #4 showed persistent proliferation under EGF and b-FGF supplementation and was therefore selected as potential NSC line and further characterized.

Extensive gene profile analysis via RT-PCR of 20 genes for identification of ES cells, NSCs, NPCs, neurons, astrocytes, mesodermal cells and endodermal cells, was performed (Table 20, Figure 27). The immortalized NSC line C17.2 WT and data published by Conti *et al.*⁹³ were used as reference. Most importantly, cells derived from D3WT were found to lack the pluripotency marker (Oct4, Rex1, Nanog) and non-ectodermal marker (Brachyury and Gata6), but positive for NSC marker like Nestin, Musashi-1, Pax6 and Sox2. Markers for radial glia cells were also detectable (BLBP and 5T4). Based on this gene profile analysis, which revealed good accordance with previously identified marker sets⁹³, clone 4 was identified as neural stem cell line and further passaged. The cell line was termed D3WT_N2Euro cells, according to the cells of origin, the media component N2 and the culture medium Euromed. Notably, marker expression differed from the reference cell line C17.2 WT.

Retained stem cell properties were tested by culturing the cell line >33 passages (approx. 6 months of continuous culturing). Neural differentiation of these cells was driven either by cell culture sup-

plementation with 1% FCS (glial differentiation) or by culturing for 3 days in FGF only media and 7 days in N2/B27 media (neuronal differentiation). The ICC analysis of differentiated cells revealed a cell passage-independent strong expression of either glial (GFAP) or neuronal (DCX) proteins (Figure 25). A detailed qPCR analysis revealed differentiation protocol-dependent regulation of neuronal (DCX, betaIII, Map2, Synaptophysin), glial (GFAP, Glast, S100b) markers (Figure 25 B, D). Differentiation into the neuronal lineage resulted in 12x higher DCX, 2x higher MAP2 and 5x higher betaIII tubulin values compared to the glial differentiation. In contrast to pro-neuronal conditions, 1% FCS induced the up-regulation of glia-specific marker, e.g. Glast (2.8x-fold). Controversially, neuronal differentiation resulted in S100b 1.9x-fold and glial differentiation in 2.8x-fold Synaptophysin expression.

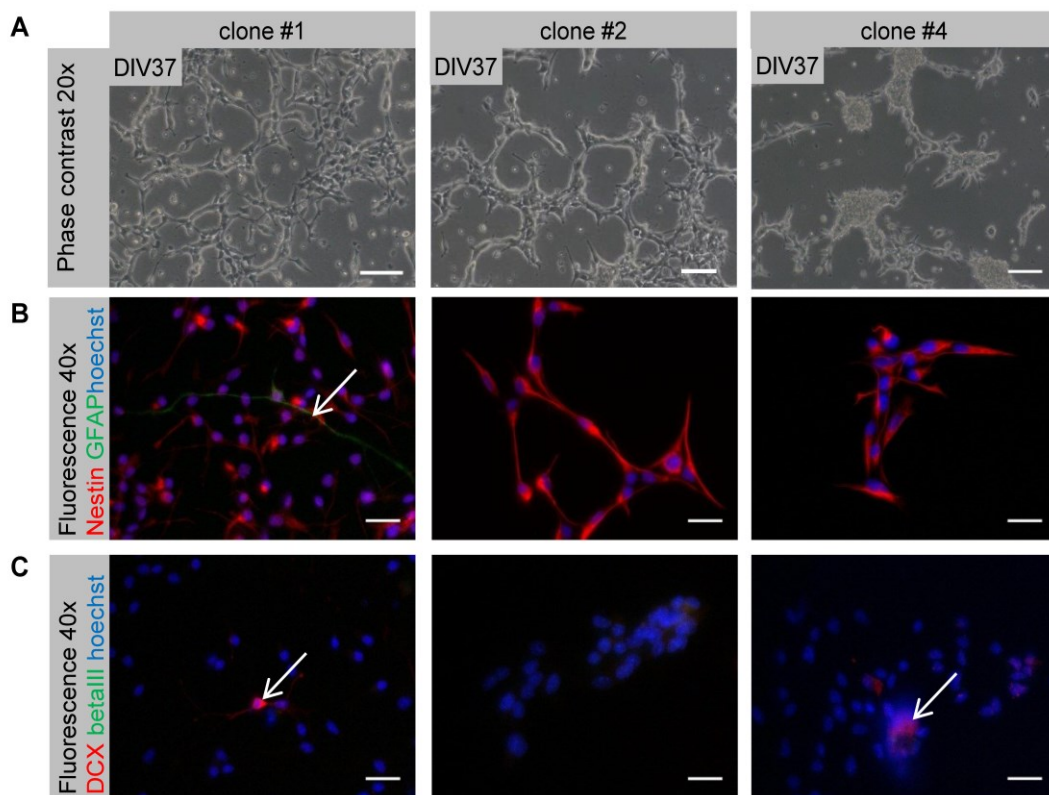


Figure 24: Morphological and immunocytochemical characterization of NSCs derived from D3WT ES cells. A) Phase contrast image showing homogenous bipolar structure of adherent cells (50 μm scale). B) Fluorescence microscopy of Nestin (red), GFAP (green) counterstained with Hoechst. C) Fluorescence microscopy of DCX (red), betaIII tubulin (green) counterstained with Hoechst (scale bar B and C 20 μm, 40x magnification).

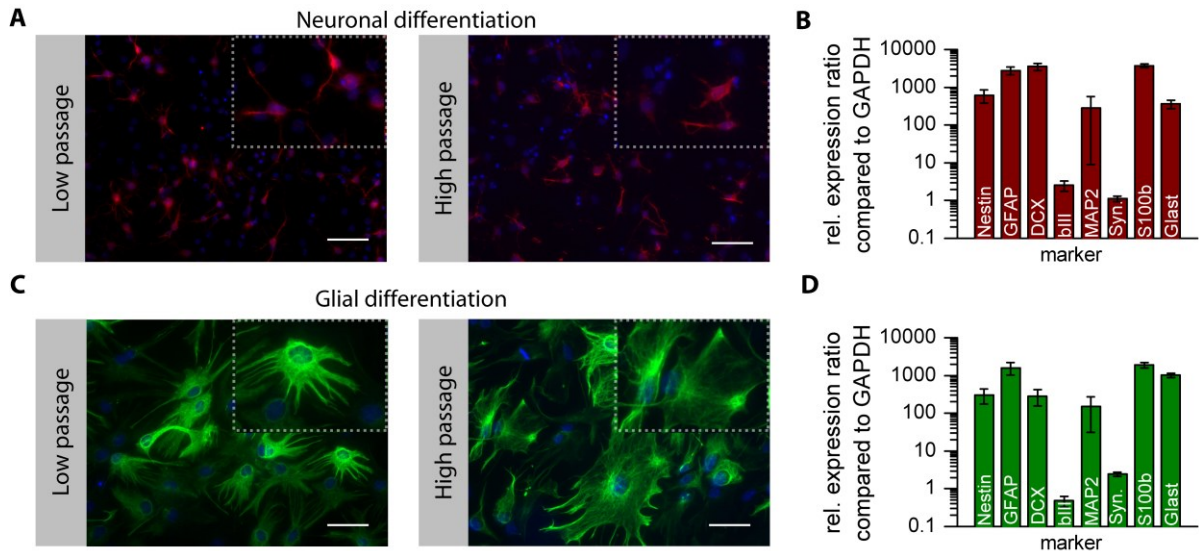


Figure 25: Differentiation of D3WT_N2Euro cells resulted in expression of neuron- and glia-specific marker. A) Neuronal differentiation into DCX-positive neurons for low and high cell passage. B) qPCR profile for the neuronal differentiation. C) Glial differentiation highlighted by ICC for high GFAP expression in low and high cell passage. D) qPCR profile for the glial differentiation (fluorescence microscopy, 40x magnification, zoomed pictures upper right, scale bar 50 μm).

Table 20 and Figure 26: Gene marker profile for D3WT_N2Euro compared to C17.2 and data published by Conti *et al.*⁹³

	Marker	D3WT_N2	C17.2	Conti <i>et al.</i>
Pluripotent embryonic stem cells	Oct3/4	-	-	-
	Rex-1	-	-	x
	Nanog	-	-	-
Neural stem cells	Nestin	+	+	+
	Pax6	+	-	+
	GFAP	-	+	-
	Sox1	-	-	-
	Sox2	+	+	+
Neural progenitor cells	Musashi-1	+	+	x
	DCX	-	-	x
	Prominin-1	+	-	x
	Olig2	+	-	+
Mature (neural) cells	NeuroD1	+	-	x
	5T4	+	+	+
	BLBP	+	-	+
	S100β	-	-	x
	NF-H	-	-	x
	Synaptophy-	-	-	x
Mesoderm	Galc	+	+	x
	Brachyury	-	-	x
Endoderm	Gata6	-	-	x
Control	Actin	+	+	+

	D3WT_N2Euro low passage	D3WT_N2Euro high passage	C17.2 WT	
Oct4	+	-	-	ESC
Rex-1	+	-	-	
Nanog	+	-	-	
BLBP	+	+	-	NSC/Npc
GFAP	+	+	-	
Musashi1	+	+	-	
NeuroD1	+	+	-	
Nestin	+	+	-	
DCX	+	+	-	
Pax6	+	+	-	
Sox1	+	+	-	
Sox2	+	+	-	
Prominin-1	+	+	-	Neuron Glia
Olig2	+	+	-	
S100beta	+	+	-	
GalC	+	+	-	
Synaptoph.	+	+	-	Control
NF-H	+	+	-	
Brachyury	+	+	-	
Gata6	+	+	-	
5T4	+	+	-	
Actin	+	+	+	

4.2.2 In vitro bioluminescence comparison in D3WT_N2Euro and HEK-293

HEK-293 and D3WT_N2Euro cells were stably transduced with self-inactivating lentiviral plasmids (EF1-Luciferase-T2A-copGFP) for expression of the luciferases Luc2, PpyRE9, CBG99 or hRluc coupled to the fluorescent reporter copGFP. The transduction resulted in approx. 80% positive HEK-293 and 30% positive NSCs. A FACS selection of a high expressing population ($>10^3$ counts) was only possible for the HEK-293 cells, whereas for the NSC only a middle expressing population could be selected (10^2 - 10^3 counts). All attempts to isolate cells with higher levels of copGFP failed, because of a progressive cell death. A comparable expression of the different luciferases within one cell type was achieved by FACS normalized to copGFP, whose expression is equimolar to the luciferase genes, due to the “self-cleaving” T2A sequence. After sorting, equal copGFP expression was validated by fluorescence microscopy and fluorescence measurements using a plate reader (Figure 27).

The in vitro sensitivity was determined by BLI of cell dilution series for HEK-293 and NSCs (Figure 28). In both cell lines, the luciferase signal was increased from PpyRE9 to CBG99 and Luc2 with highest signal for hRluc. The expected quantitative relationship between cell number and photon flux was detectable for both cell lines and every luciferase in vitro, by linear fitting with $R^2=0.99$. From this dilution series a ph/s/cell value was calculated for Luc2 ($3,412\pm 189$), PpyRE9 (837 ± 78), CBG99 ($3,119\pm 179$) and hRluc ($68,276\pm 18,077$). As expected from the different FACS gating and the copGFP expression, the luciferase expression differed substantially between both cell types – visible by the 4-6 fold increased photon flux of 1×10^3 HEK-293 compared to NSCs.

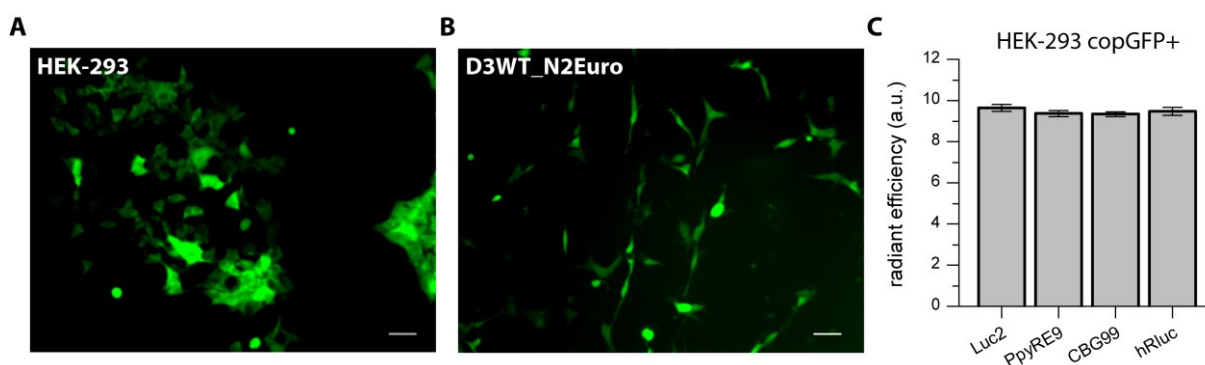


Figure 27: Transduced cells after FACS with equal expression of copGFP. A, B) Representative fluorescence microscopy images of HEK-293 and D3WT_N2Euro cells (scale bar 50 μm). C) Fluorescence imaging of 1×10^3 cells confirmed the equimolar expression of copGFP in the sorted and stably transduced cell lines with a mean radiation efficiency of 9.45 ± 0.13 .

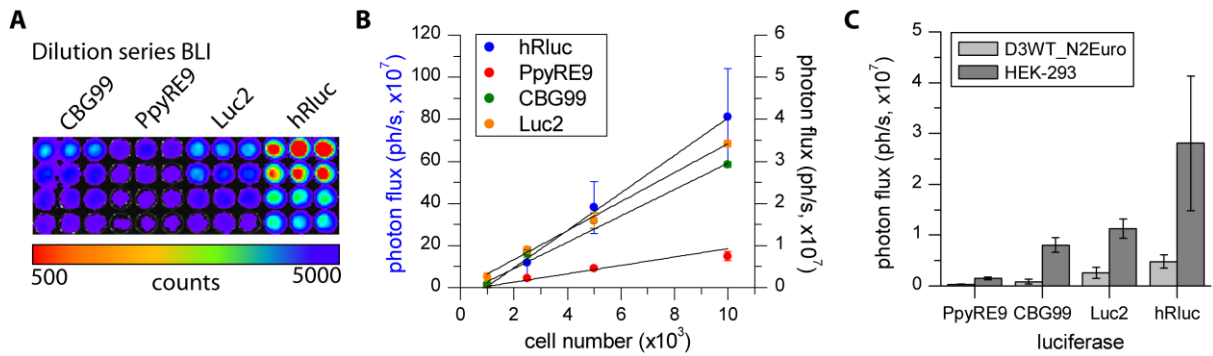


Figure 28: In vitro bioluminescence sensitivity determined by cell dilution series for all cell lines in two independent experiments. **A)** Representative image of a HEK-293 cell dilution series (1,000, 2,500, 5,000 and 10,000 cells). **B)** Corresponding quantitative relationship for D3WT_N2Euro cells. **C)** Photon flux comparison for D3WT_N2Euro and HEK-293 cells revealing higher BLI signal for HEK-293 cells independent of the luciferase type.

4.2.3 Bioluminescence imaging of cells grafted into the mouse brain

Initially the Luciferin- and Coelenterazine-dependent kinetic was investigated by acquiring every 20 min the luciferase signal for 30 s. Independent of the different kinetics in vitro, under in vivo conditions the signal from HEK-293-hRluc and -Luc2 cell grafts increased with a comparable curve until a time-to-peak of 15 and 16 min ($n=3$), as it is shown for a representative animal data set in Figure 29 A. On average for both substrates, time-to-peak values were between 12 and 16 min post ip injection. NSCs were transplanted in different amounts into nude mouse striatum (1×10^5 left, 3×10^5 right hemisphere, $n=3$) and recorded with BLI 24 h later for 1 min – 15 min after substrate administration (150 mg/kg D-Luciferin or 1.5 mg/kg CTZ-h). Superior signal was detectable for Luc2 followed by CBG99 and PpyRE9 with a detection limit of 1×10^5 (Luc2, CBG99) and 3×10^5 (PpyRE9). In contrast, neither 1×10^5 nor 3×10^5 hRluc cells were detectable (Figure 29 B). For a quantitative comparison of the luciferase performance in 3 transplanted animals, only the 3×10^5 cell graft revealed reliable data (Figure 29 C). BLI of hRluc expressing cells was only possible with transplanted HEK-293 cells (data not shown, only 1 animal), where 2×10^5 cells exhibited a photon flux of $92,600 \pm 12,347$ ph/s.

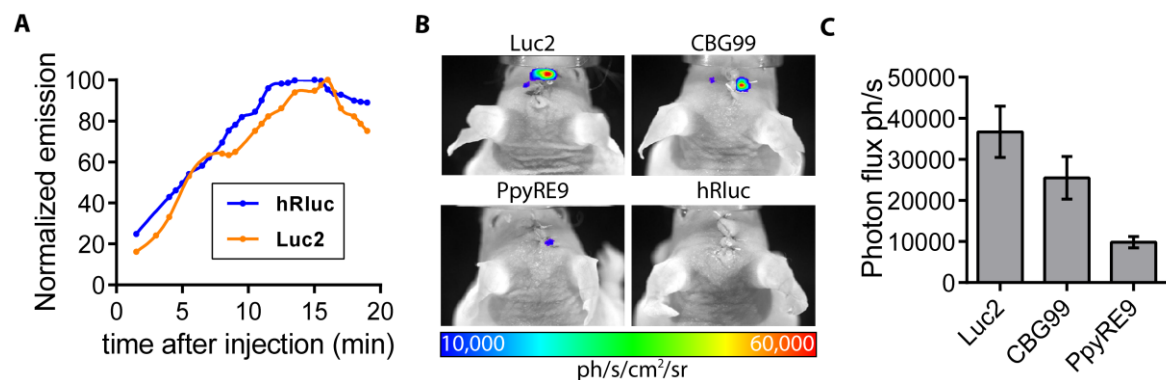


Figure 29: In vivo comparison of luciferases. **A)** Similar BLI time curves were acquired for Coelenterazine- and Luciferin-dependent luciferases with HEK-293. **B)** Representative images for nude mice grafted with 1×10^5 and 3×10^5 luciferase expressing NSCs. **C)** Quantitative analysis was done for 3×10^5 cells and revealed superior photon emission for Luc2 followed by CBG99 and PpyRE9 – the hRluc signal was not detectable.

4.2.4 Spectral luciferase analysis in vivo

For spectral analysis of in vivo BLI signals, a series of 20 nm bandpass filters was used, covering the luciferase emission spectra (520-680 nm). With this setup the emission spectra of D3WT_N2Euro cells expressing CBG99, Luc2 and PpyRE9 transplanted at 3 mm depth were compared. Luc2 and PpyRE9 spectra remain nearly stable for lower transplantation depths, but CBG99 becomes bimodal due to stronger absorption of light in the green region of the spectrum and better tissue penetration of light at red wavelengths. In an additional experiment, CBG99 cells were transplanted at 4 mm depth, which resulted in an increase in the red part of the spectrum, shifting almost completely.

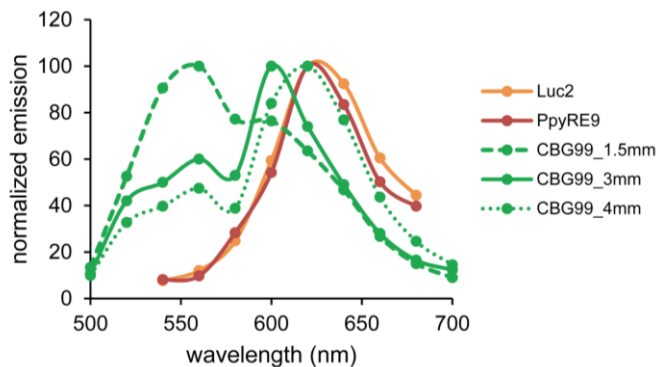


Figure 30: Emission spectra of Luc2, PpyRE9 and CBG99 under in vivo conditions acquired with a set of 20 nm bandpass filter. Luc2 and PpyRE9 show strong overlap and emission maxima merge at approx. 630 nm. Notably, the CBG99 emission peak shifts and the spectrum changed with implantation depth, serving as a specific predictor of graft location from the brain surface.

4.2.5 BLI protocol optimization

Validation of transgenic mouse model of neuroblast-specific BLI

Transgenic mice (n=4, 3-6 months) expressing luciferase under control of the neuronal doublecortin promoter DCX were used to optimize protocol parameters for brain-specific BLI. The animals were shaved prior to BLI on the head and back to reduce signal scattering and masking by the fur. To make measurements from different days and imaging conditions comparable, the unspecific signal from the back was subtracted from the brain signal (Figure 31). This weak unspecific signal appears most probably due to spontaneous oxidation of D-Luciferin. According to previous experiments, differences in this signal between animals reflect variations in substrate administration and Luc2 expression.

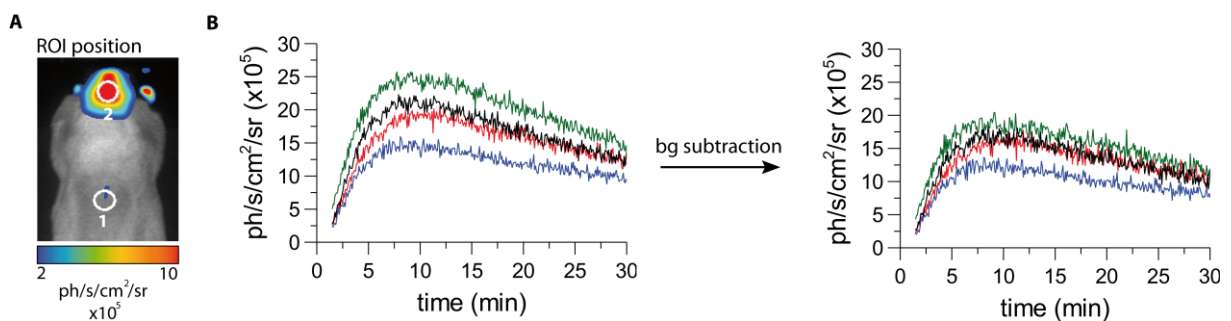


Figure 31: Background correction for the 4 DCX-Luc mice. A) BLI image of the ROI positions for measuring the background (ROI 1) and brain signal (ROI 2). B) The kinetic values obtained in ROI 1 were subtracted from ROI 2 for every animal (indicated by different colors) to normalize for variations in substrate injection/delivery in each imaging session.

Photon flux dependence on substrate concentration

In order to measure the substrate-dose dependency of in vivo luciferase activity in DCX-Luc mice, different concentrations of D-Luciferin (15, 150, 300, 750 mg/kg) were injected ip after 2% Isoflurane anesthesia and BL was recorded for 30 min. The D-Luciferin concentration had a significant effect on PE_{max} ($F(1.006, 3.017)=72.862$ $p=0.003$), AUC ($F(1.005, 3.016)=66.988$ $p=0.004$) and time-to-peak ($F(3, 9)=28.693$, $p<0.001$). Interestingly, the increase in PE_{max} followed a monoexponential curve (Figure 32 A). The concentration increase from 150 mg/kg to 750 mg/kg resulted in approx. the 10-fold PE_{max}/AUC value (Figure 32 B). Nevertheless, at high concentrations the standard deviation was also increased. The strong signal enhancement was accompanied by higher slope values in the initial inflow phase following also the exponential relationship (1.1×10^5 - 2.9×10^6) and a prolonged time-to-peak for high substrate concentrations (Figure 32 C, D).

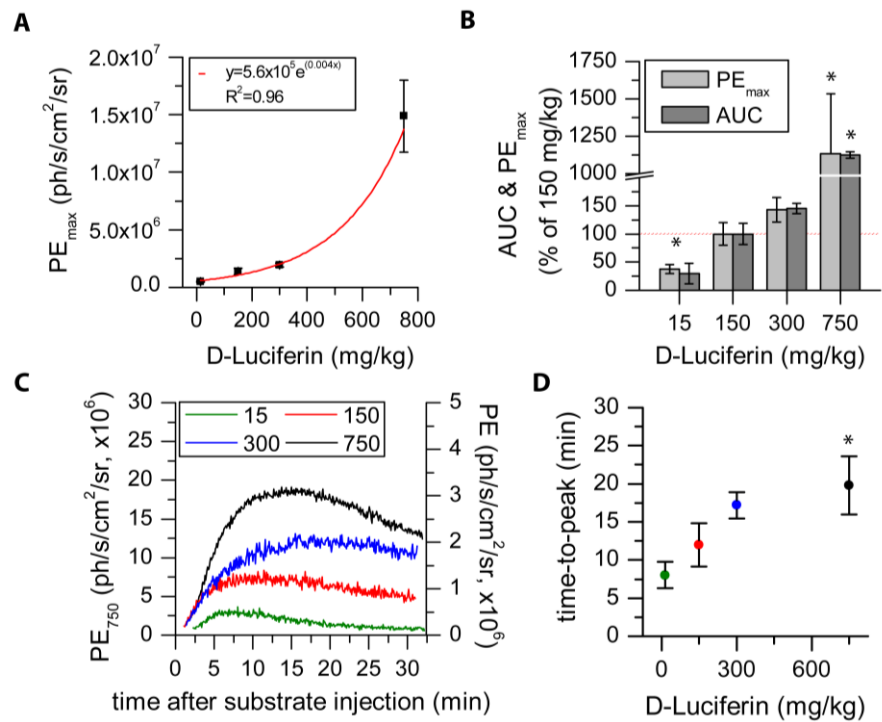


Figure 32: Dose-dependency of luciferase activity in DCX-Luc mice. **A)** Exponential PE_{max} increase for substrate concentrations 15-750 mg/kg. **B)** Illustration of AUC and PE_{max} values normalized to 150 mg/kg D-Luciferin (red dotted line). **C)** D-Luciferin concentration dependent modulation of luciferase time activity curves acquired for 30 min (left y-axis for 750 mg/kg, right y-axis for 15-300 mg/kg). **D)** The increased substrate concentration delays time-to-peak (* indicates statistically significant difference with $p \leq 0.05$ to 150 mg/kg in post-hoc comparison).

D-Luciferin injection route comparison

Here, the impact of different injection routes ip (intraperitoneal), vs. intravenous (iv) and subcutaneous (sc) was evaluated. DCX-Luc mice ($n=4$) received 150 mg/kg D-Luciferin ip, iv, or sc post Isoflurane anesthesia followed by acquisition for 30 min. Considering ip as the standard injection route, iv and sc had a significant effect on PE_{max} ($F(2, 6)=75.048$ $p<0.001$), AUC ($F(2, 6)=126.935$ $p<0.001$) and on time-to-peak ($F(2, 6)=71.148$ $p<0.001$). The PE_{max} for sc injections reached approx. 40 % of the ip

experiment, whereas iv resulted in approx. 450% PE_{max} . The AUC values showed a similar behavior with a minor effect for iv - approx. 260% (Figure 33 A). The D-Luciferin absorption kinetic was reflected by the luciferase time-activity curves with a smaller slope for sc vs. ip ($6.1 \times 10^4 \pm 2.2 \times 10^3$ vs. $2.2 \times 10^5 \pm 8.6 \times 10^3$). In case of iv injections, absorption into the blood system is not the rate-limiting step, as reflected by the highest slope ($5.1 \times 10^5 \pm 6.2 \times 10^4$) (Figure 33 B). The D-Luciferin biodistribution contributed to significant smaller time-to-peak values for iv injections (8.7 min shorter than ip, $p=0.017$) and a significant delay in time-to-peak for sc (additional 4.4 min compared to ip, $p=0.011$) (Figure 33 C).

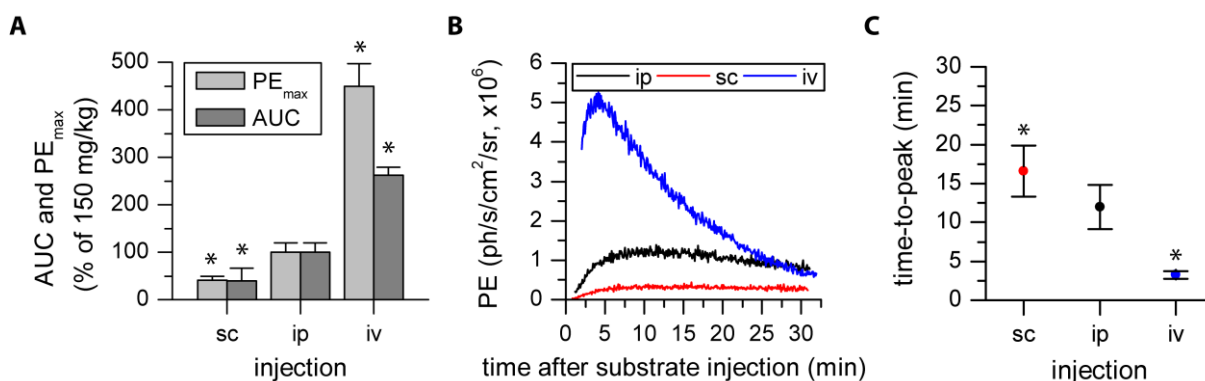


Figure 33: Brain-specific BLI is strongly affected by the D-Luciferin injection route. A) Compared to ip injections, PE_{max} and AUC were significantly reduced for sc and enhanced for iv injections. **B)** Kinetic of D-Luciferin biodistribution is reflected by the time-activity-curves. **C)** This results in significantly longer time-to-peak values for sc (red) and faster signal maturation for iv (blue) injections compared to ip (* indicates statistically significant difference with $p \leq 0.05$ to 150 mg/kg ip in post-hoc comparison).

Effect of anesthesia on photon flux

In a further set of experiments, the impact of type and timing of anesthesia was evaluated. Beside the commonly used Isoflurane anesthesia, which was reported to exhibit inhibitory effects on the luciferase enzyme, Pentobarbital and Ketamine/Xylazine were compared. The 4 DCX-Luc mice received different concentrations of D-Luciferin ip (15, 150 and 300 mg/kg) prior to and post Isoflurane anesthesia in order to determine the influence of a pre-inhibited enzyme. D-Luciferin injection prior to Isoflurane anesthesia resulted in significantly increased PE_{max} ($F(1, 3)=51.585$ $p=0.006$) and AUC ($F(1, 3)=44.488$ $p=0.007$).

By increasing the substrate concentration the maximum and total amount of photon flux difference for pre to post condition was significantly increased (300 mg/kg to 150 mg/kg pre iso: PE_{max} $p=0.01$, AUC $p=0.009$) (Figure 34 A, B). The time-to-peak suggested a similar D-Luciferin concentration-dependent effect, however did not reach the level of statistical significance (Figure 34 C).

In a second set of experiments, DCX-Luc signal was compared for different anesthetics revealing an overall effect on PE_{max} ($F(2, 6)=5.935$ $p=0.038$) but no significant change compared to Isoflurane anesthesia in post-hoc pairwise comparison (Ketamine/Xylazine: $p=0.058$, Pentobarbital: $p=0.742$). A

significantly lower AUC value for Ketamine/Xylazine compared to Isoflurane ($F(2, 6)=22.738$ $p=0.002$; post-hoc $p=0.005$) (Figure 35) was observed. Time-to-peak values for Isoflurane and Pentobarbital were not different.

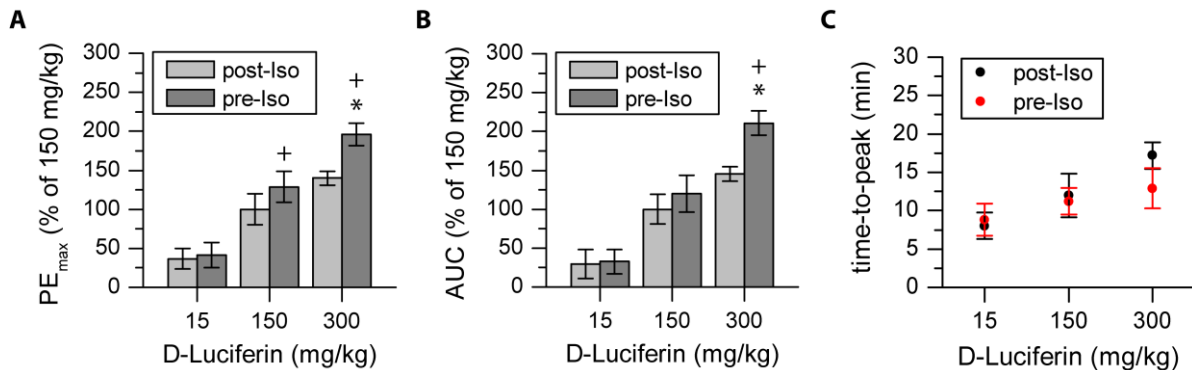


Figure 34: Luciferase inhibition by Isoflurane is D-Luciferin dose-dependent. A and B) PE_{max} and AUC differed were increased for the pre Isoflurane condition. This effect could be increased by higher substrate concentrations (*=statistically significant to 150 mg/kg post-Iso, +=statistically significant between pre and post condition, $p \leq 0.05$). C) There was no effect on the time-to-peak value.

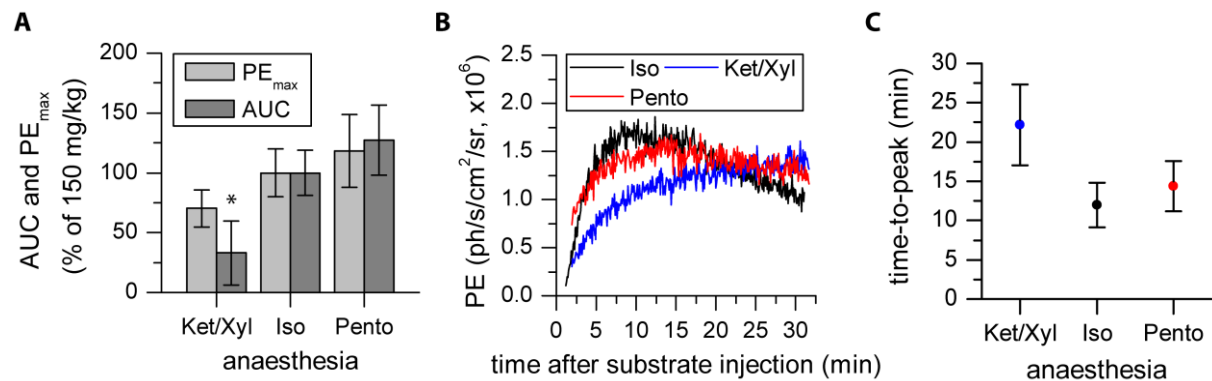


Figure 35: DCX-Luc BLI is modulated by the type of anesthesia. A) PE_{max} and AUC were slightly decreased under Ketamine/Xylazine conditions and increased under Pentobarbital anesthesia, without reaching statistical significance (except for AUC Ketamine/Xylazine compared to 150 mg/kg post-Iso, $p=0.005$, indicated by *). B and C) Representative time activity curves showing the anesthesia dependent signal behavior leading to delayed time-to-peak for Ketamine/Xylazine, but no difference for Isoflurane to Pentobarbital anesthesia.

4.2.6 Generation of advanced Luc2+ NSCs

The first generation of D3WT_N2Euro cells was transduced using a lentiviral approach. In order to generate advanced luciferase expressing cells, the Luc2-T2A-copGFP cassette was cloned into a retroviral vector, which included the internal LTR promoter and the neomycin resistance cassette, driven by an additional SV40 promoter (Figure 36 A). This enabled a double selection strategy – by the copGFP expression and the antibiotic resistance – resulting in approx. 90% transduced cells which were subsequently selected. Initially a FACS high ($>10^3$ counts) and middle (5×10^2 - 10^3 counts) cell line was derived in order to determine the impact of high gene reporter expression (Figure 36 B, C). There was a significant reduced viability detectable for the high vs. middle copGFP expressing cells (Figure 36D).

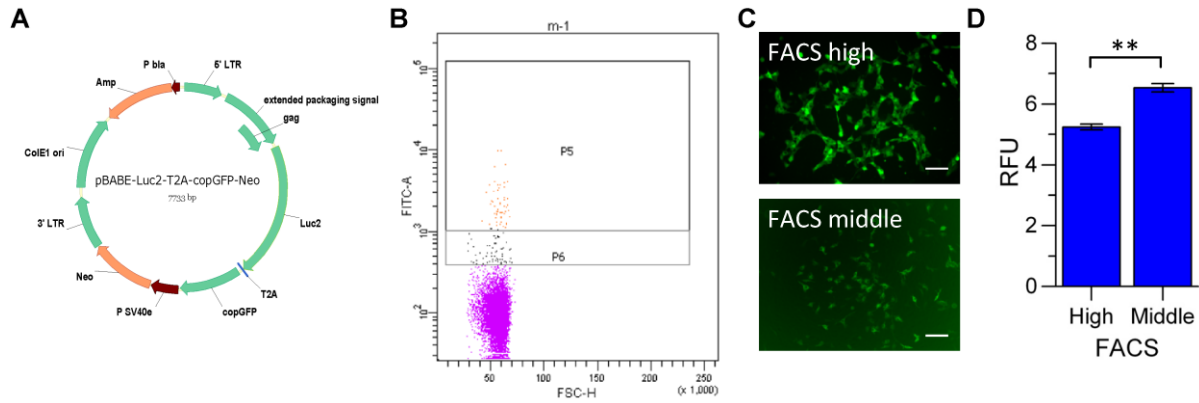


Figure 36: Retroviral generation of NSCs expressing Luc2 and copGFP. A) Retroviral plasmid used for transduction contains Luc2 coupled to copGFP and Neomycin resistance driven by the SV40 promoter. B) Transduced cells were sorted for a middle (P6) and high count regime (P5) for copGFP. C) Representative fluorescence images of the sorted cell lines (20x magnification, scale bar 50 μm). C) Cell viability was significantly decreased for the FACS high cells ($p < 0.005$), for differences in cell viability with the PrestoBlue assay.

However, the FACS high cell line dominated strongly in BLI performance (7 vs. 2 photons/cell). In order to gain maximal sensitivity, the high cell line was chosen for further experiments. The cell numbers intended for transplantation and in vivo sensitivity determination were also tested in vitro. For this purpose, a cell dilution series (each cell number $n=4$) was measured

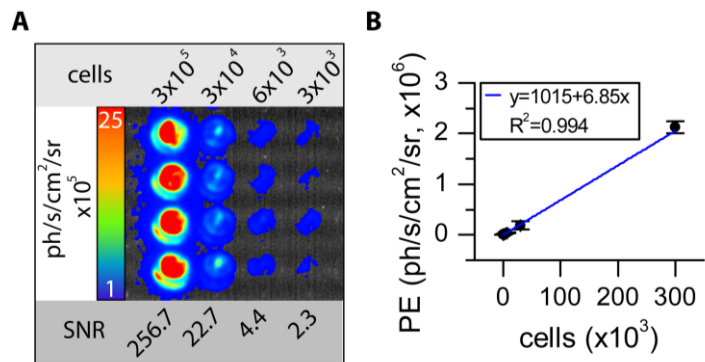


Figure 37: In vitro characterization of NSC bioluminescence. A) BL signal obtained for a cell dilution series ranging from 3,000 – 300,000 cells. B) Photon emission and cell number are linearly correlated as indicated by linear fit.

for 1 min under substrate excess conditions (1 mM) and the SNR was calculated (Figure 37 A). Under these conditions, the photon emission is linearly correlated with the amount of luciferase enzyme (represented by number of cells) (Figure 37 B) and results in a reliable detection of 6,000 cells with a mean SNR of 4.4.

The FACS high D3WT_N2Euro cells expressing Luc2 and copGFP were further characterized in relation to the non-transduced cells by Western blot, RT-PCR and ICC. The immunoblotting proved the exclusive expression of the reporter gene Luc2 in the transduced cells. A alleviative effect on the Nestin expression was detected by 5 % (approximated only for a single experiment). Furthermore, an extensive qualitative comparison of gene expression between transduced cells and WT cells was carried out (Figure 38). According to the equal bands for WT and transduced cells, there was no difference in gene expression induced by the transgene expression (excluding weak detection of Synaptophysin in transduced cells).

As an additional prove of no contaminating pluripotent cells, tumorigenicity was assessed in vivo. Luc2-positive cells were transplanted into nude mice (n=2) and BLI was conducted over 1 month. According to the decrease in BLI signal, cell death occurs after transplantation. On day 27 after transplantation, BLI signal from the cell graft reached the skin background level. A long-term tumor formation was excluded by the histological staining, which showed no sign of tumor cell proliferation (Figure 39).

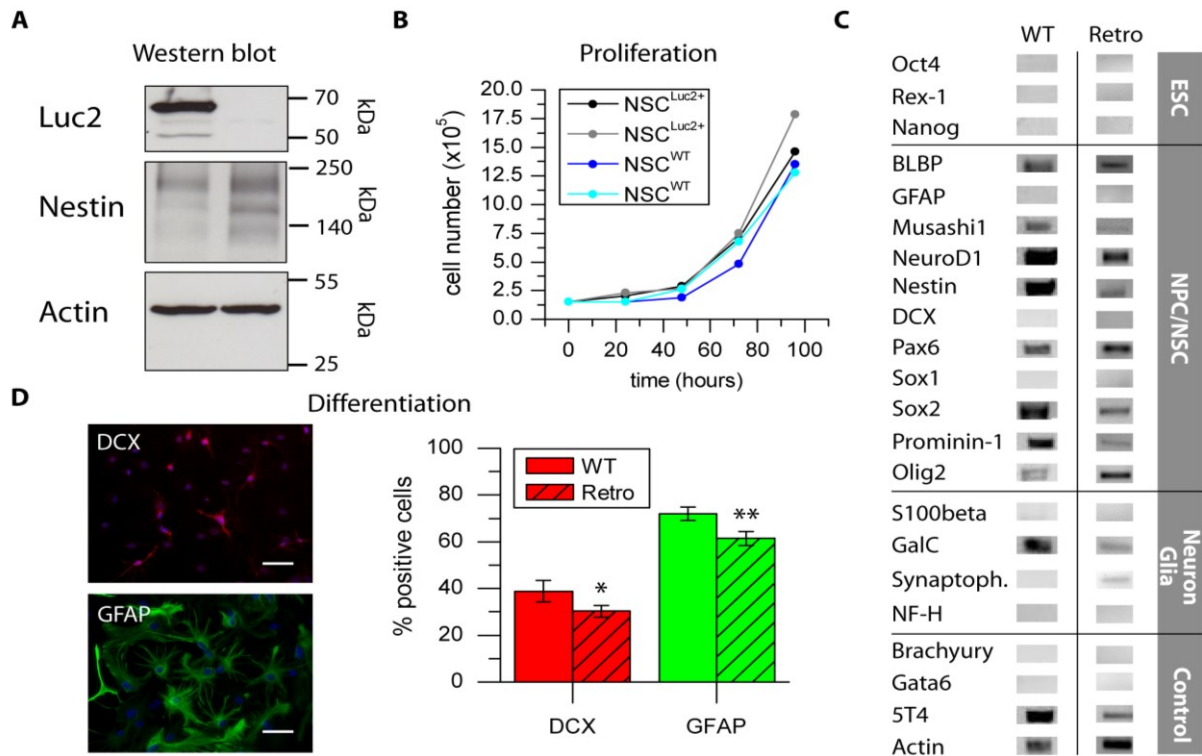


Figure 38: Characterization of D3WT_N2Euro cells transduced with EF1-Luc2-T2A-copGFP-SV40-Neo. A) Western blot verification of Luc2 (61 kDa) expression and maintained level of Nestin (200 kDa) compared to WT cells – Actin as loading control (42 kDa). B) Proliferation rate for Luc2-positive cells compared to WT obtained in two independent experiments. C) RT-PCR marker profile comparison for retroviral-vector transduced D3WT_N2Euro cells and WT cells. D) Neural differentiation potential of transduced cells differed significantly from WT cells (DCX p=0.006, GFAP p=0.001).

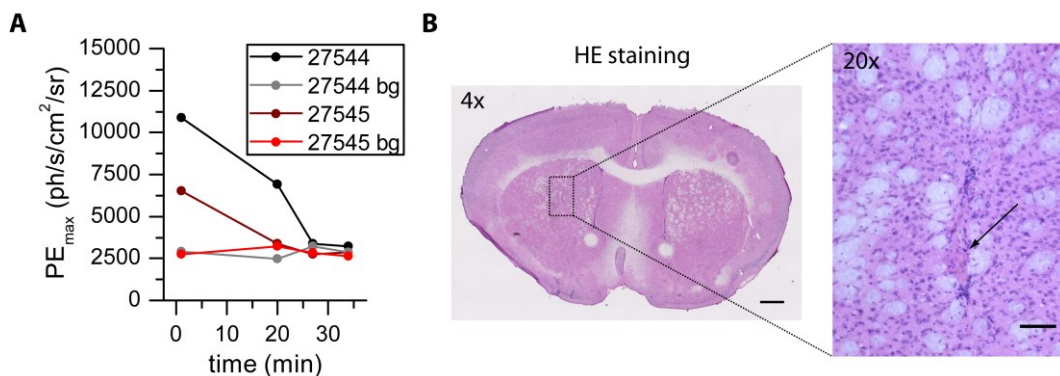


Figure 39: Long-term tracking of Luc2 expressing D3WT_N2Euro cells. A) Animal 27544 and 27545 received 30,000 cells into the left striatum and were monitored over 1 month. B) According to the homogenous cell structure visible in the H&E staining at 4x and 20x magnification, no tumor formation occurred (scale bar 500 and 50 μm).

4.2.7 Detection of small number of grafted NSCs with the advanced protocol

Based on the empirical data obtained in 4.2.5, 300 mg/kg pre Isoflurane anesthesia was chosen for a further in vivo application: the sensitivity determination for grafted NSCs. For this, different amounts of the Luc2 expressing D3WT_N2Euro cell line (see 4.2.6) were transplanted into the striatum of nude mice (3,000, 6,000, 30,000 or 300,000 cells, each cell amount n=3). BLI was performed 24 h later. The advanced protocol was applied in comparison to the standard protocol (150 mg/kg post Isoflurane and 300 mg/kg pre Isoflurane – 6 h time separation) for 30 min. The BLI detection limit was calculated assuming a SNR≥3 for a reliably detectable signal. A summary of all BLI images acquired under both protocol conditions

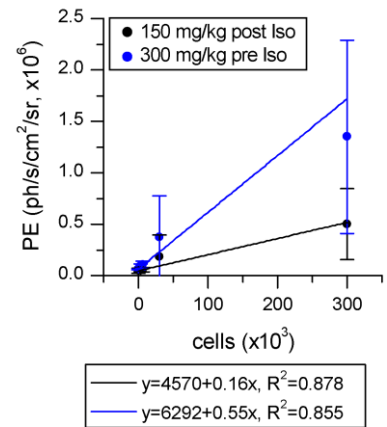


Figure 40: Linear correlation between photon emission and cell number for both BLI protocols.

is shown in Figure 41. This evaluation revealed the primarily the advantage of the new protocol, which facilitated the detection of 3,000 cells in vivo. The standard protocol required at least 30,000 cells to generate a SNR>3. Based on the calculated mean PE_{max} values for all cell grafts, a correlation between cell number and photon emission was plotted and fitted to a linear equation (Figure 40).

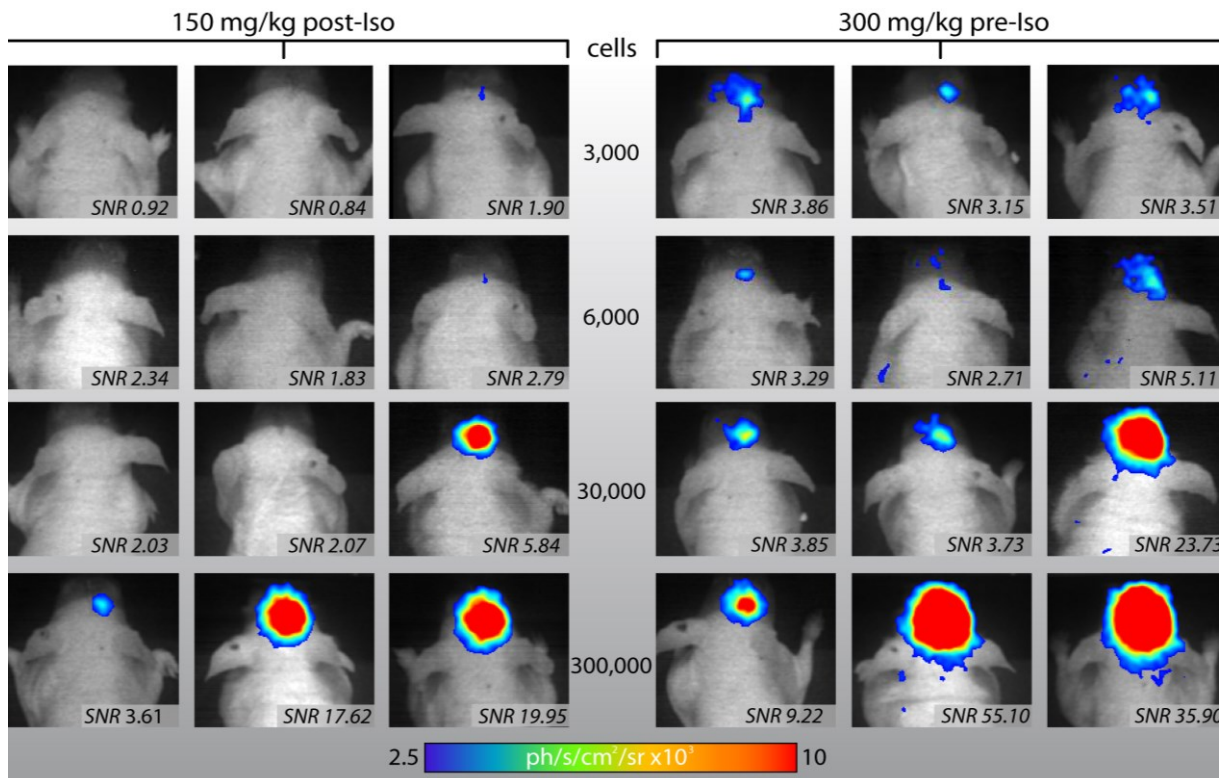


Figure 41: Sensitivity comparison of 150 mg/kg post-Iso and 300 mg/kg pre-Iso D-Luciferin injected ip. Based on the SNR calculations 3000 cells were reliably detectable with the advanced protocol, but at least 30,000 cells were necessary to generate a SNR > 3 acquired with the standard protocol.

4.3 Discussion

Optical cell tracking with bioluminescence enables researchers to observe various firefly, *Gaussia* and *Renilla* luciferases upon injection of the appropriate substrate without an additional light source. Luciferase variants were recently engineered to enable different emission spectra, to increase quality of emission and expression in mammalian cells by codon-optimization (see 1.3.2). These improvements paved the way for dual color⁷⁰ and dual substrate¹³⁸ imaging using different luciferases. Nevertheless, most of these luciferases have not been validated for neuroimaging approaches. Especially the quantitative detection limits cell grafts in the mouse brain missing. In the experiments of this dissertation, the genetically improved firefly Luc2, the red-shifted PpyRE9, the green-emitting Click beetle Luciferase CBG99 and the Coelenterazine-dependent *Renilla* luciferase hRluc were compared in terms of detectability under in vivo conditions. The results emphasize the impact of luciferase quantum yield superior to the wavelength-dependent tissue penetration. For dual color imaging based on different substrates, Luc2 coupled with hRluc are preferable and CBG99/PpyRE9 remain the best couple for spectral discrimination based on the different emission maxima. Based on the superior properties of Luc2 for neuroimaging purposes, the next experimental step involved the empirical optimization of imaging parameter with a transgenic mouse line for brain specific BLI. The advanced protocol proved two-times higher sensitivity for the detection of grafted Luc2-expressing NSCs.

4.3.1 Mouse neural stem cell line derived from embryonic stem cells

The mouse NSC line generated according to an adapted protocol (termed D3WT_N2Euro) fits precisely to the radial-glia like NSCs – a well described type of NSCs, obtainable under in vitro conditions¹³⁹. Nevertheless, the molecular fingerprint of such in vitro cells cannot directly be assigned to one of the NSCs characterized in the adult mammalian brain in vivo. Based on the expression of GFAP, NSCs in the SVZ are divided into GFAP-positive type B cells and transit-amplifying type C cells, which are GFAP-negative but positive for NG2 and Dlx-2^{140–142}. But the cellular correlate for D3WT_N2Euro cells is better represented by radial glia cells, which serve in the developing brain as neural progenitors and as scaffolds for migrating newborn neurons. The in vitro generation of radial glia cells seems to be a common step induced by the culture conditions¹⁴³. The radial glia-like NSC identity of D3WT_N2Euro cells is supported by the mouse radial glia set BLBP⁺/GFAP⁻¹⁴⁴ and the NSC pattern Nestin⁺/Pax6⁺/Sox1⁻/Sox2⁺/Musashi1⁺/Prominin-1^{+145–150}. In addition D3WT_N2Euro cells match the radial glia-like NSC pattern described by Conti *et al.*⁹³ (Sox1⁻/BLBP⁺/Pax6⁺/Olig2⁺/Musashi1⁺). The oligodendrogenic marker Olig2 and GalC (galactosylceramide)¹⁵¹ is explained by a phenotypic deregulation of cultured neural cells as reported by Dromard and colleagues¹⁶. The cerebellar immortalized NSC line C17.2 (initially derived from 4 day old mice), here used as a reference, showed a distinctive marker profile: GFAP⁺/Nestin⁺/Sox1⁻/Sox2⁺/Olig2⁻/GalC⁺. Previous reports have charac-

terized C17.2 accordingly, except for GFAP and Sox2, which were possibly acquired during extensive passaging (the cell line is already > 12 years old)¹⁰. However, C17.2 cells differ significantly from other NSCs, which limits the extrapolation from data acquired with C17.2 as Mi and colleagues pointed out¹⁵².

D3WT_N2Euro cells differentiate efficiently upon stimulation into the neuronal and glial lineage as it was proven by ICC and qPCR. In contrast to data by Conti *et al.*⁹³, expression of early neuronal marker (DCX) was more frequently (approx. 40% of all cells) than marker for mature neurons (e.g. Map2, Synaptophysin), according to the qPCR analysis. The efficient generation of betaIII tubulin-positive cells was not reached. Optimization of the protocol by hypoxia culture conditions (2% O₂), which can facilitate neuronal differentiation¹⁵³, could not improve the ICC results (data not shown). These results indicate that neuronal differentiation potential of D3WT_N2Euro cells is limited and would need further cell culture optimization. However, D3WT_N2Euro cells differentiate reliably into astrocytes (GFAP, Glast) and Oligodendrocytes.

In conclusion, the protocol described here, follows the model of embryonic stem cell differentiation as described by Pollard and colleagues¹³⁹, in which a transient Sox1-positive pan-neural progenitor population (analogous to mouse E8.5-10.5) contains mature Sox1-negative cells, which can be stably maintained and expanded using EGF plus b-FGF. As indicated by the absence of pluripotency marker (Oct4, Rex-1 and Nanog), D3WT_N2Euro cells lack residual embryonic stem cells, which could lead to a putative tumorigenicity after transplantation^{154,155}. By observing these cells over 4 weeks after transplantation into the striatum by BLI and histology, tumor formation or cell proliferation was excluded. The longterm passaging of D3WT_N2Euro cells revealed no differences in marker expression and differentiation potential as verified by RT-PCR and ICC. As an exception, weak amplification of Sox1 was detectable in the high passage, which would need further validation by qPCR to be verified as a sign of switch to neuroectodermal precursors¹⁵⁶. Nevertheless, D3WT_N2Euro cells meet the criteria of long-term, self-renewing and multipotent NSCs¹⁴³ as resource for further experiments.

4.3.2 Imaging reporter expression

Lentiviral vector-mediated imaging reporter expression in HEK-293 and D3WT_N2Euro cells

The cloning strategy for introducing the 4 different luciferases made use of the strong EF1 promoter, which was shown to be beneficial in terms of transgene stability especially in stem cells⁹⁰. Each luciferase was coupled to copGFP via the self-cleaving T2A sequence, which allows equimolar expression of both reporter genes and overcomes limitations of conventional linker elements like viral IRES elements (internal ribosomal entry site)¹⁵⁷. The transduction of HEK-293 and D3WT_N2Euro cells revealed the substantial difference in transduction efficiency and transgene integration/expression rate. Based on this observation, the HEK-293 cells were sorted using a higher FACS gate without long-

term proliferation effects. In contrast, NSCs represent a group of cells, which are much more difficult to transduce and are more vulnerable for genetic modification. Notably, NSCs required sorting with a lower gate to reveal stable, proliferating cell lines. The generally lower efficiency of gene delivery and suppression of exogenous genes integrated into the (embryonic) stem cell genome has been described^{158,159}. In a recent study by Dhara and colleagues¹⁶⁰, lentiviral transduction was compared with transfection and electroporation. Lentiviral transduction was found to be the most efficient method in terms of transgene expression and long-term GFP reporter expression in human neural progenitor cells. Because of the focus on the most efficient luciferase for *in vivo* neuroimaging applications, an extensive characterization of lentiviral-induced effects on (stem) cell behavior was not conducted. Nevertheless, various reports have proven the safety of lentiviral transduction especially for (neural) stem cells in terms of cell viability, proliferation, retained stem cell properties and no influence on the proteome^{160–162}.

Retroviral vector-mediated imaging reporter expression in D3WT_N2Euro cells

One drawback of the lentiviral approach is the size of the plasmids carrying the EF1 promoter and two reporter genes, which can exceed 10 kb – a critical size for efficient viral packaging. Therefore, D3WT_N2Euro cells were also infected by an ecotropic retrovirus, which contains Luc2-T2A-copGFP under control of LTR and Neomycin-resistance gene under control of a separate SV40 promoter (total size 7.7 kb). The antibiotic resistance in combination with the copGFP FACS revealed to be a highly efficient method to sort for stable cell clones with high reporter gene expression. Furthermore, these cells showed no difference in marker expression and differentiation potential. In these experiments the long-term stability of transgene expression was not as important but should be considered for future longitudinal studies. Retroviral vector systems are potentially hampered by transgene stability, which was reported to be stable for up to 3 months *in vivo* assessed by a LacZ expressing NSC transplanted into the mouse brain¹⁶³ and strongly reduced after differentiation¹⁶⁴.

4.3.3 Quantitative *in vitro* and *in vivo* luciferase comparison

Our neuroimaging experiments improve and complete previous reports comparing luciferases under *in vivo* conditions^{135,165,166}. Under *in vitro* conditions, the hRluc, Luc2 followed by CBG99 were superior to PpyRE9 luciferase with 10-times lower detectability for HEK-293 compared to NSCs. Under *in vivo* conditions, we detected a significant difference between CBG99 and Luc2 in line with the *in vitro* results (Table 21). However, the ratio between Luc2 and PpyRE9 decreased (3.7 ± 0.3 fold difference between Luc2 and PpyRE9 signals), indicating an advantage of the red shifted spectrum for *in vivo* imaging. Nevertheless, the spectral advantages were diminished by the low quantum yield, which leads to a benefit for the green-shifted CBG99.

Table 21: Quantitative comparison of luciferase performance in vitro and in vivo

Luciferase	In vitro	In vivo
	D3WT_N2	D3WT_N2Euro
Luc2	50	100,000
PpyRE9	500	300,000
CBG99	50	100,000
hRluc	50	>300,000

In contrast to the well-known flash-kinetic of *Renilla* luciferases in vitro, this BLI signal normalized to the luciferin kinetic with peak emissions between 12-16 min after substrate administration. Coelenterazine-h diffusion into the brain parenchyma is strictly limited by the multidrug-resistance specific transport back in the blood system, which is most probably the reason for the time delay in signal increase. In our experiments, only the pre-formulated Coelenterazine-h RediJect (Caliper) was a suitable *Renilla* substrate. Coelenterazine-h from different supplier could not be solved efficiently and degraded rapidly by spontaneous oxidation (leading to unspecific photon emission). This *Renilla*-specific setting enabled the detection of 6×10^4 HEK-293 in the brain, but not 3×10^5 NSCs. This discrimination is most prominent due to the fact that HEK-293 cells generated nearly 6 fold brighter signals in vitro. Optimization of hRluc expression in NSCs is therefore required for future studies.

The luciferase with second highest photon emission in vitro – Luc2 – was superior in vivo, which is in line with recent reports on liver imaging¹⁶⁷. The Luc2 benefits from the optical properties, but also from the extensive gene modifications to optimize its expression in mammalian cells¹⁶⁸. CBG99 revealed second highest photon emission in vivo and the most prominent spectral shift in relation to the transplantation depth, which can be used as a precise predictor.

Tissue depth-dependent spectral emission changes

Detection of BLI signals from brain transplantations is strictly dependent on the transmission properties of the brain tissue, determined mainly by light absorption due to hemoglobin^{52,169} and light scattering at myelin/cell borders^{53,170}. The spectral shift in relation to the transplantation depth was most prominent for the click beetle luciferase CBG99. In this case the emission maximum is directly shifted by the stronger absorption/scattering with increasing transplantation depth. Similar results were obtained by Zhao and colleagues¹⁷¹, who described depth-dependent spectral changes most prominent for the green-emitting click beetle luciferase CBG68. The emission of the red-shifted Luc2 and CBGr68 was diminished in the lung and liver but not the emission maximum. The pronounced shift in emission maximum for the experiments reported here could serve as a noninvasive control for the cell graft location for example in longitudinal studies in which migration of stem cells is assumed. In this case, spectral unmixing of the CBG99 signal would resolve the emission maximum, which could be translated to a certain transplantation depth.

Notably, dual color approaches with PpyRE9 and CBG99⁷⁰, would be hampered by the spectral shifts of CBG99 in the brain. Under in vitro conditions and if the cells are transplanted subcutaneously, the initial separation is 60 nm. This is diminished to 20 nm in case of 3 mm deep transplanted cell grafts in the mouse brain. In this respect novel Luc2 substrates for shifting the emission maximum of Luc2 about 40 nm could improve spectral unmixing¹⁷².

4.3.4 Revision of the standard protocol for bioluminescence neuroimaging

While conducting the BLI comparison of different luciferases, Keyaerts and colleagues³⁷ published an article about the anesthesia-dependent inhibition of the firefly luciferase. In a subcutaneous tumor model, the inhalation gas Isoflurane diminished the BLI signal about %. A publication record on 21 recent reports about BLI of transplanted (stem) cells and transgenic animals revealed the lack of a consistent standard protocol, with a tendency to 150 mg/kg D-Luciferin (62%) injected ip (86%), post anesthesia (57%) by Isoflurane (91%) (Table 22).

This protocol does not necessarily meet the special requirements of brain imaging, as it has been proven useful primarily in qualitative tumor studies. Therefore, in this study basic factors affecting the BLI in vivo were empirically evaluated for the first time on a mouse model for brain-specific BLI – the transgenic DCX Luc mice. The impact of substrate concentration, route/timing of substrate administration and the type of anesthesia were evaluated quantitatively. An advanced protocol was identified, which results in a 2-fold BLI signal increase, while remaining user-friendly, fast applicable and cost-effective. The advantage of the new protocol relies on the boosting of the sensitivity for optical cell tracking in the mouse brain by a factor of 2, which enabled for the first time the detection of down to 3,000 transplanted NSCs in vivo.

Concentration dependent increase in photon flux

The intracellular kinetics of firefly luciferase were recently characterized¹⁸⁶. Under in vitro conditions the intracellular half-life is over 24 hours and the K_M value (representing the concentration for half the maximal enzyme velocity) was found to be 1 mM. However, the in vivo situation – especially for brain specific BLI is not well characterized. Interestingly, the experiments with different concentrations showed that 750 mg/kg did still not result in a saturating photon emission level as it was proposed for 450 mg/kg D-Luciferin¹⁸⁷. Furthermore, the photon emission increased with concentration by an exponential curve. This effect is probably due to a critical blood plasma concentration, which facilitates substrate absorption through the blood brain-barrier¹⁸⁸. This is supported by the nearly 10-fold higher slope, which can serve as a measure for the substrate inflow dependent photon emission in the first 5 min of acquisition.

Table 22: List of BLI protocol conditions for recent publications from 2008-2012. Injection of D-Luciferin pre or post anesthesia, the type of anesthesia (Isoflurane – Iso, Ketamine/Xylazine – Ket/Xyl) and the injection route (ip, iv, sc) were compared. The D-Luciferin concentration for rats (*) was divided by a factor 5 to match the mouse weight.

Model	D-Luciferin (mg/kg)	pre or post anesthesia	Anesthesia	Injection route	Reference
Optimized protocol	300	Pre	Iso	ip	-
NSCs in a demyelination mouse model	300	pre	Iso	ip	173
Intracerebral glioblastoma	150	pre	Iso	ip	134
Cardiac cell transplant	75 (rats)*	pre	Iso	ip	174
GFAP-Luc transgenic mice	150	pre	Iso	ip	175
TLR2-Luc transgenic mice	150	pre	Iso	ip	176
Imaging SVZ-neurons with Luc lentivirus	126	post	Iso	ip	74
Human NSCs in ischemic rat brain	75 (rats)*	post	Iso	ip	177
Subcutaneous tumor model	150	post	Iso	ip	178
DCX-Luc transgenic mice	300	post	Iso	ip	71
Brain infiltration by MSCs	150	pre	Iso	ip	179
<i>Renilla</i> vs click beetle luciferase	150	post	Iso	ip	165
Brain infiltration by MSCs	150	post	Iso	ip	180
Subcutaneous tumor model	30	post	Iso	ip, iv	181
Luc2 vs PpyRE9	150	pre	Iso	ip	135
Subcutaneous tumor model	75	post	Iso	sc, ip	182
Intracerebral tumor model	125	pre	Iso	ip	183
Subcutaneous tumor model	150	post	Iso	ip	37
Brain infiltration by bone marrow cells	150	post	Ket/Xyl	ip	184
Intracerebral NSC model	150	pre	Iso	ip	185
Subcutaneous tumor model	150	post	Ket/Xyl	ip	70
Intracerebral MSCs graft	150	post	Iso	lv	136
	62 % 150	57% post	91 % Iso	86 % ip	

Assuming a 20 g mouse with 2 ml of total blood volume and neglecting substrate metabolism and elimination, the injection of 30 mg/kg D-Luciferin should reach already the in vitro K_M of 1 mM. Nevertheless, the D-Luciferin titration experiments revealed higher PE_{max} and contradict to previous assumptions, that the enzyme is already saturated at low substrate concentrations (5 μ l of 100 mM) for subcutaneous applications in vivo⁶⁸. Pharmacokinetic modeling as it was established for the tumor by Sim and colleagues¹⁸⁹ would be necessary to understand the brain-specific mechanisms of influx and efflux D-Luciferin kinetics. According to a calculation by Berger and colleagues¹⁹⁰ only 5% of the blood plasma level D-Luciferin will enter the brain parenchyma. The remarkable substrate restriction provides an indication of the persistent luciferase activity at substrate concentrations exceeding K_M under in vitro conditions. Interestingly, the time-to-peak is significantly delayed at high substrate concentrations. Under in vitro conditions, this would clearly be reflected in the conformational change of the luciferase enzyme, temporarily reducing the catalytic rate¹⁹¹. However, this observation is in all

probability due to the prolonged concentration gradient between blood plasma and brain tissue at high concentrations of D-Luciferin facilitating a continued concentration increase. D-Luciferin-dependent toxicity effects are not expected, as the majority of studies have reported no adverse effects^{68,192–195}.

Influence of injection route

D-Luciferin is advantageous as an imaging substrate because of its ability to distribute rapidly in the blood system, pass cell membranes and enter every organ (even through the placenta and blood brain-barrier)^{68,73,196}. In this study, previous reports for the injection route¹⁸² were complemented by comparing the impact of sc, ip and iv on the brain specific BL signal. For every condition, 4 DCX-Luc mice were injected with 150 mg/kg D-Luciferin and BLI was acquired in list mode for superior temporal resolution. In accordance with previous reports using a subcutaneous tumor model, also the brain signal was dependent on the D-Luciferin biodistribution^{181,182}. In case of the absorption-independent iv injection, the photon emission reached 400% maximum in ¼ the time compared to the ip injection. In contrast, after ip injection the substrate bioavailability is delayed by the absorption process from the peritoneum into the blood system, which finally reduces PE_{max} while prolonging time-to-peak. In contrast to a study of Inoue *et al.*¹⁸² the sc injection resulted in the lowest photon emission accompanied by a small slope and long time-to-peak value. In conclusion, iv injection generates the highest photon flux, but has limitations for repetitive measurements. The very fast kinetics without a long plateau phase for imaging impede reproducible measurements at the PE_{max} and can induce additional error. Tail vein injections require more experimental skills than the simple ip injections and repetitive injections into the same tail can induce tissue necrosis. Therefore, at this experimental stage, it was decided to use the ip injection, which is established and proven to work with a high success rate¹⁸² in a shorter time (more mice can be measured at the same time), repetitively without tissue irritation and permits experimental flexibility by a prolonged steady-state BLI signal.

Anesthesia-dependent photon flux changes

In vivo BLI of subcutaneously transplanted cells was reported to be strongly affected by the type of anesthesia³⁷. In this work, the effect of different anesthetics (Isoflurane, Ketamine/Xylazine, Pentobarbital) and the timing of Isoflurane anesthesia on brain-specific BLI was investigated.

Compared to the standard protocol, PE_{max} decreased Ketamine/Xylazine and increased slightly for Pentobarbital anesthesia, without reaching statistical significance. In vitro, Keyearts *et al.*³⁷ found no direct inhibitory effect of Ketamine, Pentobarbital or Medetomidine (belonging to the same family of α_2 adrenoreceptor agonists like Xylazine). In conclusion, the signal modulation observed in experiments reported here, might be the result of an altered hemodynamic situation. D-Luciferin biodistribution¹⁹⁷ and the BLI signal are affected.

However, anesthetics can have different effects on the blood system¹⁹⁸. Isoflurane results in the slightest reduction of cardiac output, followed by Pentobarbital with medium reduction. The strongest impact on cardiac output is expected under Ketamine/Xylazine anesthesia, which induces hypotension, bradycardia and hypothermia^{199,200}. Although cerebral hemodynamics are autoregulated, the grading of the hemodynamic changes parallels our observation of delayed time-to-peak values for Pentobarbital and Ketamine/Xylazine anesthesia compared to Isoflurane.

The slight difference in PE_{max} between Pentobarbital and Isoflurane anesthesia might be due to the direct inhibitory effect of Isoflurane on the luciferase enzyme, which we studied by comparing pre vs. post Isoflurane anesthesia. D-Luciferin injection before anesthesia consistently resulted in higher PE_{max}/AUC compared to the standard post injection. It was previously suggested, that D-Luciferin inhibition by Isoflurane is a mixed style inhibition with competitive binding at the substrate pocket site as well as a non-competitive binding, which will change the structure of the enzymatic pocket¹⁹¹. In line with previous reports³⁷, inhibition is partially reversible by higher substrate concentrations, which is due to an increased K_M value. Our data indicates that pre Isoflurane administration of D-Luciferin results in a better substrate distribution and an increased substrate availability in the brain compared to post Isoflurane injection. This results in an increased enzyme-substrate complex under pre Isoflurane condition, which is less affected by the inhibitory activity by Isoflurane.

Imaging protocol-dependent in vivo detection limits

We performed a quantitative comparison of the advanced vs. the standard imaging protocol applied to Luc2+ NSC transplanted into the mouse brain at different quantities. With this approach it was possible to study the detection limits of both protocols: 3,000 and 6,000 cells were not detectable with the standard protocol. Measuring these animals with the advanced protocol enables clear detection of even 3,000 transplanted NSCs. To point out, such a small number of transplanted non-immortalized NSC has not been imaged in vivo, yet.

SNR values were calculated for each graft size and a $SNR \geq 3$ determined as a quantitative measure to reliably distinguish BLI signal from the noise. Visual comparison of all BLI images ($n=12$) confirmed that signals outside the cell graft exhibited $SNR < 3$ and were identified as noise. Cell number approximation, as it was shown under in vitro conditions²⁰¹, seems to be possible in vivo providing that experimental conditions remain constant. Notably, the SNR values are not dependent on the 30 min acquisition time, they do not differ, if calculated for 1 min acquisition at the time-to-peak for each animal (300 mg/kg 3,000 cells: 30 min $SNR=3.5 \pm 0.4$, 1 min $SNR=4.4 \pm 1.3$). However, calculating SNR values for the 30 min acquisition is more convenient, as it requires no preprocessing (like determination of time-to-peak and image frame extraction) and can serve as a rapid estimation for a successful transplantation experiment.

High variability between animals receiving equal cell amounts was primarily induced by the transplantation procedure. The number of cells is variable due to the error induced during cell counting, the injection and the transplantation depth. As it was pointed out before, the transplantation depth is one of the key determinants of photon flux as it controls the percentage of transmitted bioluminescence light¹⁸³.

4.4 Conclusion and Outlook

In this chapter, bioluminescence imaging was extensively revised for the optimal protocol conditions and type of luciferase suitable for highest sensitivity in optical cell tracking within the mouse brain. In contrast to the majority of previous studies, which applied BLI as a qualitative tool to assess the presence of the reporter gene according to e.g. tumor growth or cells infected by an intracerebral injection of virus – the reported advancements can be used to fully exploit the potential of quantifying the luciferase expression *in vivo*. The threshold determination adapted from MRI by determining SNR values represents a valuable tool to reliably distinguish background signal from cell grafts.

The differences in photon flux between HEK-293 and NSCs emphasize the importance of further molecular and cellular biological optimization. A prerequisite to induce even higher levels of reporter gene expression could be realized potentially by adaption of an optimized high-level expression cassette on retrovirus vectors²⁰². Nevertheless, preservation of stem cell properties and retained reporter expression remains a requirement for using these novel reporter cells in a therapeutic application, e.g. the treatment of neurodegenerative disease.

Based on the improvements reported here, bioluminescence neuroimaging will be not limited on a single luciferase readout. By further improving the BLI sensitivity with luciferases bioengineered for far-red light emission, the combination with the green CBG99 luciferase to distinguish different cell types will become possible also for brain applications. An example of luciferase substrate-dependent cell discrimination is explained in the following chapter.

5. NONINVASIVE IMAGING OF NEURAL STEM CELL DIFFERENTIATION

5.1 Project aim and experimental setup

In vitro differentiation of embryonic and neural stem cells serves as a powerful tool to elucidate the complex gene regulations involved while cells shift from a pluri- and multipotent state to a definitive mature cell type, e.g. neuronal or glial cells. The conventional approach to follow the underlying cascade of molecular events is the in vitro differentiation by definite culture conditions and the subsequent immunostaining at each time point for selected markers. This implies a great experimental complexity and the limitation of definite end time point images. For the in vivo condition – the tracking of stem cell fate after transplantation – histology is substantially limited by marker analysis for different animals in experimental subgroups for selected time points.

The aim of this project was to develop a lentiviral-based assay for bimodal reporter gene detection of NSC differentiation into the glial lineage, which can be transferred into the in vivo application.

The basic concept involves NSCs transduced to stably and constitutively express *Renilla* luciferase hRluc and the green fluorescent protein copGFP. These reporter genes are included for optical cell tracking independent of the differentiation state. To assess differentiation into the glial lineage, the GFAP promoter was selected to drive the expression of the firefly luciferase Luc2 and the red fluorescent protein mCherry. This set of reporter genes was inserted by two independent lentiviral vector-mediated gene transfers into D3WT_N2Euro cells: 1) EF1-hRluc-T2A-copGFP and 2) GFAP-Luc2-T2A-mCherry.

The onset of GFAP expression could be monitored by the reporter genes under control of the GFAP promoter in vitro. This setup is intended to allow for the first time dual-luciferase and dual-color readout of the cell differentiation state by expression of the appropriate imaging reporters. The differentiated GFAP-positive cells can be distinguished by hRluc bioluminescence and mCherry fluorescence.

The experimental schedule included the following subprojects:

- 1) *Generation of lentiviral, bimodal reporter plasmids for constitutive and cell-specific imaging*
- 2) *Validation of the human GFAP promoter for efficient reporter expression in a tumor cell line*
- 3) *Transduction of bimodal reporter plasmids into D3WT_N2Euro cells*
- 4) *Dual-reporter monitoring of glial differentiation in vitro*

5.2 Results

5.2.1 Validation of the GFAP promoter driven reporter gene expression

In a first set of experiments, the human GFAP promoter was validated for efficient reporter gene expression in different mammalian cells (U373, GL261, HEK-293T). An appropriate model cell line was chosen based on the GFAP expression, triggered by stimulation with 0.5, 1.5 or 5.0 mM valproic acid (VPA). After 1 day of VPA treatment cells were fixed and stained for GFAP. These ICC stainings revealed a strong increase in GFAP immunoreactivity only for the human glioblastoma cell line U373 cells but not for GL261 cells. No increased ICC signal was detected for HEK-293T, which have no endogenous GFAP expression and served as a control for the VPA effect on the ICC. The relative ICC signal normalized to the cell number for a representative fluorescence image increased by a factor of 20 for U373 cells supplemented with 5 mM VPA for 24 h (Figure 42).

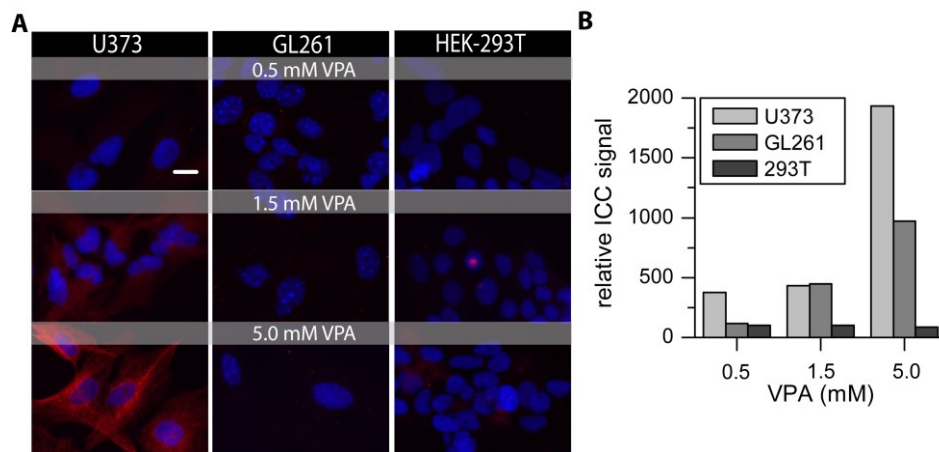


Figure 42: Validation of GFAP promoter activity. A) GFAP expression was triggered by 0.5, 1.5 and 5.0 mM valproic acid (VPA) in U373, GL261 and HEK-293T cells shown by increased immunoreactivity for the GFAP antibody stained by Cy3-coupled secondary antibody and counterstained with Hoechst (scale bar 25 μ m). B) Quantitative evaluation of the fluorescence in ICC stainings for GFAP normalized to the number of cells per ROI. U373 cells were most sensitive to the GFAP-inducing VPA treatment.

This paradigm was further tested by transfection of U373 with GFAP-T2A-copGFP, stimulation with 5 mM VPA for 1 day and subsequently GFAP staining. The representative fluorescence microscopy images in Figure 43 illustrate, how the copGFP fluorescence signal (no additional ICC necessary) was significantly increased by a factor of 1.7 ± 0.1 ($p=0.0032$). The increased expression of the GFAP-driven transgene was in accordance to the 1.8 ± 0.3 ($p=0.0300$) fold ICC signal obtained for endogenous GFAP.

Based on these experiments, the BLI performance of GFAP-driven Luc2 expression was studied. U373 were transfected with different plasmids: 1) EF1-Luc2-T2A-mCherry (control), 2) GFAP-Luc2-T2A-mCherry, 3) GFAP-Luc2-T2A-Puro and 4) GFAP-Luc2-P2A-mCherry-T2A-Puro. A longer VPA stimulation for up to 72 h was necessary to reveal reliable results. Cells were measured in black 96-wells to avoid cross-well signals. Upon VPA stimulation BLI was acquired for 1 min directly after addition of 1

mM D-Luciferin. For each condition, a quantitative ROI analysis was evaluated on at least 5 independent wells for each transfection. Figure 43 C summarizes the photon flux differences upon VPA stimulation normalized to the untreated samples set to 100%. The VPA stimulation had no effect on the conditionally expressed Luc2. In contrast, VPA stimulated GFAP-driven expression of Luc2 significantly for GFAP-Luc2-T2A-Puro ($p=0.0292$) and GFAP-Luc2-P2A-mCherry-T2A-Puro ($p=0.0325$). For the GFAP-Luc2-T2A-mCherry transfected cells, the photon flux increase was not significant different from the untreated group. A substantial difference in photon flux was detectable for the constitutive EF1 promoter ($27,956 \pm 8,065$ ph/s/cm²/sr) in relation to e.g. GFAP-Luc2-T2A-Puro ($14,883 \pm 4,329$ ph/s/cm²/sr).

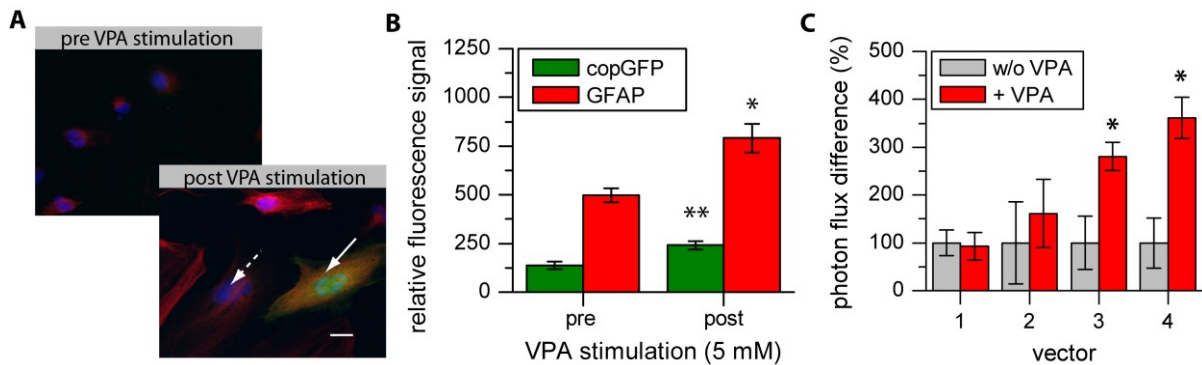


Figure 43: GFAP-induced expression of imaging reporters after stimulation of U373 with VPA. A) Representative fluorescence microscopy of GFAP ICC (red). U373 were transfected with GFAP-T2A-copGFP and stimulated for 24 h with VPA. In a subset of cells copGFP expression was initiated along with GFAP (arrow), whereas in other cells only GFAP was upregulated (dotted arrow) (Hoechst nuclei staining, 40x magnification, 25 μ m scale bar). B) Quantification of relative fluorescence signals for copGFP and ICC of GFAP pre and post VPA stimulation for 24 h. C) BLI of VPA-dependent GFAP promoter activation in U373 transfected with different GFAP vectors: 1) EF1-Luc2-T2A-mCherry, 2) GFAP-Luc2-T2A-mCherry, 3) GFAP-Luc2-T2A-Puro, 4) GFAP-Luc2-P2A-mCherry-T2A-Puro. BLI data from wells without VPA-stimulation were used for normalization.

5.2.2 Dual reporter neural stem cells

In a first transduction experiment, D3WT_N2Euro cells were infected with a lentivirus carrying EF1-hRluc-T2A-copGFP or EF1-T2A-copGFP as control. The cells from two independent experiments were sorted according to the copGFP expression by applying different FACS gatings: for very high expressing cells $> 10^3$ counts, for high expressing cells $> 7 \times 10^2$ and middle expressing cells $5 \times 10^2 - 1 \times 10^3$ counts (Figure 44). These cells were further passaged and subsequently compared against WT cells and cells transduced with the control vector EF1-T2A-copGFP based on photon flux and cell viability (Figure 44 D). The cell viability was decreased only by the hRluc expressing cell lines with a significant stronger effect for the FACS High I cells ($p=0.0075$) compared to WT cells. As an exception, the High II cell line showed significantly higher cell viability compared to the WT cells ($p=0.0025$).

In accordance with the FACS gating, High II cells exhibited 2.2-fold photon flux and the High I cells even a 3.4x-fold higher photons/cell value. In order to achieve highest BLI sensitivity, the D3WT_N2Euro EF1-hRluc-copGFP High I cell line was chosen for the second transduction. This time,

the plasmid with a cell specific promoter-driven Luc2 expression was transduced. In order to follow the GFAP promoter onset by histology, the red fluorescent protein mCherry was coupled via the T2A peptide to Luc2. However, the second transduction resulted in an additional cell stress, which impeded the efficient gene integration. Therefore, the GFAP-Luc2-T2A-mCherry plasmid was expanded by an additional SV40 promoter for driving the expression of zeocin resistance. Thus, additional GFAP promoter independent selection for successfully transduced cells was possible, by media supplementation with 200 $\mu\text{g/ml}$ Zeocin. The resulting double transduced NSC line was used for the differentiation experiments.

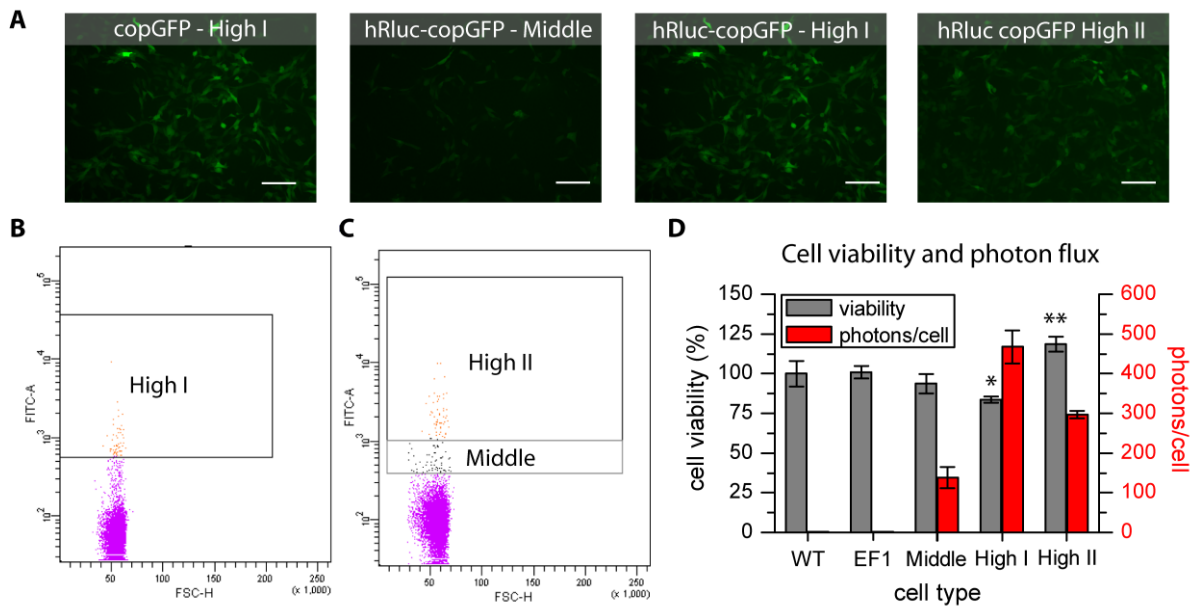


Figure 44: Generation of D3WT_N2Euro cells with high expression of hRluc and copGFP. A) Representative fluorescence images for the cell lines transduced with EF1-T2A-copGFP or EF1-hRluc-copGFP with different levels of copGFP expression. Two cell lines with high copGFP expression (High I, II) and one with less copGFP (Middle) were generated (20x magnification, scale bar 100 μm). B and C) Dot plots for the High I, High II and Middle cell line, named according to the FACS gate and copGFP fluorescence, respectively. D) These cell lines were tested by PrestoBlue assay for cell viability and by a BLI cell dilution series for the photon flux properties.

5.2.3 Dual reporter monitoring of glial differentiation

Double transduced D3WT_N2Euro cells were differentiated into the glial lineage according to the protocol described in section 4.2.1. The mCherry fluorescence onset was monitored after 7 days of differentiation. Figure 45 illustrates the differences between the undifferentiated, proliferative NSC state characterized by $\text{copGFP}^+/\text{mCherry}^-/\text{ICC-GFAP}^-$ and the glia cell culture after differentiation characterized by $\text{copGFP}^+/\text{mCherry}^+/\text{ICC-GFAP}^+$. After differentiation, GFAP-negative cells (dotted arrow) can be clearly distinguished from cells expressing GFAP (arrow). These cells co-express the optical reporter mCherry, visible without any histological treatment (Figure 45 B). A potential down-regulation of the constitutive copGFP reporter during differentiation was excluded by equal fluorescence measurements before and after differentiation (Figure 46 A).

The Luc2 expression under control of the GFAP promoter was monitored at 1, 4 and 7 days of glial differentiation in a 24-well plate (Figure 46 B). A significant increase was observed from day 1 to 4 ($p=0.048$), in which the Luc2 expression increased and resulted in approx. 24-fold increase of photon flux. Until day 7, the photon flux tended to increase, although without reaching significance.

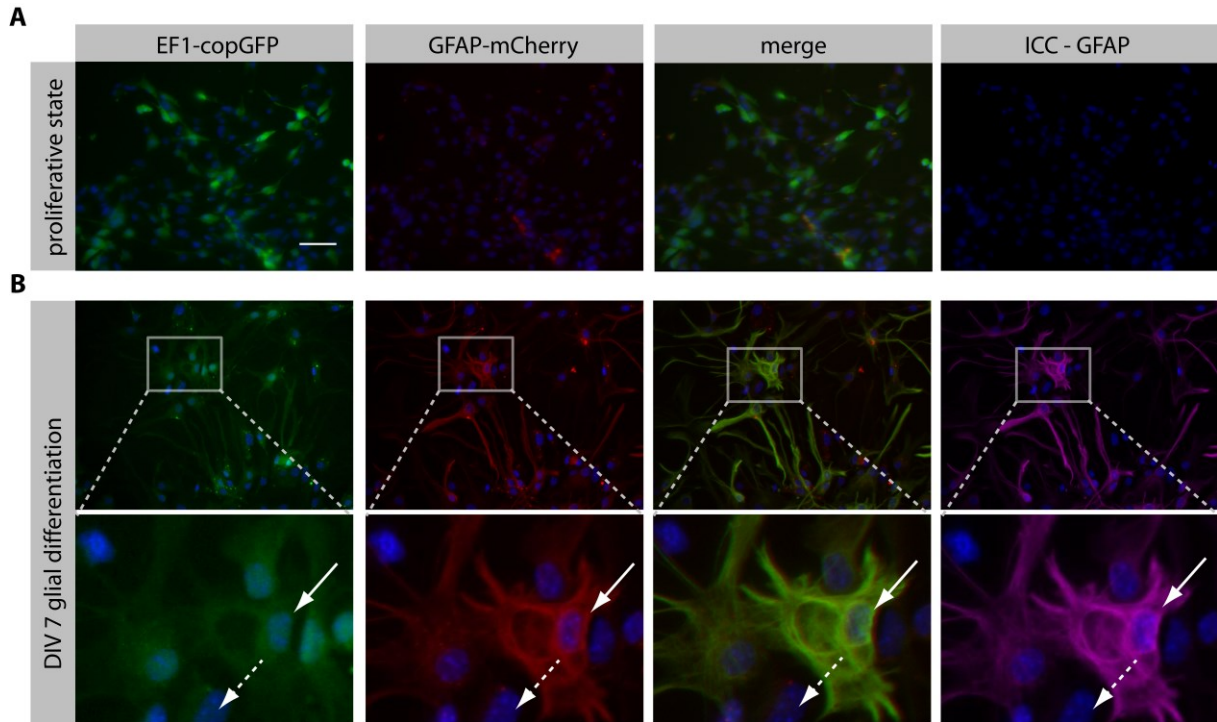


Figure 45: Monitoring glial differentiation by fluorescence reporter. Fluorescence microscopy images for the endogenous expression of copGFP (EF1 promoter-driven), mCherry (GFAP promoter-driven) and the ICC for GFAP for A) proliferative and B) differentiation conditions (Hoechst used for staining nuclei, all images 40x magnification, 50 μm scale bar).

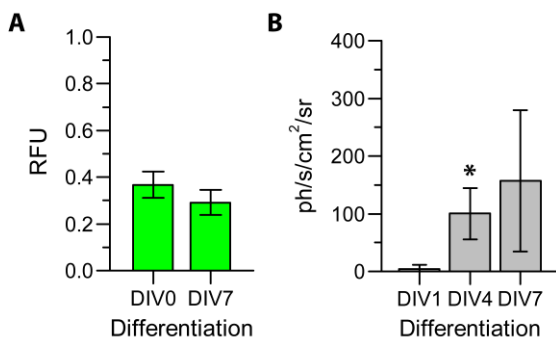


Figure 46: Fluorescence and bioluminescence reporter during glial differentiation. A) Differentiation induced changes in copGFP were not significant. B) The Luc2 photon flux increased during the glial differentiation specifically because of the GFAP promoter activity.

5.4 Discussion

Noninvasive monitoring of neural stem cell differentiation has not been achieved until now. One way to highlight the glial fate of NSCs is presented here: the expression of bimodal optical reporters under control of a differentiation sensitive promoter. The NSC line D3WT_N2Euro lacks GFAP expression in the proliferative state, but induces GFAP strongly upon glial differentiation. This endogenous off/on system was chosen for a molecular imaging approach. At first, the human GFAP promoter was tested in a tumor cell line for the efficient expression of optical imaging reporter. In a second step, D3WT_N2Euro cells were double transduced, which enabled 1) the constitutive, and 2) glia cell-specific promoter driven expression of distinct bioluminescence and fluorescence reporters. This approach enabled for the first time the visualization of the glial fate in living neural stem cells by imaging reporter with a potential for in vivo applications.

5.4.1 Validation of the GFAP promoter driven reporter gene expression

The intermediate filament protein GFAP was discovered 40 years ago²⁰³ during an analysis of multiple sclerosis plaques and found to be almost exclusively expressed in astrocytes. The well described cell specificity in neural cells has recommended the human²⁰⁴ and mouse²⁰⁵ GFAP promoter for directing transgene activity in astrocytes²⁰⁶. Applications included GFAP-targeting in brain tumors^{207–209}, astrocyte-specific production of bioactive molecules^{210,211} and creation of disease models^{212,213}. Morphological studies on transgenic mice using the bacterial beta-galactosidase or jellyfish GFP under control of the GFAP promoter have been described^{204,205}. More recently, Cho and colleagues²¹⁴ generated a dual transgenic mouse expressing firefly luciferase under control of the human GFAP promoter and *Renilla* luciferase under control of constitutive human GAPDH promoter.

In the experiments reported here, imaging reporter plasmids were cloned, which include not only the luciferases Luc2 and hRluc, but also 2 different fluorescent reporters with clear advantages. Firefly and *Renilla* luciferases do not require post-translational modification, which allows fast maturation of the functional enzyme providing immediate reporter readout upon promoter activation^{215,216}. Furthermore, the BLI signal from both luciferases can be separated by the choice of substrate – D-Luciferin or Coelenterazine. The fluorescent proteins copGFP and mCherry belong to a group of advanced bright reporters and can be separated by the fluorescence emission (502 nm vs. 610 nm). For the initial validation of the GFAP promoter plasmids, the human astrocytoma cell line U373 was selected. GFAP expression could be efficiently modulated by the mood-stabilizer valproic acid, which inhibits cell growth and induces differentiation¹⁰⁵. The short-term expression of GFAP-promoter driven imaging reporters was achieved by transfection. These experiments showed clearly the imaging reporter activation upon stimulation of GFAP expression in U373 cells. The initial cloning approach included GFAP plasmids with puromycin resistance genes for selection of cells after differentiation.

Transfection with these plasmids resulted in the strongest luciferase response, which suggests no interference of the plasmid size for the expression of the transgene directly downstream of the promoter. Nevertheless, in future studies mCherry fluorescence should be quantified dependent on the position in the reporter cassette.

5.4.2 Dual reporter neural stem cells provide monitoring of glial differentiation

As pointed out in the results section (5.2.2), double transduction of D3WT_N2Euro cells was not sufficient for every plasmid tested with U373 cells. For this reason, only the additional antibiotic selection through an independent SV40-promoter driven zeo gene enabled the efficient 2nd transduction. The final NSC line was transduced with EF1-hRLuc-T2A-copGFP and GFAP-Luc2-T2A-mCherry-SV40-Zeo. As indicated by the viability measurements (Figure 44), not the transduction process, but the presence of a bimodal reporter can alter cell viability. These cells were used to target glial differentiation by monitoring Luc2 and mCherry expression. The human GFAP promoter was sufficient to drive the expression of these reporter genes illustrated by the detection of fluorescence and bioluminescence in vitro. This way, glial cells were distinguished after differentiation by the coexpression of copGFP and mCherry from mCherry and GFAP negative cells. During the differentiation process, the constitutive copGFP signal decreased without reaching a significant difference between undifferentiated and differentiated cells. This stable reporter expression is one advantage of the lentiviral approach in relation to retroviral-mediated gene transfer and facilitates long-term observations¹⁶⁴. The luciferase signal was 45-fold increased during the differentiation process. The measurements of hRLuc signals could not be combined and used for normalization as initially planned. The substrate CTZ-h is premixed in an organic solvent, which lead to the detachment of cells during 1-2 minutes. The measurements could be combined by including additional control wells only for the hRLuc measurements. Nevertheless, the dual luciferase approach was hampered also by the weak GFAP promoter and would need further improvement for in vivo studies. As proposed by Leeuw and colleagues²¹⁷, the transcriptional activity of the GFAP promoter can be increased by inserting GFAP enhancer regions. Transfection experiments revealed a 75-fold higher LacZ expression upon plasmid transfection. Preliminary results with this gfa2(ABD)₃ promoter (data not shown), revealed a 5.6-fold higher Luc2 BLI signal in the U373 experimental model and serves as a basis for further optimization.

5.5 Conclusion and Outlook

In this study, cell specific optical imaging was shown in vitro. Imaging reporter plasmids were cloned, which contain a luciferase and fluorescence reporter for both, the undifferentiated and differentiated state of neural stem cells. This approach enables the discrimination of glial cells from neural stem cells by the imaging reporters, which are detectable in the living cell. No histological staining is necessary to assess the glial fate quantitatively, which overcomes conventional attempts to visualize the

fate of (transplanted) stem cells²¹⁸. A remaining challenge is to enhance the transcriptional activity of cell-specific promoters. One possibility is the combination of additional enhancer elements, as shown for the GFAP²¹⁹ and Synapsin²²⁰ promoter. Alternatively, a Cre/lox system could be used to drive expression of Cre under control of the GFAP promoter and subsequently cleavage of a stop cassette to facilitate imaging reporter expression²²¹.

Further sensitivity improvements for this dual reporter would allow the application to transplanted stem cells. This way, noninvasive imaging will be able to assess the fate of stem cells quantitatively and elucidate an additional key feature of stem cell therapy.

6. SYNOPSIS

Noninvasive imaging is dedicated to visualize endogenous processes in the living cell, without affecting the physiological state of the experimental animal. Stem cell therapy in neurodegenerative diseases would substantially benefit from such methods visualizing processes like cell viability and differentiation. During the last decade, magnetic resonance imaging (MRI) of contrast agent-labeled stem cells was established to locate the cells in the anatomical background and to observe migration processes noninvasively. The resulting images provide a high resolution projection of the labeled cells but provide no specific information about the cell status. Histological evaluation is still necessary after finishing the in vivo experiment to derive the fate of transplanted cells.

This dissertation describes a novel MRI-based approach to overcome the limitations of conventional contrast agents. A molecular probe was designed to respond selectively to the most important enzyme in GABAergic neurons – the glutamic acid decarboxylase (GAD). For the first time, a responsive contrast agent has been found which is selectively activated by a neuron-specific enzyme, and provides the discrimination of GABAergic neurons based on T_1 relaxation changes.

An optical noninvasive method was analyzed in a second project aiming at optimal conditions for bioluminescence imaging (BLI). Neural stem cells (NSCs) were transduced with Luciferases, which can be used for noninvasive assessment of cell viability and quantity. Luciferases from different species were compared and validated for highest sensitivity. In conclusion, the codon-optimized firefly luciferase Luc2 was superior for imaging NSC grafts in the mouse brain. Furthermore, a novel BLI protocol was developed for boosting BLI sensitivity by a factor of 2. Using this protocol the reliable detection of 3,000 transplanted NSCs has become possible for the first time.

Based on these BLI optimizations, the third project invented a novel approach for cell-specific imaging. Lentiviral plasmids were generated, which enable the constitutive and glia cell-specific expression of luciferases and fluorescence proteins. This system is based on the combination of 4 optical imaging reporters and allows the monitoring of glial differentiation in living cells.

The results of these 3 projects promote additional noninvasive insights into stem cell biology of transplanted cells in the mouse brain. Cell-specific MRI and BLI as presented here improve the noninvasive tools necessary for the understanding of cellular therapy. The use of transgene overexpression and non-approved contrast agents limits the direct transfer into a clinical therapy. However, this experimental setup can make unique predictions on stem cell fate and function, an indispensable knowledge for a safe clinical implementation.

7. LIST OF ABBREVIATIONS

AOAA	Aminooxyacetic acid
AP	Anteriorposterior
ATP	Adenosine triphosphate
AUC	Area under curve
BBS	BES-buffered saline
b-FGF	Basic fibroblast growth factor
BLI	Bioluminescence imaging
BLBP	Brain lipid-binding protein
BrdU	Bromodeoxyuridine
BSA	Bovine serum albumin
CBG	Click beetle green
CCD	Charge-coupled device
CT	X-ray computed tomography
DCX	Gene coding for doublecortin
DIV	Days in vitro
DMEM	Dulbecco's modified Eagle's medium
DNA	Deoxyribonucleic acid
DV	Dorsoventral
EC	Extinction coefficient
ECL	Enhanced Chemoluminescence
EF1	Elongation factor 1alpha
EGF	Epidermal growth factor
ES cell	Embryonic stem cell
FACS	Fluorescence-activated cell sorting
FCS	Fetal calf serum
FID	Free induction decay
FISP	Fast Imaging with Steady Precession
FLASH	Fast Low-Angle Shot
FLI	Fluorescence imaging
FLT	Fluorescence tomography
for	forward
FOV	Field of view
GABA	γ -Aminobutyric acid
GAD	Glutamic acid decarboxylase
Galc	Galactosylceramidase
GAPDH	Glyceraldehyde 3-phosphate dehydrogenase
Gata6	GATA binding protein 6
Gd(III)	Gadolinium ion
GE	Gradient echo
GFAP	Glial fibrillary acidic protein
GFP	Green fluorescent protein
HBSS	Hank's buffered salt solution
HEK	Human embryonic kidney

hRluc	Humanized <i>Renilla</i> luciferase
HRP	Horse radish peroxidase
HS	Horse serum
ICC	Immunocytochemistry
IHC	Immunohistochemistry
ip	Intraperitoneal
ITS	Supplement containing insulin, human transferrin, and selenous acid
iv	Intravenous
LIF	Leukemia inhibitory factor
Luc2	Codon-optimized firefly luciferase
LTR	Long terminal repeat
MAP2	Microtubule-associated protein 2
MCAO	Middle cerebral artery occlusion
MMLV	Moloney Murine Leukemia Virus
MRI	Magnetic resonance imaging
MSME	Multi-Slice Multi-Echo
NEAA	Non-essential amino acids
NF-H	Neurofilament heavy chain
NMDA	<i>N</i> -Methyl-D-aspartic
NMR	Nuclear magnetic resonance
NPC	Neural precursor cell
NSC	Neural stem cell
Oct4	Octamer binding transcription factor 4
Olig2	Oligodendrocyte transcription factor 2
Pax6	Paired box protein 6
PBS	Phosphate-buffered saline
PCR	Polymerase chain reaction
PE	Photon emission
PFA	Paraformaldehyde
PET	Positron emission tomography
PMSF	Phenylmethanesulfonylfluoride
PLP	Pyridoxal phosphate
POLA	Poly-L-ornithine/laminin
PpyRE9	mutant red-shifted firefly luciferase
P/S	Penicillin/streptomycin
QY	quantum yield
RARE	rapid acquisition
RES	Reticuloendothelial system
rev	reverse
RNA	Ribonucleic acid
ROI	Region of interest
RT	room temperature (20°C)
rtPA	Recombinant tissue plasminogen activator
S100b	S100 calcium binding protein B
sc	subcutaneous

SDS	Sodium dodecyl sulfate
SE	Subependymal zone
SGZ	Subgranular zone
SNR	signal-to-noise ratio
SPIO	Superparamagnetic iron oxide particle
SV-40	Simian-Virus 40
STAT3	Signal transducer and activator of transcription 3
TA	acquisition time
TE	Echo time
TI	Inversion time
TR	Repetition time
TBS	Tris-buffered saline
Tubb3	Gene encoding for tubulin beta-3 chain
VPA	Valproic acid
VSV-G	Glycoprotein of vesicular stomatitis virus
WT	Wild type

8. REFERENCES

1. Evans, M. J. & Kaufman, M. H. Establishment in culture of pluripotential cells from mouse embryos. *Nature* **292**, 154–156 (1981).
2. Martin, G. R. Isolation of a pluripotent cell line from early mouse embryos cultured in medium conditioned by teratocarcinoma stem cells. *Proceedings of the National Academy of Sciences of the United States of America* **78**, 7634–7638 (1981).
3. Spangrude, G. J., Heimfeld, S. & Weissman, I. L. Purification and characterization of mouse hematopoietic stem cells. *Science* **241**, 58–62 (1988).
4. Taylor, G., Lehrer, M. S., Jensen, P. J., Sun, T. T. & Lavker, R. M. Involvement of follicular stem cells in forming not only the follicle but also the epidermis. *Cell* **102**, 451–61 (2000).
5. Zuk, P. A. *et al.* Multilineage cells from human adipose tissue: implications for cell-based therapies. *Tissue Engineering* **7**, 211–28 (2001).
6. Gross, C. G. Neurogenesis in the adult brain: death of a dogma. *Nature Reviews Neuroscience* **1**, 67–73 (2000).
7. Eriksson, P. S. *et al.* Neurogenesis in the adult human hippocampus. *Nature Medicine* **4**, 1313–1317 (1998).
8. Reynolds, B. A. & Weiss, S. Generation of neurons and astrocytes from isolated cells of the adult mammalian central nervous system. *Science* **255**, 1707–10 (1992).
9. Kallur, T. Human Neural Stem Cells: region-specific properties an prospects for cell therapy. 1–156 (2008).
10. Ryder, E. F., Snyder, E. Y. & Cepko, C. L. Establishment and characterization of multipotent neural cell lines using retrovirus vector-mediated oncogene transfer. *Journal of neurobiology* **21**, 356–75 (1990).
11. Kim, S. U. *et al.* Production and characterization of immortal human neural stem cell line with multipotent differentiation property. *Methods In Molecular Biology Clifton Nj* **438**, 103–121 (2008).
12. Alvarez-Buylla, A. & Garcia-Verdugo, J. M. Neurogenesis in adult subventricular zone. *Journal of Neuroscience* **22**, 629–634 (2002).
13. Morshead, C. M. *et al.* Neural stem cells in the adult mammalian forebrain: a relatively quiescent subpopulation of subependymal cells. *Neuron* **13**, 1071–1082 (1994).
14. Cameron, H., Woolley, C., McEwen, B. & Gould, E. Differentiation of newly born neurons and glia in the dentate gyrus of the adult rat. *Neuroscience* **56**, 337–344 (1993).
15. Doetsch, F. The glial identity of neural stem cells. *Nature neuroscience* **6**, 1127–34 (2003).
16. Dromard, C. *et al.* NG2 and Olig2 expression provides evidence for phenotypic deregulation of cultured central nervous system and peripheral nervous system neural precursor cells. *Stem Cells* **25**, 340–353 (2007).
17. Shagin, D. A. *et al.* GFP-like proteins as ubiquitous metazoan superfamily: evolution of functional features and structural complexity. *Molecular Biology and Evolution* **21**, 841–850 (2004).
18. Einstein, O. *et al.* Intraventricular transplantation of neural precursor cell spheres attenuates acute experimental allergic encephalomyelitis. *Molecular And Cellular Neurosciences* **24**, 1074–1082 (2003).
19. Lindvall, O. & Kokaia, Z. Stem cells for the treatment of neurological disorders. *Nature* **441**, 1094–6 (2006).
20. Einstein, O. & Ben-Hur, T. The changing face of neural stem cell therapy in neurologic diseases. *Archives of neurology* **65**, 452–6 (2008).
21. Li, J., Imitola, J., Snyder, E. Y. & Sidman, R. L. Neural stem cells rescue nervous purkinje neurons by restoring molecular homeostasis of tissue plasminogen activator and downstream targets. *Journal of Neuroscience* **26**, 7839–7848 (2006).

22. Kamei, N. *et al.* BDNF, NT-3, and NGF released from transplanted neural progenitor cells promote corticospinal axon growth in organotypic cocultures. *Spine* **32**, 1272–1278 (2007).
23. Mathers, C. D., Boerma, T. & Ma Fat, D. Global and regional causes of death. *British medical bulletin* **92**, 7–32 (2009).
24. Roger, V. L. *et al.* Heart disease and stroke statistics--2011 update: a report from the American Heart Association. *Circulation* **123**, e18–e209 (2011).
25. Davis, S. M. & Donnan, G. A. 4.5 hours: the new time window for tissue plasminogen activator in stroke. *Stroke: A Journal of Cerebral Circulation* **40**, 2266–2267 (2009).
26. Traystman, R. J. Animal models of focal and global cerebral ischemia. *ILAR journal / National Research Council, Institute of Laboratory Animal Resources* **44**, 85–95 (2003).
27. Locatelli, F. *et al.* Stem cell therapy in stroke. *Cellular and molecular life sciences : CMLS* **66**, 757–72 (2009).
28. Bliss, T., Guzman, R., Daadi, M. & Steinberg, G. K. Cell transplantation therapy for stroke. *Stroke; a journal of cerebral circulation* **38**, 817–26 (2007).
29. Oki, K. *et al.* Human Induced Pluripotent Stem Cells form Functional Neurons and Improve Recovery After Grafting in Stroke-Damaged Brain. *Stem cells Dayton Ohio* (2012).doi:10.1002/stem.1104
30. Wilhelmj, E. *et al.* Organotypic brain-slice cultures from adult rats: approaches for a prolonged culture time. *Alternatives to laboratory animals ATLA* **30**, 275–283 (2002).
31. Massoud, T. F. & Gambhir, S. S. Molecular imaging in living subjects: seeing fundamental biological processes in a new light. *Genes & development* **17**, 545–80 (2003).
32. Lauterbur, P. C. Image Formation by Induced Local Interactions Examples Employing Nuclear Magnetic Resonance lauterbur nature1973.pdf. *Nature* **242**, 190–191 (1973).
33. Journals, C., Contact, A., Iopscience, M., Phys, S. S. & Address, I. P. Image formation in NMR by a selective irradiative pulse. *J Phys C* **457**, L457–L462 (1974).
34. de Graaf, R. A. *et al.* High magnetic field water and metabolite proton T1 and T2 relaxation in rat brain in vivo. *Magnetic resonance in medicine : official journal of the Society of Magnetic Resonance in Medicine / Society of Magnetic Resonance in Medicine* **56**, 386–94 (2006).
35. Bloch, F. Nuclear Induction. *Physical Review* **70**, 460–474 (1946).
36. Hoehn, M. *et al.* Cell tracking using magnetic resonance imaging. *The Journal of physiology* **584**, 25–30 (2007).
37. Keyaerts, M. *et al.* Inhibition of firefly luciferase by general anesthetics: effect on in vitro and in vivo bioluminescence imaging. *PLoS one* **7**, e30061 (2012).
38. Weinstein, J. S. *et al.* Superparamagnetic iron oxide nanoparticles: diagnostic magnetic resonance imaging and potential therapeutic applications in neurooncology and central nervous system inflammatory pathologies, a review. *Journal of cerebral blood flow and metabolism official journal of the International Society of Cerebral Blood Flow and Metabolism* **30**, 15–35 (2010).
39. Geraldes, C. F. G. C. & Laurent, S. Classification and basic properties of contrast agents for magnetic resonance imaging. *Contrast media & molecular imaging* **4**, 1–23 (2009).
40. Runge, V. M., Clanton, J. A., Lukehart, C. M., Partain, C. L. & James, A. E. Paramagnetic agents for contrast-enhanced NMR imaging: a review. *Ajr American Journal Of Roentgenology* **141**, 1209–1215 (1983).
41. Allen, M. J. & Meade, T. J. Magnetic resonance contrast agents for medical and molecular imaging. *Metal Ions In Biological Systems* **42**, 1–38 (2004).
42. Solomon, I. Relaxation Processes in a System of Two Spins. *Physical Review* **99**, 559–565 (1955).
43. Moats, R. A., Fraser, S. E. & Meade, T. J. A “smart” magnetic resonance imaging agent that reports on specific enzymic activity. *Angewandte Chemie Inter Ed Eng* **36**, 726–728 (1997).
44. Aime, S. *et al.* NOVEL PARAMAGNETIC MACROMOLECULAR COMPLEXES DERIVED FROM THE LINKAGE OF A MACROCYCLIC Gd(III) COMPLEX TO POLYAMINO ACIDS THROUGH A SQUARIC ACID MOIETY. *Bioconjugate Chemistry* **10**, 701 (1999).

45. Lowe, M. P. *et al.* pH-dependent modulation of relaxivity and luminescence in macrocyclic gadolinium and europium complexes based on reversible intramolecular sulfonamide ligation. *Journal of the American Chemical Society* **123**, 7601–7609 (2001).
46. Li, W.-H., Parigi, G., Fragai, M., Luchinat, C. & Meade, T. J. Mechanistic studies of a calcium-dependent MRI contrast agent. *Inorganic Chemistry* **41**, 4018–4024 (2002).
47. Aime, S., Fasano, M., Paoletti, S., Arnelli, A. & Ascenzi, P. NMR relaxometric investigation on human methemoglobin and fluoromethemoglobin. An improved quantitative in vitro assay of human methemoglobin. *Magnetic Resonance in Medicine* **33**, 827–831 (1995).
48. Burai, L., Tóth, E., Seibig, S., Scopelliti, R. & Merbach, A. E. Solution and solid-state characterization of Eu(II) chelates: a possible route towards redox responsive MRI contrast agents. *Chemistry (Weinheim an der Bergstrasse, Germany)* **6**, 3761–3770 (2000).
49. Ramos-Cabrer, P. & Hoehn, M. MRI Stem Cell Tracking for Therapy in Experimental Cerebral Ischemia. *Translational Stroke Research* **3**, 22–35 (2011).
50. Sutton, E. J., Henning, T. D., Pichler, B. J., Bremer, C. & Daldrup-Link, H. E. Cell tracking with optical imaging. *European radiology* **18**, 2021–32 (2008).
51. Shah, K. & Weissleder, R. Molecular optical imaging: applications leading to the development of present day therapeutics. *NeuroRx: the journal of the American Society for Experimental NeuroTherapeutics* **2**, 215–25 (2005).
52. Zee, P. Van Der Measurement and modelling of the optical properties of human tissue in the near infrared. *Medical Physics* 1–302 (1992).
53. Ross, K. F. A. *Phase contrast and interference microscopy for cell biologists*. (Edward Arnold: 1967). at <<http://books.google.de/books?id=DEZrAAAAMAAJ>>
54. Leenders, K. L. *et al.* Cerebral blood flow, blood volume and oxygen utilization. Normal values and effect of age. *Brain: A journal of neurology* **113 (Pt 1)**, 27–47 (1990).
55. Gheysens, O. & Mottaghy, F. M. Method of bioluminescence imaging for molecular imaging of physiological and pathological processes. *Methods (San Diego, Calif.)* **48**, 139–45 (2009).
56. Prah, S. Optical Absorption of Hemoglobin. at <<http://omlc.ogi.edu/spectra/hemoglobin/>>
57. Cheong, W. F., Prah, S. A. & Welch, A. J. A review of the optical properties of biological tissues. *IEEE Journal of Quantum Electronics* **26**, 2166–2185 (1990).
58. Sarna, T. & Swartz, H. A. The physical properties of melanins. *The Pigmentary System Physiology and Pathophysiology* 311–341 (2006). doi:10.1002/9780470987100.ch16
59. Pope, R. M. & Fry, E. S. Absorption spectrum (380–700 nm) of pure water. II. Integrating cavity measurements. *Applied Optics* **36**, 8710–8723 (1997).
60. Palmer, K. F. & Williams, D. Optical properties of water in the near infrared. *Journal of the Optical Society of America* **64**, 1107 (1974).
61. Shimomura, O., Johnson, F. H. & Saiga, Y. Extraction, purification and properties of aequorin, a bioluminescent protein from the luminous hydromedusa, *Aequorea*. *Journal Of Cellular And Comparative Physiology* **59**, 223–239 (1962).
62. Prasher, D. C., Eckenrode, V. K., Ward, W. W., Prendergast, F. G. & Cormier, M. J. Primary structure of the *Aequorea victoria* green-fluorescent protein. *Gene* **111**, 229–233 (1992).
63. Chalfie, M., Tu, Y., Euskirchen, G., Ward, W. W. & Prasher, D. C. Green fluorescent protein as a marker for gene expression. *Science* **263**, 1766–1767 (2007).
64. Chudakov, D. M., Matz, M. V., Lukyanov, S. & Lukyanov, K. A. Fluorescent Proteins and Their Applications in Imaging Living Cells and Tissues. *Physiological Reviews* **90**, 1103–1163 (2010).
65. Baird, G. S., Zacharias, D. A. & Tsien, R. Y. Biochemistry, mutagenesis, and oligomerization of DsRed, a red fluorescent protein from coral. *Proceedings of the National Academy of Sciences of the United States of America* **97**, 11984–11989 (2000).
66. Inoué, S. Firefly luciferase: an adenylate-forming enzyme for multicatalytic functions. *Cellular and molecular life sciences CMLS* **67**, 387–404 (2010).
67. Gould, S. J. & Subramani, S. Firefly luciferase as a tool in molecular and cell biology. *Analytical Biochemistry* **175**, 5–13 (1988).

68. Contag, C. H. *et al.* Visualizing Gene Expression in Living Mammals Using a Bioluminescent Reporter. *Photochemistry and Photobiology* **66**, 523–531 (1997).
69. Dohager, R. S. *et al.* Advances in bioluminescence imaging of live animal models. *Current opinion in biotechnology* **20**, 45–53 (2009).
70. Mezzanotte, L. *et al.* Sensitive dual color in vivo bioluminescence imaging using a new red codon optimized firefly luciferase and a green click beetle luciferase. *PLoS one* **6**, e19277 (2011).
71. Couillard-Despres, S. *et al.* In vivo optical imaging of neurogenesis: watching new neurons in the intact brain. *Molecular imaging* **7**, 28–34 (2008).
72. Edinger, M. *et al.* Noninvasive assessment of tumor cell proliferation in animal models. *Neoplasia (New York, N.Y.)* **1**, 303–10 (1999).
73. Rehemtulla, A. *et al.* Rapid and quantitative assessment of cancer treatment response using in vivo bioluminescence imaging. *Neoplasia (New York, N.Y.)* **2**, 491–5 (2000).
74. Reumers, V. *et al.* Noninvasive and quantitative monitoring of adult neuronal stem cell migration in mouse brain using bioluminescence imaging. *Stem cells (Dayton, Ohio)* **26**, 2382–90 (2008).
75. Keyaerts, M., Caveliers, V. & Lahoutte, T. Bioluminescence imaging: looking beyond the light. *Trends in molecular medicine* **18**, 164–72 (2012).
76. de Wet, J. R., Wood, K. V., DeLuca, M., Helinski, D. R. & Subramani, S. Firefly Luciferase Gene : Structure and Expression in Mammalian Cells. *Molecular and Cellular Biology* **7**, 725–737 (1987).
77. Branchini, B. R., Southworth, T. L., Khattak, N. F., Michelini, E. & Roda, A. Red- and green-emitting firefly luciferase mutants for bioluminescent reporter applications. *Analytical biochemistry* **345**, 140–8 (2005).
78. Wood, K. V., Lam, Y. a, McElroy, W. D. & Seliger, H. H. Bioluminescent click beetles revisited. *Journal of bioluminescence and chemiluminescence* **4**, 31–9 (1989).
79. Tannous, B. a, Kim, D.-E., Fernandez, J. L., Weissleder, R. & Breakefield, X. O. Codon-optimized Gaussia luciferase cDNA for mammalian gene expression in culture and in vivo. *Molecular therapy : the journal of the American Society of Gene Therapy* **11**, 435–43 (2005).
80. Matthews, J. C., Hori, K. & Cormier, M. J. Purification and properties of Renilla reniformis luciferase. *Biochemistry* **16**, 85–91 (1977).
81. Thompson, E. M., Nagata, S. & Tsuji, F. I. Cloning and expression of cDNA for the luciferase from the marine ostracod *Vargula hilgendorffii*. *Proceedings of the National Academy of Sciences of the United States of America* **86**, 6567–6571 (1989).
82. Tanahashi, Y. *et al.* Continuous measurement of targeted promoter activity by a secreted bioluminescence reporter, *Vargula hilgendorffii* luciferase. *Analytical Biochemistry* **289**, 260–266 (2001).
83. Nakajima, Y., Kobayashi, K., Yamagishi, K., Enomoto, T. & Ohmiya, Y. cDNA cloning and characterization of a secreted luciferase from the luminous Japanese ostracod, *Cypridina noctiluca*. *Bioscience, biotechnology, and biochemistry* **68**, 565–70 (2004).
84. Tang, Y. *et al.* In vivo tracking of neural progenitor cell migration to glioblastomas. *Human gene therapy* **14**, 1247–54 (2003).
85. Kim, D.-E., Schellingerhout, D., Ishii, K., Shah, K. & Weissleder, R. Imaging of stem cell recruitment to ischemic infarcts in a murine model. *Stroke; a journal of cerebral circulation* **35**, 952–7 (2004).
86. Costa, G. L. *et al.* Adoptive immunotherapy of experimental autoimmune encephalomyelitis via T cell delivery of the IL-12 p40 subunit. *Journal of immunology (Baltimore, Md. : 1950)* **167**, 2379–87 (2001).
87. Klohs, J. *et al.* In vivo imaging of the inflammatory receptor CD40 after cerebral ischemia using a fluorescent antibody. *Stroke; a journal of cerebral circulation* **39**, 2845–52 (2008).

88. Sugiyama, T. *et al.* Near-infrared fluorescence labeling allows noninvasive tracking of bone marrow stromal cells transplanted into rat infarct brain. *Neurosurgery* **68**, 1036–47; discussion 1047 (2011).
89. Un, P. Romeis Mikroskopische Technik. *Enzyme* **18**, 551 (2010).
90. Hong, S. *et al.* Functional analysis of various promoters in lentiviral vectors at different stages of in vitro differentiation of mouse embryonic stem cells. *Molecular therapy : the journal of the American Society of Gene Therapy* **15**, 1630–9 (2007).
91. Burns, J. C., Friedmann, T., Driever, W., Burrascano, M. & Yee, J. K. Vesicular stomatitis virus G glycoprotein pseudotyped retroviral vectors: concentration to very high titer and efficient gene transfer into mammalian and nonmammalian cells. *Proceedings of the National Academy of Sciences of the United States of America* **90**, 8033–7 (1993).
92. Morita, S., Kojima, T. & Kitamura, T. Plat-E: an efficient and stable system for transient packaging of retroviruses. *Gene therapy* **7**, 1063–6 (2000).
93. Conti, L. *et al.* Niche-independent symmetrical self-renewal of a mammalian tissue stem cell. *PLoS biology* **3**, e283 (2005).
94. Arvidsson, S., Kwasniewski, M., Riaño-Pachón, D. M. & Mueller-Roeber, B. QuantPrime--a flexible tool for reliable high-throughput primer design for quantitative PCR. *BMC bioinformatics* **9**, 465 (2008).
95. Willems, E. *et al.* Selection of reference genes in mouse embryos and in differentiating human and mouse ES cells. *The International journal of developmental biology* **50**, 627–35 (2006).
96. Pfaffl, M. W., Horgan, G. W. & Dempfle, L. Relative expression software tool (REST©) for group-wise comparison and statistical analysis of relative expression results in real-time PCR. *Nucleic Acids Research* **30**, e36 (2002).
97. Laemmli, U. K. Cleavage of structural proteins during assembly of the head of bacteriophage T4. *Nature* **227**, 680–685 (1970).
98. Graham, F. L., Smiley, J., Russell, W. C. & Nairn, R. Characteristics of a human cell line transformed by DNA from human adenovirus type 5. *The Journal of general virology* **36**, 59–74 (1977).
99. Snyder, E. Y. *et al.* Multipotent neural cell lines can engraft and participate in development of mouse cerebellum. *Cell* **68**, 33–51 (1992).
100. Nichols, J., Evans, E. P. & Smith, a G. Establishment of germ-line-competent embryonic stem (ES) cells using differentiation inhibiting activity. *Development (Cambridge, England)* **110**, 1341–8 (1990).
101. Doetschman, T. C., Eistetter, H., Katz, M., Schmidt, W. & Kemler, R. The in vitro development of blastocyst-derived embryonic stem cell lines: formation of visceral yolk sac, blood islands and myocardium. *Journal of embryology and experimental morphology* **87**, 27–45 (1985).
102. Ausman, J. I., Shapiro, W. R. & Rall, D. P. Studies on the chemotherapy of experimental brain tumors: development of an experimental model. *Cancer Research* **30**, 2394–2400 (1970).
103. Pontén, J. & Macintyre, E. H. Long term culture of normal and neoplastic human glia. *Acta pathologica et microbiologica Scandinavica* **74**, 465–86 (1968).
104. Holden, L. J. & Coleman, M. D. Assessment of the astrogliotic responses of three human astrocytoma cell lines to ethanol, trimethyltin chloride and acrylamide. *Toxicology* **241**, 75–83 (2007).
105. Das, C. M. *et al.* Valproic acid induces p21 and topoisomerase-II (alpha/beta) expression and synergistically enhances etoposide cytotoxicity in human glioblastoma cell lines. *Journal of neuro-oncology* **85**, 159–70 (2007).
106. Daldrop-Link, H. E. *et al.* Cell tracking with gadophrin-2: a bifunctional contrast agent for MR imaging, optical imaging, and fluorescence microscopy. *European journal of nuclear medicine and molecular imaging* **31**, 1312–21 (2004).
107. Neumann, E., Schaefer-Ridder, M., Wang, Y. & Hofschneider, P. H. Gene transfer into mouse lyoma cells by electroporation in high electric fields. *the The European Molecular Biology Organization Journal* **1**, 841–845 (1982).

108. Kruttwig, K. Molekulare Markierungsstrategien für die optische und magnetresonanztomographische zelluläre Visualisierung. *Naturwissenschaften* (2009).
109. Chen, C. & Okayama, H. High-efficiency transformation of mammalian cells by plasmid DNA. *Molecular and Cellular Biology* **7**, 2745–2752 (1987).
110. Kraft, K. A., Fatouros, P. P., Clarke, G. D. & Kishore, P. R. An MRI phantom material for quantitative relaxometry. *Magnetic resonance in medicine official journal of the Society of Magnetic Resonance in Medicine Society of Magnetic Resonance in Medicine* **5**, 555–562 (1987).
111. Eis, M. & Hoehn-berlage, M. A time-efficient method for combined T1 and T2 measurement in magnetic resonance imaging: Evaluation for multiparameter tissue characterization. *Magma Magnetic Resonance Materials in Physics, Biology, and Medicine* **2**, 79–89 (1994).
112. Boehm-Sturm, P., Mengler, L., Wecker, S., Hoehn, M. & Kallur, T. In vivo tracking of human neural stem cells with ¹⁹F magnetic resonance imaging. *PLoS one* **6**, e29040 (2011).
113. Arena, F., Singh, J. B., Gianolio, E., Stefania, R. & Aime, S. β -Gal gene expression MRI reporter in melanoma tumor cells. Design, synthesis, and in vitro and in vivo testing of a Gd(III) containing probe forming a high relaxivity, melanin-like structure upon β -Gal enzymatic activation. *Bioconjugate chemistry* **22**, 2625–35 (2011).
114. Aswendt, M. *et al.* In vivo imaging of inhibitory, GABAergic neurons by MRI. *NeuroImage* (2012).doi:10.1016/j.neuroimage.2012.05.029
115. Gudbjartsson, H. & Patz, S. The Rician distribution of noisy MRI data. *Magnetic resonance in medicine: official journal of the Society of Magnetic Resonance in Medicine / Society of Magnetic Resonance in Medicine* **34**, 910–4 (1995).
116. Deng, Y. P. *et al.* Differential loss of striatal projection systems in Huntington's disease: a quantitative immunohistochemical study. *Journal of chemical neuroanatomy* **27**, 143–64 (2004).
117. Reiner, A. *et al.* Differential loss of striatal projection neurons in Huntington disease. *Proceedings of the National Academy of Sciences of the United States of America* **85**, 5733–7 (1988).
118. Schwartz-Bloom, R. D. & Sah, R. gamma-Aminobutyric acid(A) neurotransmission and cerebral ischemia. *Journal of neurochemistry* **77**, 353–371 (2001).
119. Eis, M. Einflußgrößen und Fehlergrenzen bei der Messung von Relaxationszeiten und Protoendichten biologischer Gewebe an Magnetresonanztomographen. (1989).
120. Hsieh, V. & Jasanoff, A. Bioengineered Probes for Molecular Magnetic Resonance Imaging in the Nervous System. *ACS Chemical Neuroscience* **3**, 593–602 (2012).
121. Shin, E., Palmer, M. J., Li, M. & Fricker, R. a GABAergic neurons from mouse embryonic stem cells possess functional properties of striatal neurons in vitro, and develop into striatal neurons in vivo in a mouse model of Huntington's disease. *Stem cell reviews* **8**, 513–31 (2012).
122. Okabe, S., Forsberg-Nilsson, K., Spiro, C., Segal, M. & McKay, R. D. Development of neuronal precursor cells and functional postmitotic neurons from embryonic stem cells in vitro. *Mechanisms of development* **59**, 89–102 (1996).
123. Küstermann, E. *et al.* Efficient stem cell labeling for MRI studies. *Contrast media molecular imaging* **3**, 27–37 (2008).
124. Rudelius, M. *et al.* Highly efficient paramagnetic labelling of embryonic and neuronal stem cells. *European journal of nuclear medicine and molecular imaging* **30**, 1038–44 (2003).
125. Terreno, E. *et al.* Effect of the intracellular localization of a Gd-based imaging probe on the relaxation enhancement of water protons. *Magnetic resonance in medicine: official journal of the Society of Magnetic Resonance in Medicine / Society of Magnetic Resonance in Medicine* **55**, 491–7 (2006).
126. Walczak, P. *et al.* Magnetoelectroporation: improved labeling of neural stem cells and leukocytes for cellular magnetic resonance imaging using a single FDA-approved agent. *Nanomedicine nanotechnology biology and medicine* **2**, 89–94 (2006).

127. Himmelreich, U. *et al.* A responsive MRI contrast agent to monitor functional cell status. *NeuroImage* **32**, 1142–9 (2006).
128. Louie, A. Y. *et al.* In-vivo visualization of gene expression using magnetic resonance imaging. *Nature Biotechnology* **52**, 321–325 (2000).
129. Yoo, B. & Pagel, M. D. An overview of responsive MRI contrast agents for molecular imaging. *Frontiers in bioscience : a journal and virtual library* **13**, 1733–52 (2008).
130. Himmelreich, U. & Dresselaers, T. Cell labeling and tracking for experimental models using magnetic resonance imaging. *Methods (San Diego, Calif.)* **48**, 112–24 (2009).
131. Shapiro, M. G. *et al.* Directed evolution of a magnetic resonance imaging contrast agent for noninvasive imaging of dopamine. *Nature biotechnology* **28**, 264–70 (2010).
132. Mishra, A., Gottschalk, S., Engelmann, J. & Parker, D. Responsive imaging probes for metabotropic glutamate receptors. *Chemical Science* **3**, 131–135 (2012).
133. Dinca, E. B., Voicu, R. V & Ciurea, A. V Bioluminescence imaging of invasive intracranial xenografts: implications for translational research and targeted therapeutics of brain tumors. *Neurosurgical review* **33**, 385–94 (2010).
134. Yang, S.-H. *et al.* Assessment of cetuximab efficacy by bioluminescence monitoring of intracranial glioblastoma xenograft in mouse. *Journal of neuro-oncology* **95**, 23–8 (2009).
135. Liang, Y., Walczak, P. & Bulte, J. W. M. Comparison of red-shifted firefly luciferase Ppy RE9 and conventional Luc2 as bioluminescence imaging reporter genes for in vivo imaging of stem cells. *Journal of biomedical optics* **17**, 016004 (2012).
136. De Vocht, N. *et al.* Quantitative and phenotypic analysis of mesenchymal stromal cell graft survival and recognition by microglia and astrocytes in mouse brain. *Immunobiology* 1–10 (2012).doi:10.1016/j.imbio.2012.08.266
137. Deroose, C. M. *et al.* Noninvasive monitoring of long-term lentiviral vector-mediated gene expression in rodent brain with bioluminescence imaging. *Molecular therapy : the journal of the American Society of Gene Therapy* **14**, 423–31 (2006).
138. Shah, K., Tang, Y., Breakefield, X. & Weissleder, R. Real-time imaging of TRAIL-induced apoptosis of glioma tumors in vivo. *Oncogene* **22**, 6865–72 (2003).
139. Pollard, S. M., Conti, L., Sun, Y., Goffredo, D. & Smith, A. Adherent neural stem (NS) cells from fetal and adult forebrain. *Cerebral cortex (New York, N.Y. : 1991)* **16 Suppl 1**, i112–20 (2006).
140. Doetsch, F., Caillé, I., Lim, D. A., García-Verdugo, J. M. & Alvarez-Buylla, A. Subventricular zone astrocytes are neural stem cells in the adult mammalian brain. *Cell* **97**, 703–716 (1999).
141. Doetsch, F., Petreanu, L., Caille, I., Garcia-Verdugo, J. M. & Alvarez-Buylla, A. EGF converts transit-amplifying neurogenic precursors in the adult brain into multipotent stem cells. *Neuron* **36**, 1021–1034 (2002).
142. Aguirre, A. a, Chittajallu, R., Belachew, S. & Gallo, V. NG2-expressing cells in the subventricular zone are type C-like cells and contribute to interneuron generation in the postnatal hippocampus. *The Journal of cell biology* **165**, 575–89 (2004).
143. Conti, L. & Cattaneo, E. Neural stem cell systems: physiological players or in vitro entities? *Nature reviews. Neuroscience* **11**, 176–87 (2010).
144. Götz, M., Hartfuss, E. & Malatesta, P. Radial glial cells as neuronal precursors: a new perspective on the correlation of morphology and lineage restriction in the developing cerebral cortex of mice. *Brain research bulletin* **57**, 777–88 (2002).
145. Sakakibara, S. *et al.* Mouse-Musashi-1, a neural RNA-binding protein highly enriched in the mammalian CNS stem cell. *Developmental biology* **176**, 230–42 (1996).
146. Hartfuss, E., Galli, R., Heins, N. & Götz, M. Characterization of CNS precursor subtypes and radial glia. *Developmental biology* **229**, 15–30 (2001).
147. Bibel, M. *et al.* Differentiation of mouse embryonic stem cells into a defined neuronal lineage. *Nature neuroscience* **7**, 1003–9 (2004).
148. Kaneko, Y. *et al.* Musashi1: an evolutionally conserved marker for CNS progenitor cells including neural stem cells. *Developmental neuroscience* **22**, 139–53 (2000).

149. Corti, S. *et al.* Isolation and characterization of murine neural stem/progenitor cells based on Prominin-1 expression. *Experimental Neurology* **205**, 547–562 (2007).
150. Kania, G. *et al.* Somatic stem cell marker prominin-1/CD133 is expressed in embryonic stem cell-derived progenitors. *Stem cells (Dayton, Ohio)* **23**, 791–804 (2005).
151. Pfeiffer, S. E., Warrington, A. E. & Bansal, R. The oligodendrocyte and its many cellular processes. *Trends in cell biology* **3**, 191–7 (1993).
152. Mi, R. *et al.* Immortalized neural stem cells differ from nonimmortalized cortical neurospheres and cerebellar granule cell progenitors. *Experimental neurology* **194**, 301–19 (2005).
153. Zhu, L.-L., Wu, L.-Y., Yew, D. T. & Fan, M. Effects of hypoxia on the proliferation and differentiation of NSCs. *Molecular neurobiology* **31**, 231–42 (2005).
154. Knoepfler, P. S. Deconstructing stem cell tumorigenicity: a roadmap to safe regenerative medicine. *Stem cells (Dayton, Ohio)* **27**, 1050–6 (2009).
155. Erdö, F. *et al.* Host-dependent tumorigenesis of embryonic stem cell transplantation in experimental stroke. *Journal of cerebral blood flow and metabolism : official journal of the International Society of Cerebral Blood Flow and Metabolism* **23**, 780–5 (2003).
156. Pevny, L. H., Sockanathan, S., Placzek, M. & Lovell-Badge, R. A role for SOX1 in neural determination. *Development (Cambridge, England)* **125**, 1967–78 (1998).
157. Ibrahimi, A. *et al.* Highly efficient multicistronic lentiviral vectors with peptide 2A sequences. *Human gene therapy* **20**, 845–60 (2009).
158. Gassmann, M., Donoho, G. & Berg, P. Maintenance of an extrachromosomal plasmid vector in mouse embryonic stem cells. *Proceedings of the National Academy of Sciences of the United States of America* **92**, 1292–1296 (1995).
159. Camenisch, G. *et al.* A polyoma-based episomal vector efficiently expresses exogenous genes in mouse embryonic stem cells. *Nucleic Acids Research* **24**, 3707–3713 (1996).
160. Dhara, S. K. *et al.* Genetic manipulation of neural progenitors derived from human embryonic stem cells. *Tissue engineering. Part A* **15**, 3621–34 (2009).
161. Millington, M., Arndt, A., Boyd, M., Applegate, T. & Shen, S. Towards a clinically relevant lentiviral transduction protocol for primary human CD34 hematopoietic stem/progenitor cells. *PLoS one* **4**, e6461 (2009).
162. Wu, J. C. *et al.* Proteomic analysis of reporter genes for molecular imaging of transplanted embryonic stem cells. *Proteomics* **6**, 6234–49 (2006).
163. Lee, J.-P., Tsai, D. J., In Park, K., Harvey, A. R. & Snyder, E. Y. The dynamics of long-term transgene expression in engrafted neural stem cells. *The Journal of comparative neurology* **515**, 83–92 (2009).
164. Vroemen, M., Weidner, N. & Blesch, A. Loss of gene expression in lentivirus- and retrovirus-transduced neural progenitor cells is correlated to migration and differentiation in the adult spinal cord. *Experimental neurology* **195**, 127–39 (2005).
165. Zhao, H. *et al.* Emission spectra of bioluminescent reporters and interaction with mammalian tissue determine the sensitivity of detection in vivo. *Journal of biomedical optics* **10**, 41210 (2005).
166. Miloud, T., Henrich, C. & Hämmerling, G. J. Quantitative comparison of click beetle and firefly luciferases for in vivo bioluminescence imaging. *Journal of biomedical optics* **12**, 054018 (2007).
167. Gil, J. S., Machado, H. B. & Herschman, H. R. A Method to Rapidly and Accurately Compare the Relative Efficacies of Non-invasive Imaging Reporter Genes in a Mouse Model and its Application to Luciferase Reporters. *Molecular Imaging and Biology* (2011).doi:10.1007/s11307-011-0515-1
168. Sherf, B. A. & Wood, K. V. Firefly luciferase engineered for improved genetic reporting. *Promega Notes* **49** 14–21 (1994).
169. Tuchin, V. *Tissue Optics*. (SPIE: 1000 20th Street, Bellingham, WA 98227-0010 USA, 2007).doi:10.1117/3.684093

170. Warren, R. C. *Physics and the architecture of cell membranes*. (Hilger: 1987).at <<http://books.google.de/books?id=Gb4sAAAAYAAJ>>
171. Zhao, H. *et al.* Emission spectra of bioluminescent reporters and interaction with mammalian tissue determine the sensitivity of detection in vivo. *Journal of biomedical optics* **10**, 41210 (2012).
172. Conley, N. R., Dragulescu-Andrasi, A., Rao, J. & Moerner, W. E. A selenium analogue of firefly d-luciferin with red-shifted bioluminescence emission. *Angewandte Chemie (International ed. in English)* **51**, 3350–3 (2012).
173. Sher, F., van Dam, G., Boddeke, E. & Copray, S. Bioluminescence imaging of Olig2-neural stem cells reveals improved engraftment in a demyelination mouse model. *Stem cells (Dayton, Ohio)* **27**, 1582–91 (2009).
174. Chen, I. Y. *et al.* Comparison of optical bioluminescence reporter gene and superparamagnetic iron oxide MR contrast agent as cell markers for noninvasive imaging of cardiac cell transplantation. *Molecular imaging and biology : MIB : the official publication of the Academy of Molecular Imaging* **11**, 178–87 (2009).
175. Cordeau, P., Lalancette-Hébert, M., Weng, Y. C. & Kriz, J. Live imaging of neuroinflammation reveals sex and estrogen effects on astrocyte response to ischemic injury. *Stroke; a journal of cerebral circulation* **39**, 935–42 (2008).
176. Lalancette-Hébert, M., Phaneuf, D., Soucy, G., Weng, Y. C. & Kriz, J. Live imaging of Toll-like receptor 2 response in cerebral ischaemia reveals a role of olfactory bulb microglia as modulators of inflammation. *Brain : a journal of neurology* **132**, 940–54 (2009).
177. Daadi, M. M. *et al.* Molecular and magnetic resonance imaging of human embryonic stem cell-derived neural stem cell grafts in ischemic rat brain. *Molecular therapy : the journal of the American Society of Gene Therapy* **17**, 1282–91 (2009).
178. Kim, J.-B. *et al.* Non-invasive detection of a small number of bioluminescent cancer cells in vivo. *PloS one* **5**, e9364 (2010).
179. Akimoto, H. *et al.* In vivo bioluminescence imaging of bone marrow-derived cells in brain inflammation. *Biochemical and biophysical research communications* **380**, 844–9 (2009).
180. De Vocht, N. *et al.* Labeling of Luciferase/eGFP-expressing bone marrow-derived stromal cells with fluorescent micron-sized iron oxide particles improves quantitative and qualitative multimodal imaging of cellular grafts in vivo. *Molecular imaging and biology : MIB : the official publication of the Academy of Molecular Imaging* **13**, 1133–45 (2011).
181. Keyaerts, M. *et al.* Dynamic bioluminescence imaging for quantitative tumour burden assessment using IV or IP administration of D: -luciferin: effect on intensity, time kinetics and repeatability of photon emission. *European journal of nuclear medicine and molecular imaging* **35**, 999–1007 (2008).
182. Inoue, Y. *et al.* Comparison of subcutaneous and intraperitoneal injection of D-luciferin for in vivo bioluminescence imaging. *European journal of nuclear medicine and molecular imaging* **36**, 771–9 (2009).
183. Pesnel, S. *et al.* Quantitation in bioluminescence imaging by correction of tissue absorption for experimental oncology. *Molecular imaging and biology : MIB : the official publication of the Academy of Molecular Imaging* **13**, 646–52 (2011).
184. Bergwerf, I. *et al.* Reporter gene-expressing bone marrow-derived stromal cells are immune-tolerated following implantation in the central nervous system of syngeneic immunocompetent mice. *BMC Biotechnology* **9**, (2009).
185. Berman, S. C., Galpoththawela, C., Gilad, A. a, Bulte, J. W. M. & Walczak, P. Long-term MR cell tracking of neural stem cells grafted in immunocompetent versus immunodeficient mice reveals distinct differences in contrast between live and dead cells. *Magnetic resonance in medicine : official journal of the Society of Magnetic Resonance in Medicine / Society of Magnetic Resonance in Medicine* **65**, 564–74 (2011).

186. Ignowski, J. M. & Schaffer, D. V Kinetic analysis and modeling of firefly luciferase as a quantitative reporter gene in live mammalian cells. *Biotechnology and bioengineering* **86**, 827–34 (2004).
187. Paroo, Z. *et al.* Validating bioluminescence imaging as a high-throughput, quantitative modality for assessing tumor burden. *Molecular imaging* **3**, 117–24 (2004).
188. Gustafson, D. L. & Bradshaw-pierce, E. L. *Principles of Anticancer Drug Development*. (Springer New York: New York, NY, 2011).doi:10.1007/978-1-4419-7358-0
189. Sim, H., Bibee, K., Wickline, S. & Sept, D. Pharmacokinetic modeling of tumor bioluminescence implicates efflux, and not influx, as the bigger hurdle in cancer drug therapy. *Cancer research* **71**, 686–92 (2011).
190. Berger, F., Paulmurugan, R., Bhaumik, S. & Gambhir, S. S. Uptake kinetics and biodistribution of ¹⁴C-D-luciferin—a radiolabeled substrate for the firefly luciferase catalyzed bioluminescence reaction: impact on bioluminescence based reporter gene imaging. *European journal of nuclear medicine and molecular imaging* **35**, 2275–85 (2008).
191. Lembert, N. & Idahl, L. a Regulatory effects of ATP and luciferin on firefly luciferase activity. *The Biochemical journal* **305 (Pt 3)**, 929–33 (1995).
192. Hasan, M. T., Schönig, K., Berger, S., Graewe, W. & Bujard, H. Long-term, noninvasive imaging of regulated gene expression in living mice. *Genesis New York NY* **29**, 116–122 (2001).
193. Luker, G. D. *et al.* Noninvasive Bioluminescence Imaging of Herpes Simplex Virus Type 1 Infection and Therapy in Living Mice. *Journal of Virology* **76**, 12149–12161 (2002).
194. Choy, G. *et al.* Comparison of noninvasive fluorescent and bioluminescent small animal optical imaging. *BioTechniques* **35**, 1022–6, 1028–30 (2003).
195. Edinger, M. *et al.* Advancing animal models of neoplasia through in vivo bioluminescence imaging. *European Journal of Cancer* **38**, 2128–2136 (2002).
196. Lipshutz, G. S. *et al.* In utero delivery of adeno-associated viral vectors: intraperitoneal gene transfer produces long-term expression. *Molecular therapy the journal of the American Society of Gene Therapy* **3**, 284–292 (2001).
197. Pawson, P. & Forsyth, S. Chapter 5 - Anesthetic agents. *Small Animal Clinical Pharmacology* 83–112 (2008).doi:10.1016/B978-070202858-8.50007-5
198. Zuurbier, C. J., Emons, V. M. & Ince, C. Hemodynamics of anesthetized ventilated mouse models: aspects of anesthetics, fluid support, and strain. *American journal of physiology. Heart and circulatory physiology* **282**, H2099–105 (2002).
199. Janssen, B. J. a *et al.* Effects of anesthetics on systemic hemodynamics in mice. *American journal of physiology. Heart and circulatory physiology* **287**, H1618–24 (2004).
200. Hildebrandt, I. J., Su, H. & Weber, W. a Anesthesia and other considerations for in vivo imaging of small animals. *ILAR journal / National Research Council, Institute of Laboratory Animal Resources* **49**, 17–26 (2008).
201. Nguyen, V. T., Morgange, M. & Bensaude, O. Firefly Luciferase Luminescence Assays Using Scintillation Counters Quantitation in Transfected Mammalian Cells. *Analytical biochemistry* **171**, 404–408 (1988).
202. Blø, M., Micklem, D. R. & Lorens, J. B. Enhanced gene expression from retroviral vectors. *BMC biotechnology* **8**, 19 (2008).
203. Eng, L. F., Vanderhaeghen, J. J., Bignami, A. & Gerstl, B. An acidic protein isolated from fibrous astrocytes. *Brain research* **28**, 351–4 (1971).
204. Brenner, M., Kisseberth, W. C., Su, Y., Besnard, F. & Messing, A. GFAP Promoter Mice Directs Astrocyte-specific in Transgenic Mice. *The Journal of Neuroscience* **74**, 1030–1037 (1994).
205. Mucke, L., Oldstone, M. B., Morris, J. C. & Nerenberg, M. I. Rapid activation of astrocyte-specific expression of GFAP-lacZ transgene by focal injury. *The New biologist* **3**, 465–474 (1991).
206. Su, M. *et al.* Expression specificity of GFAP transgenes. *Neurochemical research* **29**, 2075–93 (2004).

207. Wu, C. *et al.* Combinatorial control of suicide gene expression by tissue-specific promoter and microRNA regulation for cancer therapy. *Molecular Therapy* **17**, 2058–2066 (2009).
208. McKie, E. A., Graham, D. I. & Brown, S. M. Selective astrocytic transgene expression in vitro and in vivo from the GFAP promoter in a HSV RL1 null mutant vector--potential glioblastoma targeting. *Gene Therapy* **5**, 440–450 (1998).
209. Shi, N., Zhang, Y., Zhu, C., Boado, R. J. & Pardridge, W. M. Brain-specific expression of an exogenous gene after i.v. administration. *Proceedings of the National Academy of Sciences of the United States of America* **98**, 12754–9 (2001).
210. Holland, E. C. & Varmus, H. E. Basic fibroblast growth factor induces cell migration and proliferation after glia-specific gene transfer in mice. *Proceedings of the National Academy of Sciences of the United States of America* **95**, 1218–1223 (1998).
211. Carpenter, M. K. *et al.* Generation and transplantation of EGF-responsive neural stem cells derived from GFAP-hNGF transgenic mice. *Experimental Neurology* **148**, 187–204 (1997).
212. Kordower, J. H. *et al.* Grafts of EGF-responsive neural stem cells derived from GFAP-hNGF transgenic mice: trophic and tropic effects in a rodent model of Huntington's disease. *Journal of Comparative Neurology* **387**, 96–113 (1997).
213. Smith, J. D., Sikes, J. & Levin, J. A. Human apolipoprotein E allele-specific brain expressing transgenic mice. *Neurobiology of Aging* **19**, 407–413 (1998).
214. Cho, W., Hagemann, T. L., Johnson, D. a, Johnson, J. a & Messing, A. Dual transgenic reporter mice as a tool for monitoring expression of glial fibrillary acidic protein. *Journal of neurochemistry* **110**, 343–51 (2009).
215. Wet, J. R. D. Cloning of Firefly Luciferase cDNA and the Expression of Active Luciferase in Escherichia coli. *Proceedings of the National Academy of Sciences* **82**, 7870–7873 (1985).
216. Wood, K. V, De Wet, J. R., Dewji, N. & DeLuca, M. Synthesis of active firefly luciferase by in vitro translation of RNA obtained from adult lanterns. *Biochemical and Biophysical Research Communications* **124**, 1154–1160 (1984).
217. Leeuw, B. De *et al.* Increased Glia-Specific Transgene Expression With Glial Fibrillary Acidic Protein Promoters Containing Multiple Enhancer Elements. *Journal of Neuroscience Research* **83**, 744–753 (2006).
218. Nguyen, P. K., Nag, D. & Wu, J. C. Methods to assess stem cell lineage, fate and function. *Advanced drug delivery reviews* **62**, 1175–86 (2010).
219. Besnard, F. *et al.* Multiple interacting sites regulate astrocyte-specific transcription of the human gene for glial fibrillary acidic protein. *The Journal of biological chemistry* **266**, 18877–83 (1991).
220. Hioki, H. *et al.* Efficient gene transduction of neurons by lentivirus with enhanced neuron-specific promoters. *Gene Therapy* **14**, 872–882 (2007).
221. Madisen, L. *et al.* A robust and high-throughput Cre reporting and characterization system for the whole mouse brain. *Nature neuroscience* **13**, 133–40 (2010).
222. Weissleder, R., Ross, B. D., Rehemtulla, A. & Gambhir, S. S. *Molecular Imaging: Principles and Practice.* (Peoples Medical Publishing House: 2010).

9. PUBLICATIONS

- 1) **Aswendt M**, Gianolio E, Pariani G, Napolitano R, Fedeli F, Himmelreich U, Aime S, Hoehn M (2012) In vivo imaging of inhibitory, GABAergic neurons by MRI. *NeuroImage* 62(3):1685-93.
- 2) Hoehn M, **Aswendt M** (2012) Structure-function relationship of cerebral networks in experimental neuroscience: Contribution of magnetic resonance imaging. *Experimental Neurology* 242: 65-73.
- 3) **Aswendt M***, Adamczak J*, Couillard-Després S, Hoehn M (2013) Boosting Bioluminescence Neuroimaging: An Optimized Protocol for Brain Studies. *PLoS ONE* 8(2):e55662.
- 4) Napolitano R, Pariani G, Fedeli F, **Aswendt M**, Aime S, Gianolio E (2013) Synthesis and Relaxometric Characterization of a MRI Gd-based probe responsive to GAD enzymatic activity. *Journal of Medicinal Chemistry* (Epub ahead of press).
- 5) Tennstaedt A, **Aswendt M**, Adamczak J, Hoehn M. (2013) Non-invasive multimodal imaging of stem cell transplants in the brain using BLI and MRI. Book chapter for Springer Protocols: *Imaging and Tracking Stem Cells: Methods*. Editor Kursad Turksen (in press).
- 6) Mezzanotte L*, **Aswendt M***, Tennstaedt A, Hoeben R, Hoehn M, Löwik C (2013) Quantitative evaluation of luciferases for in vivo bioluminescence imaging of neural stem cells. *CMMI* (in revision).

Acknowledgements

First of all, I would like to thank Prof. Klaus Reymann for supervising this work as an external reviewer. The stem cell work I started in his lab during the Diploma thesis laid the foundation of my interest in visualizing the stem cell therapy of stroke.

My thanks goes to my local supervisor at the Max Planck Institute in Cologne, Mathias Hoehn. From the first day on, he put me in charge of a challenging project and got me involved in workshops and international meetings. This was the best motivation for me, as it stimulated my own scientific ideas and I started to learn everything about molecular imaging.

I spent approximately 80% of my PhD time in the lab. Therefore, my thanks go to all members of the In-vivo-NMR group for the good working atmosphere. I have been fortunate to have had outstanding support by the laboratory staff Nadine, Gaby and Cordula. Our teamwork essentially contributed to the completion of my work. Michael helped me a lot with software for fitting relaxation times. Philipp, Joanna, Luam and Daniel – my PhD colleagues in the lab - thank you for sharing ideas, experiences and (sometimes) leisure time.

I really appreciated the help from the “senior” scientists in the lab, who made important experiments possible. Annette, who shared her knowledge in molecular biology and gave input for writing. I also learned a lot from Thérèse and Tracy. I appreciated help from Dirk, who explained more than once the essential parts of the MRI system (which culminated in the quenching of the 4.7 T, which I had used nearly exclusively at this time). I also thank Klaus and Chantal, for the help at the beginning of my PhD thesis.

I would like to thank the external cooperation partners: Eliana Gianolio, Silvio Aime, Laura Mezzanotte, Clemens Löwik, Uwe Himmelreich, Aneta Keliris, Sébastien Couillard-Després, Vera Lepperhof and Tomo Saric.

I dedicate this dissertation to my parents, in return of their continuous support and motivation throughout the years of study. The belief of my family in my capabilities made it often easier to go on. My thanks to Michèle for keeping me grounded during all the time.

Curriculum Vitae

Name	Markus Aswendt
Geburtsdatum	20.05.1984
Geburtsort	Karl-Marx-Stadt, heute Chemnitz
Familienstand	ledig
Staatsangehörigkeit	deutsch
Adresse	Helmholtzstr. 13, 50825 Köln

Ausbildung

seit 05/2009	Max-Planck-Institut für neurologische Forschung, Köln In-vivo-NMR, Prof. Mathias Hoehn, Promotion
02/2008-02/2009	Leibniz Institute für Neurobiologie, Magdeburg PG Neuropharmakologie, Prof. Klaus Reymann Diplomarbeit (Abschluss: Diplom Neurowissenschaftler)
10/2005-02/2009	Otto-von-Guericke Universität, Magdeburg Hauptstudium der Neurobiologie
10/2003-09/2005	Martin-Luther-University, Halle-Wittenberg Grundstudium der Biochemie (Abschluss: Vordiplom)
1994-2002	Carl-Friedrich-Gauß and Johannes-Kepler Gymnasiun, Chemnitz Abitur

Köln, 26.11.2012

Erklärung

Hiermit erkläre ich, dass ich die von mir eingereichte Dissertation zu dem Thema „Imaging beyond structure - novel noninvasive tools for neuroimaging of stem cell function and differentiation -“ selbstständig verfasst, nicht schon als Dissertation verwendet habe und die benutzten Hilfsmittel und Quellen vollständig angegeben wurden.

Weiterhin erkläre ich, dass ich weder diese noch eine andere Arbeit zur Erlangung des akademischen Grades doctor rerum naturalium (Dr. rer. nat.) an anderen Einrichtungen eingereicht habe.

Köln, 26.11.2012
